

April 2018

# Integration and Cross-Coupling of a Notched-Turbine Symbiotic Power Source for Implantable Medical Devices

Samuel Perez

University of South Florida, [sperez2@mail.usf.edu](mailto:sperez2@mail.usf.edu)

Follow this and additional works at: <http://scholarcommons.usf.edu/etd>

 Part of the [Biomedical Engineering and Bioengineering Commons](#), [Electrical and Computer Engineering Commons](#), and the [Other Education Commons](#)

## Scholar Commons Citation

Perez, Samuel, "Integration and Cross-Coupling of a Notched-Turbine Symbiotic Power Source for Implantable Medical Devices" (2018). *Graduate Theses and Dissertations*.  
<http://scholarcommons.usf.edu/etd/7215>

This Dissertation is brought to you for free and open access by the Graduate School at Scholar Commons. It has been accepted for inclusion in Graduate Theses and Dissertations by an authorized administrator of Scholar Commons. For more information, please contact [scholarcommons@usf.edu](mailto:scholarcommons@usf.edu).

Integration and Cross-Coupling of a Notched-Turbine Symbiotic  
Power Source for Implantable Medical Devices

by

Samuel Pérez Minaya

A dissertation submitted in partial fulfillment  
of the requirements for the degree of  
Doctor of Philosophy  
Department of Electrical Engineering  
College of Engineering  
University of South Florida

Major Professor: Sylvia Thomas, Ph.D.  
Arash Takshi, Ph.D.  
Jing Wang, Ph.D.  
Delcie Durham, Ph.D.  
Lennox Hoyte, M.D.

Date of Approval:  
March 19, 2018

Keywords: energy harvesting, implantation, power efficiency, notched turbine, MPPT,  
DC-DC converter

Copyright © 2018, Samuel Pérez Minaya

## DEDICATION

This dissertation is dedicated to my beautiful wife Dorka Pérez (Kyla) for always believing in me and giving me such unwavering support and to my lovely daughters Shania and Chenella for helping me realize and understand the meaning and purpose of my life. My goal is to show how much I love you because my words cannot describe it well enough.

## ACKNOWLEDGMENTS

I want to thank God, The Holy Spirit and my Lord and Savior Jesus Christ for saving me and for blessing me with a wonderful life in a family that has always given me more than I could ever ask for. Kyla, Shania and Chenella I love more than words can express. I am thankful to my extended family, my mother Noemi and my father Manuelico who gave me the best example of hard work and dedication and taught me to persevere no matter what obstacles may stand in my way. I am thankful to all my brothers and sisters: Angel, Iran, Rebeca, Natanael, David, Ruth, Debora, Omni and Bethania for their unfailing love and support throughout the years. I love you all dearly.

This dissertation was possible by the collaborative effort of my major professor Dr. Sylvia Thomas and the wonderful team she leads: The AMBIR research group whose members were a wonderful asset in the completion of this work, not only technically but also morally and spiritually. Thank you William Serrano, Manopriya Devisetty, Majdi Ababneh, Kavyashree Puttananjegowda, Ridita Khan, Nirmita Roy, Katty Pierre-Charles and Idi Tulloch for his support in the calculations of efficiency.

I want to give a special thanks to my friend and collaborator Dr. Henry Cabra for his wonderful support, enthusiasm and counseling during the last few years.

I also extend my gratitude to the entire staff of the Nanotechnology Research and Education Center (NREC) especially Mr. Richard Everly for sharing his instrumentation methods and ideas and to the X-labs director Dr. Michael Celestine for providing the high

accuracy measurement equipment needed in the characterization of the turbine models used in this work.

I am indebted to Dr. Sylvia Thomas for her understanding, support, trust in me, and invaluable guidance during the course of this work. To Mr. Bernard Batson, thanks for your friendship, encouragement and support in the Sloan Program, which helped extend the life of my research in so many ways.

Finally, I would like to extend my gratitude to my home church Templo La Hermosa of Valrico, my pastors, Luis and Julia Toro and the entire congregation for keeping me constantly in their prayers and encouraging me to reach higher for God's glory.

## TABLE OF CONTENTS

LIST OF TABLES	iv
LIST OF FIGURES	v
ABSTRACT	xi
CHAPTER 1: INTRODUCTION	1
1.1 Overview	1
1.2 Research Objectives	5
1.3 Contributions and Relevance of Research	7
1.4 Organization	7
CHAPTER 2: BACKGROUND	9
2.1 Implantable Power Sources and Generators	9
2.1.1 Implantable Power Generators	11
2.1.2 Chemical Implantable Power Generators	11
2.1.3 Thermoelectric Implantable Power Generators	12
2.1.4 Piezoelectric Implantable Power Generators	13
2.1.5 Electromagnetic Implantable Power Generators	13
2.1.6 Radioisotope Implantable Power Generators	16
2.1.7 RF Transcutaneous Induction Power Generators	16
2.2 Fabrication Methods	17
2.2.1 Computer Numeric Control (CNC) Machining	18
2.2.2 3D Printing	18
2.2.3 Selective Laser Sintering (SLS)	19
2.2.4 Stereo Lithography Apparatus (SLA)	20
2.2.5 Vacuum Casting	20
2.2.6 Injection Molding	20
2.3 Justification of Research	21
CHAPTER 3: PRELIMINARY STUDIES AND RESULTS	27
3.1 The Power Generator	27
3.1.1 Bench-Top Characterization	29
3.1.2 Linearity	32
3.2 Frequency Response Analysis	32
3.3 Slip Analysis and Characterization	34

CHAPTER 4: SYMBIOTIC INTRACORPORAL POWER SOURCE (SIPS) DESIGN AND SIMULATIONS	39
4.1 Overview	39
4.2 Voltage Rectification	41
4.2.1 Full Rectification	41
4.2.2 Partial Rectification	43
4.3 DC to DC Conversion	44
CHAPTER 5: HEMODYNAMIC ANALYSIS OF THE CIRCULATORY SYSTEM	48
5.1 Principles of Blood Flow	48
5.2 Anastomoses and Cross-Coupling of SIPS	52
5.3 Artery-to-Artery Anastomosis	52
5.4 Arteriovenous Anastomosis	54
5.5 Blood Components	55
5.5.1 Plasma	56
5.5.2 Blood Cells	56
5.6 Density, Viscosity and Hematocrit	57
5.7 Platelet Activation	58
5.8 Biomaterials and Hemocompatibility	59
CHAPTER 6: TESTING METHODS	61
6.1 Structural Integrity	61
6.2 Testing Methodology	61
6.3 Data Collection Approach	62
CHAPTER 7: DESIGN, FABRICATION AND ASSEMBLY	64
7.1 Introduction	64
7.2 Model Design	64
7.2.1 MST Model Design	65
7.2.2 LST Model Design	68
7.2.3 OTI-1 Model Design	69
7.2.4 OTI-2 Model Design	71
7.3 Model Fabrication	72
7.3.1 Zortrax M200 3D Printer	73
7.3.2 MST Model Fabrication	76
7.3.3 LST Model Fabrication	77
7.3.4 OTI-1 Model Fabrication	78
7.3.5 OTI-2 Model Fabrication	79
CHAPTER 8: SYSTEM TESTING	81
8.1 Testing Circuits	81
8.1.1 Rectifier	82
8.1.2 Variable Load	83
8.2 Nitrogen Gas Flow Energy Harvesting	86
8.2.1 Equipment	87
8.2.2 Setup	87

8.3 Water Flow Energy Harvesting	91
8.3.1 Equipment	91
8.3.2 Setup	92
8.4 Simulated Blood Flow Energy Harvesting	94
8.4.1 Equipment	94
8.4.2 Setup	95
CHAPTER 9: TESTING RESULTS AND DISCUSSION	97
9.1 Nitrogen Flow Harvesting Results	97
9.1.1 AC Power and Efficiency	97
9.1.2 DC Power	105
9.1.2.1 MST DC Power	105
9.1.2.2 OTI-1 DC Power	108
9.1.2.3 OTI-2 DC Power	108
9.2 Water Flow Harvesting Results	114
9.2.1 AC Power and Efficiency	114
9.2.2 Water Flow Harvesting DC Power	116
9.2.2.1 MST DC Power	119
9.2.2.2 OTI-1 DC Power	121
9.2.2.3 OTI-2 DC Power	122
9.3 Simulated Blood Flow Harvesting Results	122
9.3.1 AC Power and Efficiency	122
9.3.2 DC Power	127
9.3.2.1 OTI-1 DC Power	128
9.3.2.2 OTI-2 DC Power	128
CHAPTER 10: CONCLUSIONS AND FUTURE WORKS	132
10.1 Introduction	132
10.2 LST Conclusions	133
10.3 MST Conclusions	134
10.4 OTI-1 Conclusions	134
10.5 OTI-2 Conclusions	135
10.6 Materials Conclusions	136
10.7 Research Objectives Conclusions	138
10.8 Future Works	140
10.8.1 Emergency Notification System	141
10.8.2 Thrombus Detection System	141
REFERENCES	143
APPENDICES	152
Appendix A: Copyright Notices	153
Appendix B: Glossary of Terms	154
ABOUT THE AUTHOR	End Page



## LIST OF TABLES

Table 2.1	State of the art generator types and comparison with proposed system.	22
Table 2.2	Power requirements of most commonly used IMDs[39].	26
Table 3.1	Induced voltage and current[65].	31
Table 3.2	Calculated RPM from generator's frequency response and percent difference between $ Z $ and Z-real.	35
Table 7.1	Size comparison between original 3.175X turbine model with generator from [28] and the new miniaturized turbine (MST) with generator proposed in this work.	66
Table 7.2	Size comparison between the large scale turbine (LST) with generator and the optimized turbine for implantation 1 (OTI-1) with generator.	70
Table 7.3	Improved aspect ratio (length: height) with optimization and miniaturization	71
Table 7.4	Size comparison between the OTI-1 turbine with generator and the OTI-2 turbine with generator.	72
Table 8.1	Measured values of shear rate, shear stress and viscosity for varying RPM	96
Table 10.1	Characterization data of the OTI-1 SIPS using simulated blood flow as a harvesting source	135
Table 10.2	Characterization data of the OTI-2 SIPS using simulated blood flow as a harvesting source	136
Table 10.3	Peak power density for LTS, MST, OTI-1 and OTI-2 turbines in mW/cc	140

## LIST OF FIGURES

Figure 1.1	Common implantable medical devices.	2
Figure 1.2	Multi-sensor network for early detection of diseases and continuous monitoring of known conditions[19].	4
Figure 2.1	Symbiosis of the SIPS	10
Figure 2.2	Typical energy harvesting systems[19].	15
Figure 2.3	Computer controlled machining (top-down process) [69]	18
Figure 2.4	Trends in 3D printer sales from 2007 to 2015 [70]	19
Figure 2.5	State of the art generator types and power comparison with proposed system.	25
Figure 3.1	Armature and magnetic-ring configuration.	27
Figure 3.2	Permanent magnet orientation.	29
Figure 3.3	Actual generator armature and rotor next to a dime for size comparison.	29
Figure 3.4	Three-phase generator coil set up.	30
Figure 3.5	Test circuit used for generator characterization.	30
Figure 3.6	Voltage (top) and current (bottom) linear response w.r.t. kRPM.	33
Figure 3.7	Generator's phase and impedance measured with respect to frequency in Hz.	34
Figure 3.8	Motor & generator modes of an electric machine.	36
Figure 3.9	Micro-generator single coil characterization shows negative slip with increasing rotational speed using a 10 $\Omega$ load.	38
Figure 4.1	Symbiosis of SIPS revisited.	39
Figure 4.2	SIPS block diagram illustrating integration of its salient features.	40

Figure 4.3	One full-wave rectifier per phase.	42
Figure 4.4	Full wave, three-phase rectifier circuit.	43
Figure 4.5	P-SAC TINA simulation results with a transformer and single rectifier diode.	44
Figure 4.6	SIPS circuit comprising minimized P-SAC and DC-DC converter.	45
Figure 4.7	Simulation results of SIPS circuit of Figure 4.6.	46
Figure 5.1	Bernoulli's principle of blood flow[76].	49
Figure 5.2	Blood pressure levels in the circulatory system [77].	50
Figure 5.3	Inlet pressure vs. volume flow rate of a notched-blade turbine [28].	51
Figure 5.4	Dual stator turbine connection between a high pressure artery (input) and a lower pressure artery (output) with flow direction.	53
Figure 5.5	Vascular tree of the human body[55].	53
Figure 5.6	Dual stator turbine connection between an artery (input) and a vein (output) with flow direction.	54
Figure 5.7	Arteriovenous anastomosis (right), and arteriovenous graft (left) [78].	55
Figure 7.1	Notched-Turbine model, scale 3.175X, 2.5 inch HDD motor [28].	65
Figure 7.2	Flow velocity profile of MST fluid in a rotating mesh.	67
Figure 7.3	Top view of flowlines with arrow heads representing the direction of flow and background contour colors representing the presence or absence of turbulent behavior.	67
Figure 7.4	LST design implementing changes stemming from first miniaturization effort findings.	69
Figure 7.5	Artificial heart on the left and the Zortrax M200 3-D printer used to create it [87]	73
Figure 7.6	Zortrax printer in action printing the LST blade assembly (top), lid (lower left) and casing (lower right)	75
Figure 7.7	Miniaturized-scale turbine (MST) 3D printed in ABS and assembled for testing in a transparent holder.	76

Figure 7.8	LST casing rotor and lid 3D printed in ABS on the left and CNC-machined LST assembled for testing on the right.	77
Figure 7.9	Optimized turbine for implantation (OTI-1) 3D-printed in ABS and machined in PMMA with different barbed connectors and blade-assembly-loaded generator.	78
Figure 7.10	OTI-2 parts: Blade assembly (bottom left), generator (bottom right) and PMMA casing with barbed connectors, along with LTC 3108 femto (top right)	79
Figure 8.1	Voltage source representing the sinusoidal output from the turbine system's generator, connected to a variable load L1, used for AC testing.	82
Figure 8.2	Turbine system generator (V1ac) connected to rectifying circuit (D1, C1) and to variable load L1 for DC testing.	82
Figure 8.3	Schottky rectifier, CW from top left: Typical forward current, typical reverse current, total capacitance and forward current derating current characteristic curves[104].	83
Figure 8.4	Variable load configuration for testing AC and DC output with and without rectifier (bottom left) and high impedance measurement load on the right.	84
Figure 8.5	Rectifiers and DC to DC converters used to convert harvested energy to DC and boost it to an appropriate level for IMD's.	85
Figure 8.6	Setup of nitrogen flow through the turbine system for energy harvesting	87
Figure 8.7	Circuit diagram for measuring AC voltage and current at the load.	88
Figure 8.8	Circuit used for DC voltage and current measurements.	89
Figure 8.9	Actual lab setup described by the circuits of Figures 8.5 and 8.6	90
Figure 8.10	Principle of operation of ultrasonic flowmeter used in this work[89].	92
Figure 8.11	Closed-loop circuit setup used to evaluate the MST, OTI-1 and OTI-2 turbines' ability to harvest energy from water flow.	92
Figure 8.12	Water pump, tubing, push –fit connectors and valves used on closed-loop circuit.	92
Figure 8.13	Left to right: Microscale, vortex mixer and viscometer with attachments.	95

Figure 8.14	Shear of fluid between a moving and stationary plate under laminar flow conditions.	96
Figure 9.1	Assembled MST on the left and its components on the right.	98
Figure 9.2	MST (N) AC power in mW vs load resistance in $K\Omega$ at increasing RPM.	99
Figure 9.3	MST(N) AC power in mW vs generated voltage in volts at increasing RPM (left) and efficiency curves vs load current in mA (right)	100
Figure 9.4	LST (N) AC power in mW vs load resistance in $K\Omega$ at increasing RPM.	101
Figure 9.5	LST (N) AC power in mW vs voltage generated at increasing RPM (left) and efficiency vs AC load current in mA (right)	102
Figure 9.6	OTI-1 (N) AC power vs load resistance (left), power vs voltage (right) and efficiency vs load current in mA (bottom)	103
Figure 9.7	(N) AC OTI-2 power vs load resistance (left), power vs voltage (right) and efficiency vs load current in mA (bottom)	104
Figure 9.8	MST (N) DC power, DC load voltage/current, RPM and generator voltage against load resistance, using TI BQ 25504 to boost the voltage sent to the load.	106
Figure 9.9	MST (N) DC power, DC load voltage/current, RPM and generator voltage against load resistance, using LTC 3105 to boost the voltage sent to the load.	107
Figure 9.10	OTI-1 (N) DC power, DC load voltage/current, RPM and generator voltage against load resistance, using BQ25504 to boost the voltage sent to the load.	109
Figure 9.11	OTI-1 (N) DC power, DC load voltage/current, RPM and generator voltage against load resistance, using LTC 3105 to boost the voltage sent to the load.	110
Figure 9.12	OTI-2 (N) DC power, DC load voltage/current, RPM and generator voltage against load resistance, using BQ25504 to boost the voltage sent to the load.	111
Figure 9.13	OTI-2 (N) DC power, DC load voltage/current, RPM and generator voltage against load resistance, using LTC3105 to boost the voltage sent to the load to 5 volts.	112
Figure 9.14	OTI-2 (N) DC power, DC load voltage/current, RPM and generator voltage against load resistance, using LTC3105 to boost the voltage sent to the load to 3.5 volts.	113

Figure 9.15	MST (W) AC power in mW vs load resistance in $K\Omega$ for changing RPM, pressure difference in PSI and flow Q in liters/min	115
Figure 9.16	MST (W) AC power in mW vs generated rms voltage in volts for different RPM, pressure difference in PSI and flow Q in mL/m (left) and efficiency vs load current in mA (right)	116
Figure 9.17	OTI-1 (W) AC power in mW vs load resistance in $K\Omega$ for changing RPM, pressure difference in PSI and flow Q in liters/min	117
Figure 9.18	OTI-1 (W) AC power in mW vs generated rms voltage in volts for different RPM, pressure difference in PSI and flow Q in mL/m (left) and efficiency vs load current (right)	117
Figure 9.19	OTI-2 (W) AC power in mW vs load resistance in $K\Omega$ for changing RPM, pressure difference in PSI and flow Q in liters/min	118
Figure 9.20	OTI-2 (W) AC power in mW vs generated rms voltage in volts for different RPM, pressure difference in PSI and flow Q in mL/m (left) and efficiency vs load current in mA (right)	118
Figure 9.21	MST (W) DC power, DC load voltage/current, RPM and generator voltage against load resistance, using TI BQ 25504 to boost the voltage sent to the load at 2600 RPM (left) and at 2100 RPM (right).	119
Figure 9.22	MST (W) DC power, DC load voltage/current, RPM and generator voltage against load resistance, using LTC 3105 to boost the voltage sent to the load.	120
Figure 9.23	OTI-1 (W) DC power, DC load voltage, DC load current, RPM and RMS generator voltage against load resistance, using TI BQ 25504 (left) and LTC 3105 (right)	121
Figure 9.24	OTI-2 (W) DC power, DC load voltage, DC load current, RPM and RMS generator voltage against load resistance, using TI BQ 25504 (left) and LTC 3105 (right)	123
Figure 9.25	OTI-1 (SB) AC power in mW vs load resistance in $K\Omega$ for changing RPM, pressure difference in mmHg and flow Q in mL/min.	124
Figure 9.26	OTI-1 (SB) AC power in mW vs generated rms voltage in volts for different RPM, pressure difference in mmHg and flow Q in mL/m (top) and efficiency vs load current (bottom)	125
Figure 9.27	OTI-2 (SB) AC power in mW vs load resistance in $K\Omega$ for changing RPM, pressure difference in PSI and flow Q in mL/min.	126

Figure 9.28	OTI-2 (SB) AC power in mW vs generated rms voltage in volts for different RPM, pressure difference in mmHg and flow Q in mL/m and efficiency vs load current in mA (right)	126
Figure 9.29	OTI-1 (SB) DC power, DC load voltage, DC load current, RPM and rms generator voltage against load resistance, using LTC 3108 supercap (left) and LTC 3108 femto (right)	129
Figure 9.30	OTI-2 (SB) DC power, DC load voltage, DC load current, RPM and rms generator voltage vs load resistance, using BQ 25504 above 1000 RPM (left) and below 1000 RPM (right)	130
Figure 9.31	OTI-2 (SB) DC power, DC load voltage, DC load current, RPM and rms generator voltage against load resistance, using LTC 3108 supercap (left) and LTC 3108 femto (right)	131

## ABSTRACT

The purpose of this research is to design and integrate a symbiotic notched-turbine energy generator for implantation as a cross-coupled system capable of continuously and perpetually powering an electronic implantable medical device (IMD), which is a device designed to operate inside the body of a higher mammal to enhance, correct or provide the body with a function that has deviated from the norm or has stopped altogether. The list of IMDs available for implantation keeps growing every year, one of the newest being the VBLOC, produced by EnteroMedics®, and approved by the Food and Drug Administration (FDA) on January 15<sup>th</sup>, 2015[1], [2] to treat obesity in the United States, in lieu of the more dangerous and costly bariatric surgery widely used to treat the same condition. Some of the more traditional IMDs, such as cardiac defibrillator, pacemaker and insulin pumps require the use of a battery system for their operation.

The powering of IMDs is a topic of growing importance and as such, the energy released by the hydrodynamic action of the cardiovascular system of a higher mammal is presented in this work as a source of energy that can be converted into electricity by use of a micro turbine, loaded with magnetic rings that induce a time-varying magnetic field onto a set of insulated coils through the process of electromagnetic induction (EMI) in accordance with Faraday's Law.

This work goes beyond mere power production, and focuses on the process required to integrate this power source with an IMD, when it is coupled to the cardiovascular system for drawing hydro-mechanical power for conversion to electricity and to the IMD of choice to



deliver the conditioned power, thus replicating a symbiotic process. The harvested energy in the form of a time-varying tri-phase sine wave is therefore rectified, conditioned and made available for use to the IMD.

The proposed 3-phase generator has a volume of  $1.02 \text{ cm}^3$  and has the potential to be implemented as a dual or quad system that doubles or quadruples the single generator power capabilities accordingly. The rectifying and conditioning circuits may be housed in a hermetically sealed container, covered with a bio-compatible material such as, ultra-high molecular weight polyethylene (UHMWPE), polymethylmethacrylate (PMMA) or titanium, which can afford the best implantation properties such as non-absorbability, durability, hardness and biocompatibility [4]. Additionally, the prevention of blood clotting is of paramount importance in any IMD, which can be helped, for example by treating its surface with Tethered-Liquid Perfluorocarbons (TLP) to prevent bio-film formation of the blood that typically leads to infections and clotting[5].

## CHAPTER 1: INTRODUCTION

### 1.1 Overview

The great innovations of the last century have ushered continuous progress in many areas of technology, especially in the form of miniaturization of electronic circuits. This progress shows a trend towards consistent increases in memory density, processing speed and power density; and towards a decrease in power requirements due to miniaturization. It is worth noting that of all these, power density has seen the least improvement [11].

It is not surprising that many efforts are being made to rectify such disparity, since lower cost has given rise to the proliferation of portable electronic devices that need some form of power to operate. Usually, the supply of this power is in the form of rechargeable batteries and power conditioning circuits that work very well together to supply the demands for power. Although this is a good solution for extracorporeal (outside the body) devices, it is not the optimal solution for a group of portable devices called intra-corporeal devices found implanted inside the body of many medical patients around the world. These devices can be divided into low power and high power devices, where the former require between 30  $\mu$ W and 10 mW, and the latter require between 1.4 W to 4 W (pediatric VADs and partial support VADs ) and 4- 15 W (adult VADs) to operate [12]–[14].

It is the hypothesis of the author that a single or potentially multiple IMDs can be permanently powered from a single notched-turbine micro-generator when a symbiotic intra-corporeal power source (SIPS) is used to integrate it with the IMD(s) of choice.

This implies the elimination of the ubiquitous battery that accompanies every powered IMD currently in the market, and subsequently, the elimination of harmful material such as lithium, silver and vanadium oxide (just to name a few) that are part of primary batteries in such systems.

## ACTIVE IMPLANTABLE MEDICAL DEVICES

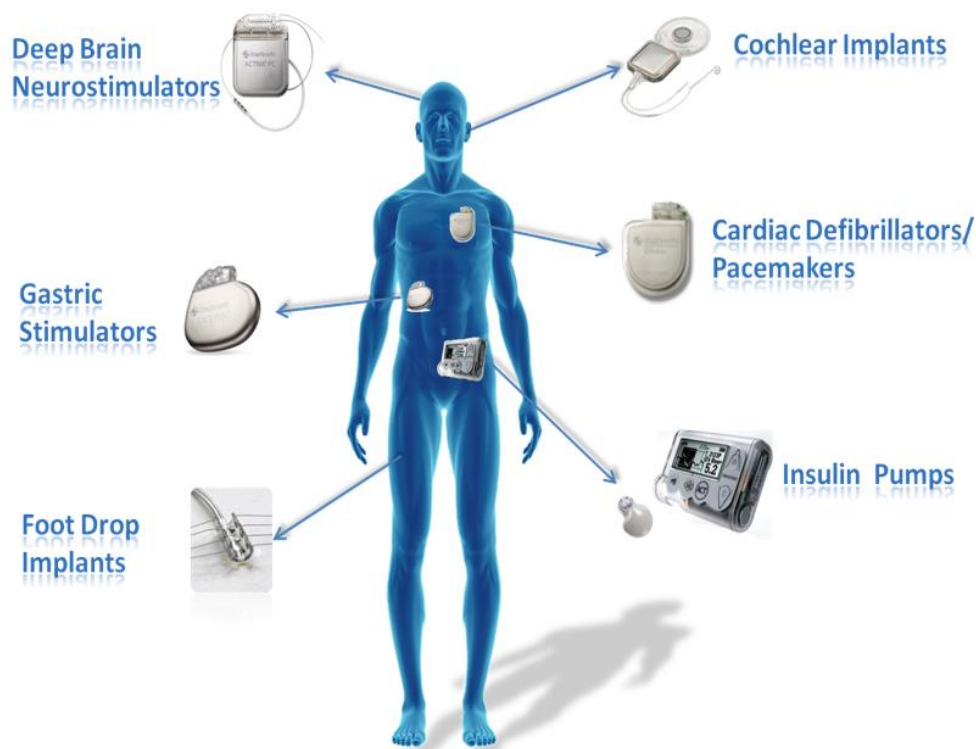


Figure 1.1 Common implantable medical devices. All except one - foot drop implants - require battery technology to operate. Modified from [68].

This research will make it possible to integrate a power source that converts mechanical energy to electrical energy and uses that energy to supply most IMDs on account of the high power generated when compared to currently available devices. The process will provide a roadmap for many laboratories to move from the conceptual and simulation phases to the operational phase by use of a SIPS. Thus eliminating the need for the current approach; that is, placement of a battery inside the body, which will eventually be removed when its life-time has

ended, subjecting the patient to dangerous and expensive procedures that may set them back financially and compromise their health by the inherent risks of post-surgical infection and complications[10].

The problems stated above beg for a solution which can actually be reached through the completion of the work proposed. By using an electromagnetic generator whose rotor is moved by the action of a notched turbine, induced energy, in the form of time-changing sinusoids, can be rectified and stored in a capacitor and conditioned for use by an IMD.

It is the author's belief that in the not-too-distant future, many individuals with genetic predisposition to certain diseases will benefit from continuous monitoring that is only possible by the use of multiple sensors placed intra-corporeally as depicted on Figure 1.1[15]. Once implanted, these sensors can be permanently powered by a SIPS and may signal the presence of certain markers that indicate the early development of certain diseases, such as cancer, Alzheimer's, diabetes, high blood pressure, heart disease, ovarian cancer and liver cancer, etc. Alzheimer's patients particularly may benefit from continuous GPS monitoring that is able to pin-point their location at all times. It is lamentable that many individuals are given a terminal prognosis simply because the disease was not detected early enough to implement the necessary treatment.

This scenario can become a thing of the past if multiple sensors (Figure 1.2) can be implanted for early detection of many treatable diseases, especially those for which the patient has a family history or a genetic predisposition. The development and application of this technology will spur the expansion of a new field that can be appropriately termed personalized continuous preventive telemedicine (PCPTM).

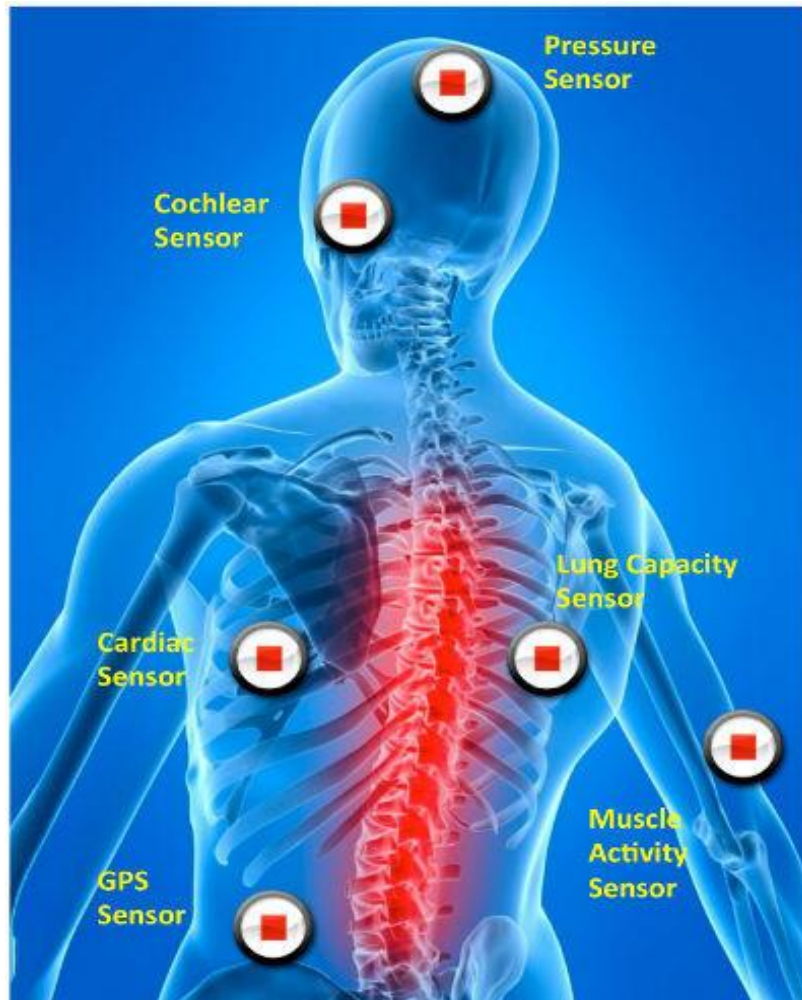


Figure 1.2 Multi-sensor network for early detection of diseases and continuous monitoring of known conditions[19].

It is not uncommon for certain individuals with a family history of breast cancer to undergo a prophylactic radical mastectomy as a preventive treatment. Even though this is an effective way of preventing the incidence of cancer, according to [16], it is impossible to remove all of the breast tissue that could become cancerous. It is not surprising then that 10% of these patients still develop breast cancer and have to be treated with radiation and/or chemotherapy only after the cancer has developed into a palpable tumor or has been detected through a blood test that indicates the presence of a specific marker.

These markers are simply proteins that can be detected in the blood of the patient, such as, CA15.3 used to find breast and ovarian cancer[17].

The proposed system would power an array of LOC (lab on a chip) sensors that would continuously test the blood for abnormal marker levels[18], thus eliminating the need for radical procedures that sometimes are justified, but often are fomented by cancer phobia.

The diagram of Figure 2.2 shows the many possibilities proposed by [19] for energy extraction from various sources. Of these only thermal, vibration, RF and motion are candidates for implantable devices. The thermal energy gradient device necessitates placement near the surface of the skin, which makes it dependent on the environment. Therefore, the constant and stable generation of power may be hampered due to changes in temperature associated with the individual's surroundings, severely restricting the power extraction ability of the generator.

Vibration devices in the form of piezoelectric transducers that operate continuously have also been proposed[20], but have not demonstrated to generate enough power to sustain the operation of any IMD, since their power production is only a few microwatts.

Radiofrequency (RF) harvesting is the topic of continuous research for systems that require very little power, but it is not always possible to maintain certain signal strength around the body, which also absorbs some of the signal before it reaches the transducer, rendering the system useless as an implantable generator.

## **1.2 Research Objectives**

The notched-turbine micro energy generator (NTEG) is a novel system developed at the AMBIR group at USF which produces 750 mW of power as a 3.5 X prototype, at low pressures and moderate angular speeds[6].

The main objective of this research is to integrate the NTEG with a power conditioning circuit, making it possible for it to power an IMD without the need for a battery. This requires that the NTEG be miniaturized to an implantable size and that its performance be optimized by changing its configuration and casing in a novel manner, as follows:

1. A single-magnetic-ring NTEG may be modified as a dual-stator, dual-rotor generator to produce a power increase up to double its power output.
2. The NTEG's casing is redesigned to separate the coils from the rotating magnetic ring, thus preventing the fluid that impacts the rotor from entering the coil space and avoiding damage to the coils and fouling of the blood in the rotor cavity.
3. The coil-ring configuration is modified to allow growth of the coils in the outward radial direction, increasing the current induction capability of the generator with a minimal increase in volume and producing a divergent-induction power source. In other words, the power increases as the coils grow in the outward radial direction. This term is basically an analogy loosely based on the concept of the divergence of a vector field.
4. The modified NTEG is integrated with a rectifier circuit and an energy storage device such as a capacitor or inductor and the stored energy is properly conditioned by means of a switched power control circuit to supply an IMD.
5. The integrated system is tested in-vitro and its ability to power an IMD is demonstrated.
6. The system may be tested in-vivo, and its ability to power an IMD is demonstrated.

### **1.3 Contributions and Relevance of Research**

The above stated objectives represent innovations that improve the NTEG and make it possible for the proposed system to be used as a symbiotic intra-corporeal power source (SIPS) which – as far as the author is aware- is capable of a ten-fold increase in available power when compared to any implantable generator currently available in industry or in academia[7], [8].

The relevancy of the proposed research can be readily seen by the fact that of all the IMDs that have been implanted and are currently in use to date, none is powered by a perpetual power source such as the proposed SIPS. Therefore those devices that require electrical power are supplied by batteries that will eventually need to be replaced.

Even though it is possible to recharge these batteries through the skin by using a transcutaneous wireless power transfer system[9], such systems still present multiple disadvantages that cannot be overcome unless the device is redesigned to eliminate the battery as the main source of power. Only then it is possible for the IMD to draw the power it needs from the energy already available inside of the body in which it is implanted.

The novel contributions of the SIPS in this work clearly show that although many approaches to solving the problem of continuous power have been proposed[10], they do not present a complete solution. Please see section 3 (Background) of this work for an overview of some of these systems and how they may be improved to satisfy the power requirements of most IMDs.

### **1.4 Organization**

This work is organized in the following manner: Chapter 1 focuses on the introduction to this body of work by driving home the relevance of the research and the proposed system.



Chapter 2 presents the background information necessary to understand this work and presents new terminology and concepts that are unique to understanding the same, as well as the fabrication methods available at the time of its completion.

Chapter 3 covers preliminary results stemming from the characterization of the generator proposed for harvesting energy from flow, while chapter 4 presents the design and simulation of the symbiotic intra-corporeal power source (SIPS) and the necessary circuits for rectification and voltage boosting to the level appropriate for use by an implantable medical device (IMD).

Chapter 5 covers important concepts of the human circulatory system and how they are pertinent to this work. Chapter 6 covers the methods proposed for use to test validity of the research and chapter 7 presents the design and fabrication and assembly of four different turbines used to determine the power response of the system at different levels of miniaturization.

Chapter 8 presents the testing process for each of the turbines used and chapter 9 shows the results obtained from testing every turbine using three specific fluids, nitrogen gas, water and simulated blood and analyzes the results. Finally, chapter 10 summarizes and draws conclusions on the results found in chapter 9 and discusses the potential areas for future works stemming from this research.

## CHAPTER 2: BACKGROUND

The human body is a rich source of energy and as such, the proposed system will demonstrate a specific and efficient way to harness it and convert it to electrical energy, which can then be used to power most IMDs. Although many an approach has been taken to address the need for electrical power inside the human body, to the author's knowledge, these have not been successful in demonstrating the generation of enough power to sustain continuous operation of most IMDs in the market. These technologies will be discussed in the current section, along with a comparison with the proposed system to highlight the differences with, and advantages of the SIPS. The notched turbine micro-generator from which the SIPS is derived will also be discussed.

### 2.1 Implantable Power Sources and Generators

At this juncture, it is important that the differences between power sources and generators be clearly explained. A generator can be understood as a device able to convert one form of energy to another. In low power applications it is known as a transducer, and it simply produces what can be termed as "raw power" that cannot be readily used by a working device. For this power to become useful, it needs to be rectified and conditioned to maximize the power transfer to a loading circuit. The generator then needs to be coupled to the conditioning circuit through a process of integration that transforms the generator into a power source[21]. Although an extensive research effort has been mounted in the area of implantable generators (MEMS micro-generators, piezo-electric generators, and electromagnetic generators) both in industry and in academia, the effort is lacking in the area of implantable power sources.

The proposed SIPS is a system designed for cross-coupling to the cardiovascular system for energy harvesting, and to the IMD of choice for energy supply.

This symbiotic process is shown in Figure 2.1 and it allows for a unique mutually beneficial relationship between the cardiovascular system (CVS) from which the energy is extracted and the power source that conditions and delivers this energy at a specific location that ultimately benefits the system from which the initial energy came. A concrete example of this relationship can be seen when the proposed system is used to power a cardiac defibrillator, where the main organ of the CVS (the heart) pumps the blood through the turbine section of the SIPS.

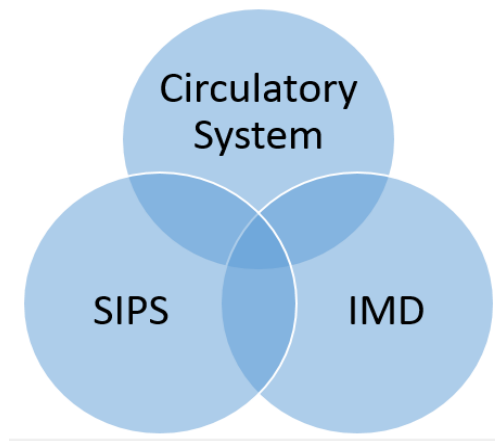


Figure 2.1 Symbiosis of the SIPS

Following rectification and storage, the energy is delivered to the defibrillator which is able to analyze the heart's EKG (electrocardiogram) and correct any abnormal rhythm by “shocking” the heart with just the right amount of energy to convert the rhythm to a normal one or stop it all together and allow the heart's own electrical impulse to start anew in an organized manner. It can then be said that there is a symbiotic relationship between the CVS and the SIPS. This research is important because as it turns out, all active (requiring electrical power) IMDs in operation to date are operated by transducers (generators) that convert chemical reactions to

electrical power, called batteries. These generators lack something very important: perpetual operation through the lifetime of the IMD, whether the device operates in continuous (constant power delivery) or discontinuous mode (on-demand power delivery)[22].

### **2.1.1 Implantable Power Generators**

In this section, several implantable power generators are presented and their output is compared to the power requirement of the IMDs available in the market. It is important to keep in mind that the power output claimed by these devices is “raw power”, while the power requirement of the IMDs is “treated power” or “conditioned power” as would be available as an output from a power source. (See section 4.2)

The generation of power inside the human body is a highly researched area of biomedical engineering, which has produced four main types of harvesting transducers, such as chemical, thermoelectric, piezoelectric and electromagnetic, as well as a plethora of implantable power generators. The following sub-sections are dedicated to the analysis of these generators and how they can be improved to meet the power needs of most IMDs.

### **2.1.2 Chemical Implantable Power Generators**

The most commonly used implantable generator to date is the chemical generator, otherwise known as a battery. The battery is able to convert chemically stored energy to electricity when a REDOX chemical reaction takes place inside the battery’s cells. These batteries already pack a specific amount of potential chemical energy at the moment of implantation and are rated, for a given application (pacemaker, defibrillator, glucose sensor, etc.) to last 5, 10 or 15 years. These times are only ratings and it has been widely documented[23] that they are frequently replaced before the rated time, since the healthcare system (due to safety concerns) will not allow for the complete exhaustion of the battery before replacing it.

Powering implantable devices with batteries is therefore not in the best interest of the patient, since the procedure to replace it can be dangerous, costly and may negatively affect the patient's wellbeing both physically and psychologically. But this is the only option available today. These batteries do satisfy the power needs of all IMDs, but only temporarily. Both intracorporeal batteries need to be made to last longer than the lifetime of a patient to be acceptable as the ultimate energy solution that is actually needed and proposed in this work.

This is not actually possible at this time, since only nuclear batteries can actually comply with this requirement, but have been eliminated as an implantable power source option by the medical community due to its inherent risks and dangers[24].

### **2.1.3 Thermoelectric Implantable Power Generators**

The thermoelectric effect tells us that there is a linear relationship between the current flowing in a conductor and the heat felt on the surface of such conductor. Additionally, this process can be reversed; that is, the temperature difference between two pieces of metal connected by the wires of a galvanometer will produce a current that can be detected as the galvanometer's needle is deflected, which is called the Sebeck effect that is used to create the thermoelectric generator (TEG) described in [3]. The greater the difference in temperature between the two conducting plates, the greater the generated current.

For the implantable TEG in [12], the greatest temperature differential was found to be near the surface of the skin. But even though the power generated is sufficient to power the IMDs with lowest consumption, such as, cardiac pacemakers, it is not enough energy to power the mid-range and high consumption devices, such as, insulin pumps and cochlear implants.

#### **2.1.4 Piezoelectric Implantable Power Generators**

The piezo-electric effect is also a major area of research that continues to investigate ways to convert changes in mechanical stress of a piece of material to electricity. This is possible because certain materials, known as piezoelectric, will create a voltage potential across electrodes when subjected to pressure or vibration. Since the optimal pressures and vibrations necessary for maximum power extraction are normally above the levels produced inside the human body, these generators tend to be very inefficient and not very practical as implantable systems. One possible way to remedy this inherent condition is to use muscle movement to activate a high-frequency mechanical oscillator to which the piezoelectric device is coupled. These vibrations can then be converted to electric power that can be conditioned for use by an IMD.

#### **2.1.5 Electromagnetic Implantable Power Generators**

Two main types of implantable electromagnetic generators (EMG) have been proposed in the art, which convert mechanical motion into electricity by the process of electromagnetic induction. These are:

1. The wound coil (traditional winding), where a copper wire is wound around a magnetic core which increases the magnetic permeability of the coil, thus ensuring a flux increase through the coil, which maximizes current induction.
2. The micro-fabricated coil, which is usually fabricated through a MEMS process and consists of copper lines that spiral out from the center of the coil to a specified outer diameter. Even though these coils are very small and can be easily implanted in the body, they are not very efficient, since the power produced by a coil is largely dependent on factors that are greatly affected by the geometry of a MEMS coil.

These factors include the wire's resistance, the cross-sectional area transverse to the magnetic flux, the wire length (and number of turns  $N$ ), the wire's cross-sectional area, the damping factor and the coil impedance.

All these factors can be understood at the light of Faraday's Law, which states that when a conducting wire is exposed to a time-changing magnetic field, an induced voltage (proportional to the number of field lines that cross the wire) can be measured between the ends of the wire. In other words, the potential difference  $V$  in Eq. 2.1 represents the changing magnetic field with respect to time.

$$V = - d\theta/dt \quad (\text{Eq. 2.1})$$

If the wire is wound into the shape of a coil, then the field lines will cross the wire  $N$  times, where  $N$  is the number of turns of the wire, and  $V$  will increase proportionally. If the wire is wound several times in a stacking fashion, the flux links with all the wire loops in the coil then by integration over the area of each loop, a total potential difference can be found. If a load  $R_L$  is then connected to the ends of the coil, a current will flow.

This current, like all currents in a wire will create a magnetic field that will oppose the field that created it, giving rise to an electromagnetic force  $Emf$ . When the magnetic field lines (flux) moves across the coil and the lines link with the wire orthogonally, the  $Emf$  is maximized and the mechanical energy that caused the magnetic field to change (move across) is transformed into electrical energy (current flowing in the conductor). This maximization of energy conversion depends on the angle of linkage, the speed of change of the field and the opposing force created by the flowing current; this opposition is called damping,  $Emd$ .

$$Emf = Emd * dx/dt. \quad (\text{Eq. 2.2})$$

The generator proposed in this work is of the type described and its configuration is presented in section 3.1, where the induced voltage across the coil terminals varies directly w.r.t. the speed of the rotor, which comprises the permanent magnets that produce the flux.

As the speed of the rotor increases, so does the induced voltage. Conversely, the greater the magnetic field density  $B$  (determined by the strength of the magnets) the greater the induction. Additionally, it can be stated that the greater the  $N$ , the greater the damping. Therefore, there is a limit since the increase in the  $N$  will also cause the coil's resistance ( $R_c$ ) to increase, causing the current flow and subsequently the  $Emf$  to decrease. The power delivered to the load  $P_L$  is proportional to

$$P = V^2 / (R_L + R_c + j\omega L), \quad (\text{Eq. 2.3})$$

where  $R_c$  will dominate the coil impedance at the low frequencies (below 500 Hz) expected when the proposed SIPS is placed inside the human body.

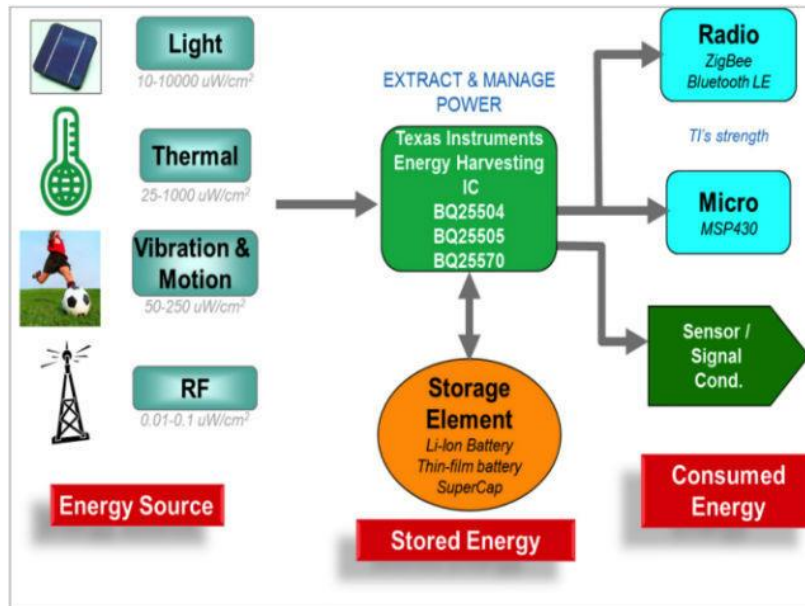


Figure 2.2 Typical energy harvesting systems[19].



### **2.1.6 Radioisotope Implantable Power Generators**

During the decade of the 70's much soul-searching went on as scientists struggled with the idea that in order to keep a patient alive, it was necessary to place a nuclear battery inside of them to power electronic IMDs that could either defibrillate their heart to allow for the termination of a disorganized rhythm and the commencement of an organized one (defibrillator), or send a continuous signal to the heart muscle when the sino-atrial or atrioventricular nodes failed (a pacemaker). Although a number of patients today still have nuclear systems implanted in their bodies, this practice was soon discontinued after the development of the lithium ion battery. The dangers of having a radioactive material inside the body were all too real and had to be discontinued. Today we face a similar danger from the lithium ion battery which must be replaced, not by a more efficient battery, but by a generator that makes the IMD a self-powered device capable of continuous operation beyond the lifetime of the patient. But gauging the lifetime of a person can be rather difficult, if not impossible, since a young person's lifetime would be potentially longer than that of a middle age or advanced age one with the same condition. This is why a battery does not really qualify as a solution to the problem of whether an intra-corporeal system is capable of supplying power beyond the lifetime of a patient.

### **2.1.7 RF Transcutaneous Induction Power Generators**

In this work it is recommended that any harvesting of energy from the flow of blood in the cardiovascular system be limited to no more than 10% of the capacity of the heart. But this restriction does not apply to transcutaneous induction power generators (TIPG) since they don't qualify as an energy harvesting system, but they need to be considered here since they address the same problem of powering IMD's without the use of a battery.

TIPGs work under the principle that a coil outside of the body is set as an antenna that transmits a sinusoidal carrier signal of a certain frequency and another coil inside the body acting as a receiving antenna passes the energy to an energy conditioning circuit that makes it suitable for use by an IMD[100]. This transfer of energy across the skin (transcutaneous) has the advantage of not being limited by the output of the heart, so in theory it can achieve high power outputs in the order of 1-10 W[101], which is enough to power all low-power and most high-power IMDs such as LVADs. But there are drawbacks as well; according to [102], the transfer of power across the skin has to deal with changes in the dielectric characteristics of the skin due to changes in the interstitial fluid's electrolyte balance, adipose tissue variability (which changes the thickness of the skin), movement and displacement of the implanted coil due to scar tissue formation among others.

TPIGs can be used to transfer both power and information across the link established between the two coils, but two separate frequencies must be used, and tuning the coils can be time consuming and cumbersome even with the use of sophisticated lab equipment that is not available to the end-user patient. This is why this technology is listed as dependent on extracorporeal power sources and equipment on Table 2.1.

## **2.2 Fabrication Methods**

The fabrication of implantable medical devices is a very rigorous endeavor that requires the use of biocompatible materials that have become standard in the production of such systems, as they have withstood the U.S. Federal Drug Administration (FDA) approval process.

It is important to be clear that our goal in this work is not to seek such approval, but to demonstrate a proof of concept that is necessary to proceed to more lofty goals outlined in the future works chapter.

The subsections below describe the different manufacturing processes available to our team. Each affords a certain level of benefits and drawbacks of which cost is probably the most significant.

### **2.2.1 Computer Numeric Control (CNC) Machining**

This manufacturing process allows a computer program to control the manufacturing tool. It is a top down process where a grinder (or any other applicable tool) removes material from a block until the desired shape is achieved [69].



Figure 2.3 Computer controlled machining (top-down process)[69].

The tool is capable of operating at different angles, depending on the number of degrees of freedom, thus obtaining a 3-dimensional object with good resolution. Figure 2.3 shows this process in action, allowing for higher accuracy and faster production than a human operator would achieve. This process can be used on different materials, such as metals, wood and plastics. In this work CNC was used to manufacture only the casings of the turbines, but not the blade assembly, due to the complexity of the part.

### **2.2.2 3D Printing**

This manufacturing process uses a bottom up approach where layers of material are deposited on a fixed platform until a 3-dimensional structure is erected. The material is

extruded from a hot nozzle that melts the threaded filament and moves to a particular position following a Cartesian coordinate system. The sales of 3D printers has skyrocketed in the past decade, as prices drop and the printing quality improves. Figure 2.4 shows this trend.

The two most commonly used materials are ABS, derived from petroleum and used widely in industry, especially on automobiles, and PLA which is biodegradable, but more brittle than ABS.

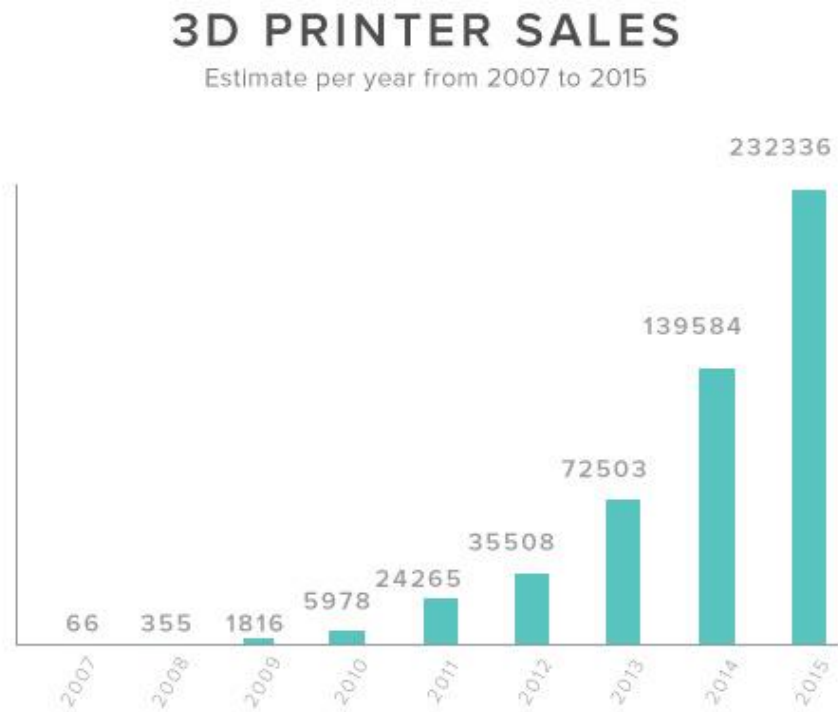


Figure 2.4 Trends in 3D printer sales from 2007 to 2015 [70].

### 2.2.3 Selective Laser Sintering (SLS)

This process is also a bottom up process in which a laser is used to melt a material in powder form, allowing it then to cool and solidify. This process is repeated until a 3-dimensional part is built from the ground up. This process is used widely in rapid prototyping, but sometimes the resulting part has to be treated to achieve higher surface smoothness and better structural integrity[71].

#### **2.2.4 Stereo Lithography Apparatus (SLA)**

SLA is also a bottom up or additive approach to manufacturing where a container filled with a photo-sensitive material (polymer resin) is irradiated with a UV laser to harden the material at very specific points. The laser is controlled by a computer that reads the CAD STL file that describes of the part being produced[72].

The SLA process is able to achieve great surface smoothness and detail, but it is limited on the types of material (metals for example) that it can process.

#### **2.2.5 Vacuum Casting**

This process is much more involved than the ones previously discussed, since it involves the making of a silicon mold where the hot metal or polymer such as polyurethane can be poured. Prior to the pouring the mold is evacuated to prevent the formation of air pockets or trapped gases that would compromise the integrity of the part. The labor intensity of this process makes it more costly than SLA, SLS and 3D printing, but the quality of the finished part is of higher order and the choice of materials is more extensive[73].

#### **2.2.6 Injection Molding**

This process is the precursor to any casting process because it delivers a finished mold that can be filled with the molten metal, plastic or polymer of your choice. Many IMD parts are now made in this manner using biocompatible materials from metals to polymers and plastics.

This allows for mass production of parts, thus reducing the cost associated with the more traditional CNC machining process[74]. Injection molding works well with small parts such as the turbines considered in this work, but it is more costly than using a 3D printer or using limited CNC machining, which are both available at USF.

### 2.3 Justification of Research

Figure 1.1 shows the most common implantable medical devices in use today, some of which require electrical power to operate. Of these, in 2011, implantable cardioverter defibrillators alone accounted for 133,263 procedures at an annual cost of \$5.5 billion, with a cost per procedure of \$40,000, while heart pace makers accounted for 235,567 implantations at a total cost of \$4.5 billion and a cost per procedure of \$20,000 [25].

Medical care costs continue to rise every year and it is expected that the costs of surgical interventions to place these devices will continue to rise every year. Additionally, the inherent problem of device tethering to extracorporeal or intra-corporeal power sources continue to cause unavoidable complications (stemming from the replacement of the device due to exhausted batteries), such as increased rate of infections that can lead to yet more device replacements.

This turns into a vicious cycle because the replacement process increases the infection rate and the recommended treatment for infection is device replacement, all the while increasing the cost of treatment and the threat to patient survival. This research presents an elegant solution where this vicious cycle of device re-implantation, repeated infections and increased care cost can be avoided[26]. The proposed SIPS offers a framework for a single implantation surgery over the life of the patient, thus improving two very important factors: the healthcare cost and the quality of life to the patient.

Table 2.1 shows the state of the art in power generators for energy harvesting. These systems are diverse in the source of energy that they convert and in the method used for conversion. But all convert some sort of energy (kinetic, thermal, solar, infrared ultrasonic and radio frequency) into electrical energy by use of a transducer (piezoelectric, electromagnetic, thermoelectric, photovoltaic and resonating circuit).

Although some of these produce a high power output, they are not implantable because their size is too large, as seen with the piezoelectric foot transducer described in [27] or the EM induction generators from [28].

Other systems although implantable, are restricted by their inability to operate continuously; such is the case of the piezoelectric system embedded in an orthopedic implant that converts the energy produced while walking to electricity. This means that some patients would not be able to benefit from this technology if their IMD requires a continuous supply of power for operation. One potential solution would be to use a rechargeable battery is charged during daily walking periods. But if the patient is unable to walk for a certain period of time due to injury or illness the system would not function as intended. Other systems exhibit a dependency on an extracorporeal source (DECS) for their operations, such as, thermal, solar, infrared, ultrasonic and radio frequency[27]-[30].

Table 2.1 State of the art generator types and comparison with proposed system.  
Adapted from [37].

Energy Source	Harvesting Method	Power	Advantages	Disadvantages	Reference
<b>Kinetic Foot pressure</b>	Piezo	1 W	Very high power	Not implantable	[27]
<b>Kinetic (Fluid flow and Pressure)</b>	EM Induction	0.75 W	High power, low fluid shear stress, notched turbine.	Large size, Not implantable	[28]
<b>Kinetic: Orthopedic implant pressure</b>	Piezo	4.8 mW	Implantable	Generation of energy requires walking, dependency on extracorporeal source (DECS)	[29]
<b>Kinetic: Blood pressure fluctuations</b>	Piezo	2.3 $\mu$ W	Implantable	Very low power	[27]
<b>Kinetic: Vibration driven generator-VDRG</b>	Electrostatic	80 $\mu$ W	Implantable	Pre-charge voltage source needed, low power	[30]

Table 2.1 Continued.

Energy Source	Harvesting Method	Power	Advantages	Disadvantages	Reference
<b>Kinetic:VDRG</b>	EM Induction	400 $\mu$ W	No separate voltage source	Maximum voltage 0.1 volts	[31]
<b>Kinetic: VDRG</b>	EM Induction	400 $\mu$ W	Tested in-vivo: Pacemaker on dog	Generator maintained 1.6 volts for 30 min at 200 BPM (high heart rate)	[32]
<b>Thermal</b>	Seibeck effect TEG	30 $\mu$ W		Limited power range, Environment dependent	[33]
<b>Solar</b>	Solar cells	647 $\mu$ W	Not intimately invasive, moderate power	DECS, Not practical	-[67]
<b>Infra-Red</b>	Photovoltaic cells under the skin	4mW	High power	Battery recharging system (not perpetual), DECS	[34]
<b>Ultrasonic</b>	MEMS resonator	21.4 nW	Safer than RF, no interference.	Power too low, DECS, slow.(0.9 volts in 15s)	[35]
<b>Wireless radio frequency</b>	Transcutaneous Induction link	150 mW	High Power, no battery needed	Limited carrier frequency due to tissue absorptions, patient mobility restricted due to DECS	[36]
<b>Cardiovascular pressure and flow</b>	EM Induction	417 $\mu$ W	Tested in-vivo (ICD on pig)	High shear stress turbine and casing materials favored thrombi formation	[7]
<b>Cardiovascular pressure and flow</b>	EM Induction	10 mW	High power, low shear stress axial notched turbine, perpetual, flexible integration, implantable, no DECS	Not yet tested in-vivo.	<b>Proposed work.</b>

This limits the device's ability to work as intended if the conditions for conversion are not present, such as the correct temperature differential between the inside and outside surfaces of the patient's skin as is the case of the thermal transducer. The solar transducer is implantable just under the skin to allow for the photoelectric effect to take place as the light travels through the skin. This may be dependent on the melanin concentration and may not work for every individual.



If the solar cells are mounted extra-corporeally such as on sunglasses, the generated energy could be transferred to a cochlear implant wirelessly or through a contact at the mastoid process behind the ears where the legs of the glasses usually rest.

This would require the use of materials that can prevent the growth of microorganisms and their penetration into the body at the skin-device boundary. This development would greatly benefit patients with ventricular assist devices (VADs) that require a minimum of 8-10 watts to operate, which is only possible with a power line that penetrates the skin and connects to the VAD, not to mention the millions of patients that undergo dialysis, placement of chest tubes or post-surgical drainage system on a daily basis.

The cardiovascular generator from [7] is similar to the SIPS since it draws power from the same source, the hydrodynamic energy of the circulatory system. But this is where the similarities end, since it uses a tesla turbine with a series of disks that causes hemolysis (destruction of red blood cells) due to the high shear forces to which they are exposed[38]. The turbine was tested in-vivo, but only operated for approximately 15 minutes before it stopped due to the blood coagulation response caused in part by the hemolysis. This is avoided in the SIPS design by using innovations such as the notched blade and distributed pressure flow[28]. Additionally the generator was only able to produce approximately 4% of the power claimed by the SIPS. Table 2.2 indicates that this Tesla generator would be able to power only a couple of the devices listed, while the SIPS could potentially power 100% of them.

It is clear then that the proposed system has the necessary characteristics to ensure continuous operation that does not depend on extracorporeal events or sources and does not need a battery to operate or to maintain a charge.

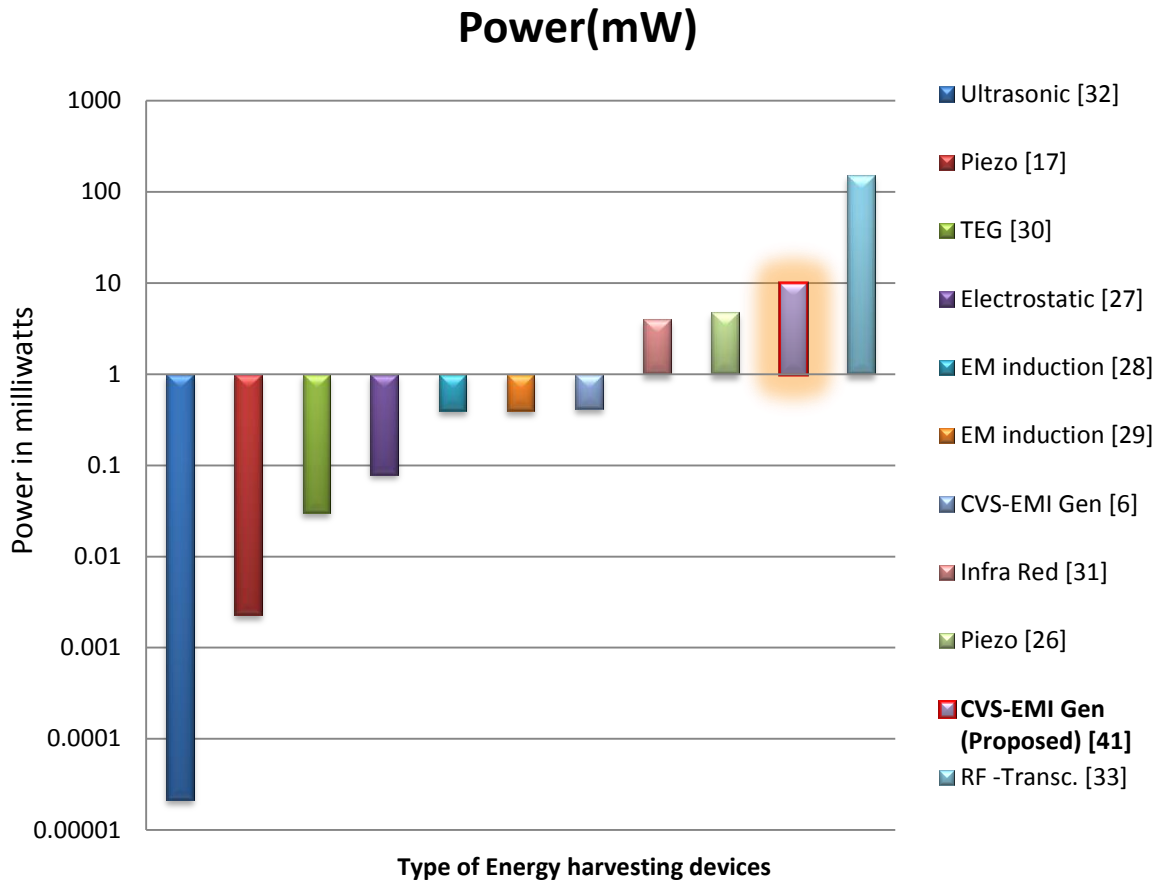


Figure 2.5 State of the art generator types and power comparison with proposed system.

The proposed SIPS is then in a separate category characterized by continuous and perpetual operation in the milliwatt range and has built-in flexibility to power one or potentially multiple IMDs simultaneously. Figure 2.5 shows a comparison between the different generators of Table 2.1 in terms of power production and type. Notice that the scale is logarithmic and the proposed system is shown highlighted in an orange glow on the right side of the figure.

Only one other system[6] can be directly compared to the proposed system since both use a turbine for harvesting electrical energy from the CVS by use of an EMI generator. Both advantages and disadvantages are considered on Table 2.1.

Table 2.2 Power requirements of most commonly used IMDs[39].

implanted device	typical power requirement
pacemaker	30–100 $\mu$ W
cardiac defibrillator	30–100 $\mu$ W
neurological stimulator	30 $\mu$ W to several mW
drug pump	100 $\mu$ W to 2 mW
cochlear implants	10 mW

The ultrasonic system has the lowest power production and the wireless RF, a transcutaneous power transfer system, is shown at the top. But it suffers from serious limitations, such as limited frequency of operation (due to absorption by the skin) and the dependence on extracorporeal conditions position and orientation of the external coil with respect to the implanted coil. An external power source is also needed to power the external coil, making the proposed system preferable.

## CHAPTER 3: PRELIMINARY STUDIES AND RESULTS

The results obtained up to now include, the bench-top characterization of the micro-generator, a 3-phase, 12 pole, 6 magnet asynchronous generator that is capable of producing enough power to source multiple IMDs simultaneously. Additionally, the design and simulation of the power source and conditioning circuit (PSAC) and Power Boosting Circuits is presented and analyzed, as well as its frequency analysis to determine the necessary impedance matching for maximum power transfer.

### 3.1 The Power Generator

In this project, a one-inch hard-disk drive motor is used as a 3-phase asynchronous brushless generator is used to produce raw power.

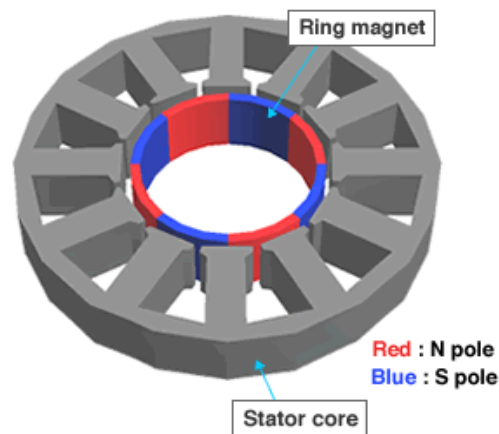


Figure 3.1 Armature and magnetic-ring configuration.

The cartoon of Figure 3.1[40] shows the configuration of the coil armature with respect to the magnetic ring. Notice that by placing the magnetic ring in the center, the coils extend outward radially allowing for a divergent induction system (DIS). One great advantage of the DIS as opposed to the outward-ring, convergent induction system (CIS) used in [28], is that the rotor (and magnetic ring) can be made smaller, and therefore, the turbine can also be reduced in size and weight. Therefore, not only is the motor's diameter reduced by a factor of 3 with respect to [28], but the rotor's diameter is also reduced by a factor of 2, allowing the turbine's diameter to be reduced by a factor of 6, not to mention the depth. This is a very significant contribution, because the turbine's speed is inversely proportional to its mass, according to Newton's second law of motion. The turbine (and the generator's rotor) with a smaller mass will then move faster, and the induced voltage will increase proportionally.

The micro-generator, when rotating at a specific RPM, will produce a sinusoidal signal at each of its phased outputs at a frequency that is directly proportional to its speed of rotation and number of its magnetic poles. This behavior can be described by the equation,

$$f [\text{Hz}] = \text{RPM} * P / 120, \quad (\text{Eq. 3.1})$$

where P is the number of poles (North and South) in the magnetic ring oriented as shown in Figure 4.2[40], and the quotient 120 is a conversion factor ( $60 * 2$ ) that converts RPMs, or revolutions per minute to Hertz or cycles per second, given that there are 60 seconds in one minute and that two passes of alternating N – S poles are necessary to complete one sinusoidal cycle of the output signal. In our specific case, since the magnetic ring is a 12 pole ring,

$$f = \text{RPM} * 12 / 120, \text{ or simply } f = \text{RPM} / 10.$$

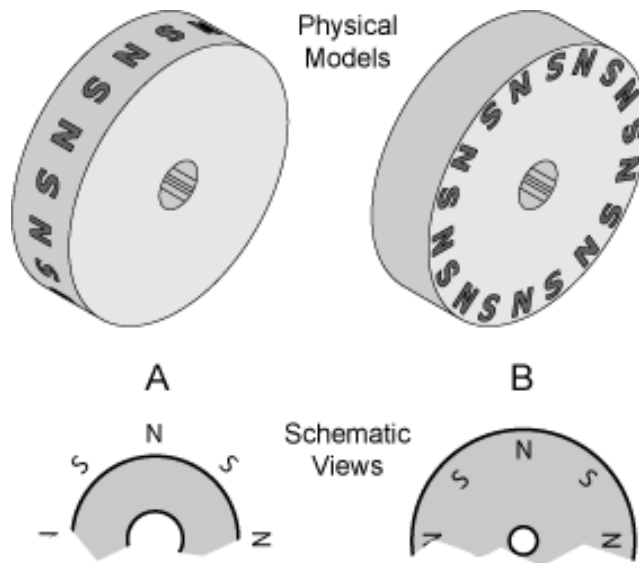


Figure 3.2 Permanent magnet orientation

### 3.1.1 Bench-Top Characterization

The characterization of the 18.5 mm (0.74 in) motor shown below in Figure 3.3, was conducted by connecting its coil terminals to the test circuit shown in Figure 3.4. The rotor (9.4 mm) and coil armature have been separated and are shown next to a dime (17.9 mm) for better visualization and size comparison.



Figure 3.3 Actual generator armature and rotor next to a dime for size comparison.

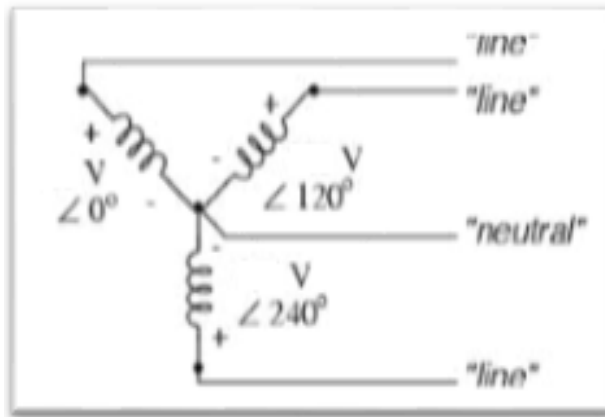


Figure 3.4 Three-phase generator coil set up

The 9 armature coils compose 3 sets of 3 coils each that are connected internally. The 3 coils of the first set are connected in series and their voltages are added since they receive induction simultaneously. The second set receives induction 120 degrees apart from the first, and the third set 240 degrees apart from the first or 120 degrees from the second. Figure 3.4 shows this relationship with each output voltage  $V$ , measured between the corresponding “line” and the “neutral” points. The neutral is a reference wire that is connected to all 3 sets and acts as a ground, but can be obviated if any two phased outputs are taken in series. In this case, the outputs add up to less than twice the individual phase outputs, since their peaks do not exactly match in phase and only add constructively over part of the period of the sinusoid.

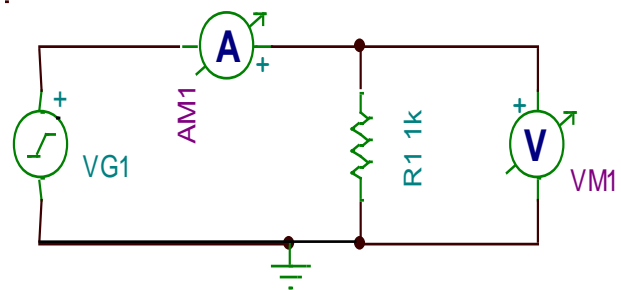
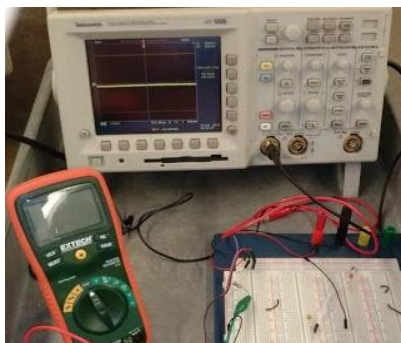


Figure 3.5 Test circuit used for generator characterization

The motor was connected in generator mode by coupling the rotor to a VM 16 Milltronics programmable drill capable of maintaining constant rotational speeds from 0 to 8,000 RPM. The rotor was set to rotate in increments of 500 RPM.

Table 4.1 shows the open circuit voltage obtained from one coil set with respect to ground (V low) and in series with the contiguous phase (V high). The corresponding currents I-low (using a single phase) and I-high(two contiguous phases) through a 10.1  $\Omega$  purely resistive load were also measured with an XTECH True RMS multi-meter. A Tektronix T DS 3052 oscilloscope was also used to verify the sinusoidal shape, frequency and amplitude of the voltage and current output by connecting it in parallel with the open-circuit coil and in parallel with the load.

Table 3.1 Induced voltage and current[65].

<b>Generator Bench-Top Characterization</b>				
<b>Rotational Speed</b>	<b>No Load Voltage (Open Circuit)</b>		<b>Load: R Ohms</b>	<b>10</b>
<b>kRMP</b>	<b>Vlow AC</b>	<b>Vhigh AC</b>	<b>Ilow AC mA</b>	<b>IhighAC mA</b>
0.5	0.04	0.07	2	3
1	0.117	0.205	6.39	8.08
1.6	0.189	0.327	10	12
<b>2</b>	<b>0.22</b>	<b>0.385</b>	<b>12.4</b>	<b>14.5</b>
2.4	0.242	0.426	13	16
2.6	0.263	0.46	14	17.3
3	0.348	0.607	18.43	22.88
3.3	0.383	0.668	20.28	25.11
3.6	0.419	0.73	22.5	26.8
3.9	0.448	0.781	23.8	29.27
4.4	0.48	0.83	25.15	31.11
4.5	0.52	0.905	27.4	33.7

The case study presented in [7] describes an implantable Tesla turbine and generator able to produce 0.4 mW of power at 1770 $\pm$  237 RPM and pressure differential of 37.8 $\pm$ 5.4 mmHg when connected to the circulatory system of a 60 Kg domestic pig. These findings clearly show



that the circulatory system of a higher mammal (including humans, since it is closest to the pig's in anatomy and physiology[41]) can maintain the pressure and flow necessary for a small millimeter turbine to rotate at above 1000 RPM. It can be seen from the data in Table 3.1 and a simple power calculation that the SIMS would be able to approximately double this output under similar conditions as untreated power alone.

Theoretically, the SIMS would also be able to supply energy to up-to 6 independent power sources that can supply energy to at least one different IMD each. Although the proposed work does not call for a demonstration of these capabilities due to scope constraints, the SIPS versatility and potential for expansion is definitely established and presented as a future works topic.

### **3.1.2 Linearity**

The measurements taken from the table are plotted below and show that the micro-generator has a very linear response to changes in RPM as seen on Figure 3.6.

This is important because it gives one a clear picture when selecting an operating point around the constant systolic/diastolic fluctuations in blood pressure that are inherent to the circulatory system. The figures below show the linearity of the induced voltage, both  $V_{high}$  and  $V_{low}$ , as well as the currents  $I_{high}$  and  $I_{low}$  flowing through a  $10.1 \Omega$  load, where  $V_{high}$  and  $I_{high}$  represent the voltage and current from two contiguous coils whose phases partially add constructively, as opposed to  $V_{low}$  and  $I_{low}$  where only one coil is used.

## **3.2 Frequency Response Analysis**

The frequency response of the generator was analyzed with a VersaSTAT4 model 400 frequency analyzer. One coil set (single phase output) was connected to the analyzer as the frequency was changed from 0 to 100 KHz. The coil's impedance components  $Z_{-real}$  and  $Z_{-$

imag, as well as the phase angle were then obtained and tabulated. Table 3.2 below shows the results. Additionally, the RPM corresponding to each frequency was calculated using Eq. 3.1.

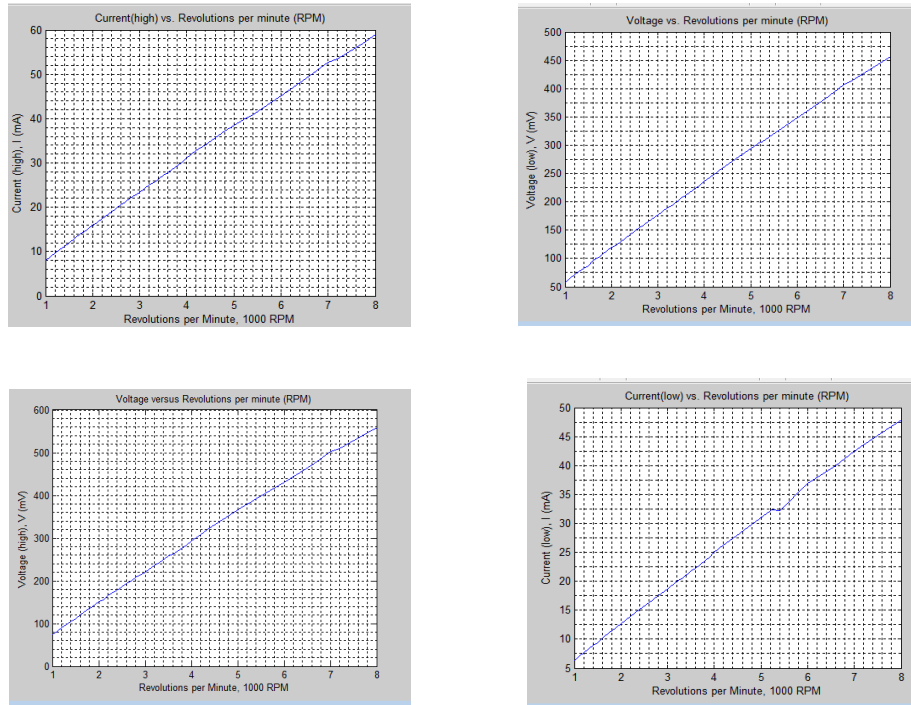


Figure 3.6 Voltage (top) and current (bottom) linear response w.r.t. kRPM

As expected, at low frequencies, the coil's impedance was found to be real and the percent difference between the magnitude of the total impedance  $|Z|$  and  $Z$ -real are negligible. This percent difference will only be approximately one tenth of 1% for any of the three phased outputs, as measured with respect to ground. Notice that the phase change is also negligible at very low frequencies around 126 Hz, or the equivalent 1260 RPM.

As the frequency increases, though, this difference becomes more significant and any impedance matching circuit must include an imaginary component if maximum power transfer is to be achieved. One of the constraints inherent to any cardiovascular generator is that there is a limit as to how fast the turbine is able to rotate.

The peak speed of blood in the abdominal aorta of an adult male can be as high as 222 cm/s and 131 cm/s in the pulmonary artery[42], and since the typical rotational speed of a VAD (ventricular assisted device), a proven system in bio-medical engineering is between 7,000 and 12,000 RPM[14], [43], then it is safe to set 2500 RPM as an appropriate limit for our design. Even though the blood is able to flow at the resulting 117.8 cm/s, the appropriate pressure difference will allow for operation at a lower speed which is enough to generate the needed power in accordance with Bernoulli's principle.

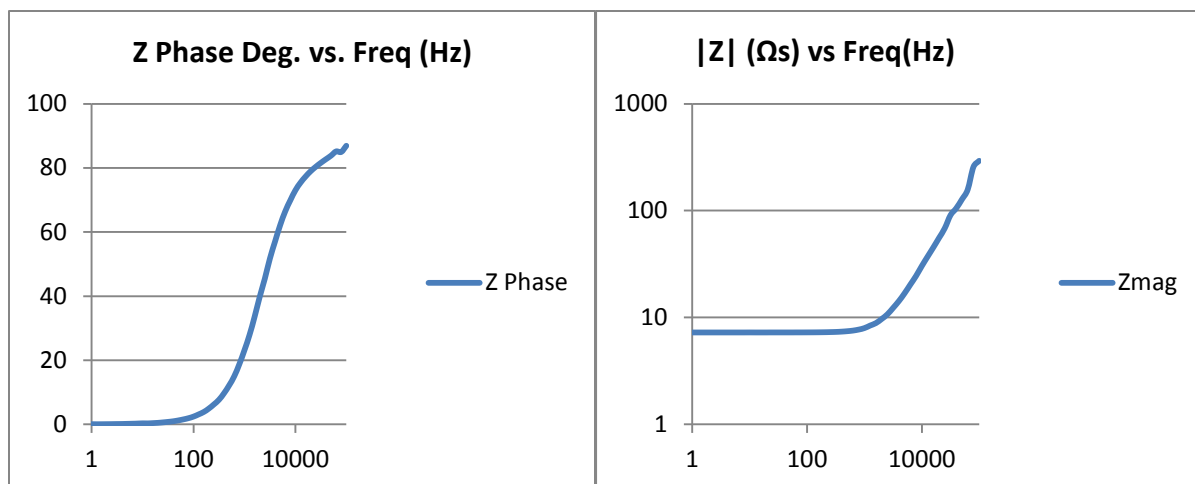


Figure 3.7 Generator's phase and impedance measured with respect to frequency in Hz.

Figure 3.7 shows the Bode plots of this analysis which shows a low impedance close to 10  $\Omega$  for frequencies below 10 KHz.

### 3.3 Slip Analysis and Characterization

In this work, an 18.8 mm synchronous permanent-magnet motor is connected in generator mode to the notched-blade turbine described by Thomas, Cabra and Pérez in [6]. In this way, the turbine's rotor is connected to the generator's rotor and the armature (stator) coils are connected to the generator load.

Since the generator is no longer synchronized to a stator-specific frequency like the motor was, it is termed an asynchronous (induction) permanent-magnet brushless generator able to induce a voltage into its coils when its rotor is moved by the coupled turbine.

Table 3.2 Calculated RPM from generator's frequency response and percent difference between  $|Z|$  and Z-real.

RPM	Frequency (Hz)	Z Phase	Zmag	%Diff. Z-real & $ Z $
10000	1000	23.13	7.95935	8.37%
7943.28	794.3282	18.7816	7.71127	5.47%
6309.57	630.9573	15.0074	7.54423	3.47%
5011.87	501.1872	12.1617	7.44418	2.27%
3981.07	398.1072	9.71716	7.37504	1.45%
3162.28	316.2278	7.66803	7.32918	0.90%
2511.89	251.1886	6.21161	7.3035	0.59%
1995.26	199.5262	4.91185	7.28232	0.37%
1584.89	158.4893	3.85159	7.27079	0.23%
<b>1258.93</b>	<b>125.8925</b>	<b>3.10152</b>	<b>7.26304</b>	<b>0.15%</b>
<b>1000</b>	<b>100</b>	<b>2.41602</b>	<b>7.25723</b>	<b>0.09%</b>
<b>794.328</b>	<b>79.43282</b>	<b>1.91782</b>	<b>7.25406</b>	<b>0.06%</b>
630.957	63.09573	1.54752	7.25175	0.04%
501.187	50.11872	1.22457	7.25009	0.02%
398.107	39.81072	0.95714	7.24901	0.01%
316.228	31.62278	0.77091	7.24831	0.01%
251.189	25.11886	0.61283	7.24761	0.01%

Additionally, since this generator will be used as an implantable power source coupled to the cardiovascular system of a higher mammal; and the cardiac cycles of systole and diastole continuously change the blood pressure in the circulation that moves the turbine, then the induced sinusoid will be also variable, both in frequency and in amplitude since the induced voltage (and its frequency) is proportional to the speed of change of the magnetic field that produces it (as stated in previous sections).

In any power generator it is important to track any changes in voltage, phase and slip. The voltage, which is the electric potential or force able to move electrons in a given direction is a common measurement. Not so well understood, the phase and slip are comparisons between two different signals, where the phase is the separation of the peaks or valleys of two signals in degrees or radians.

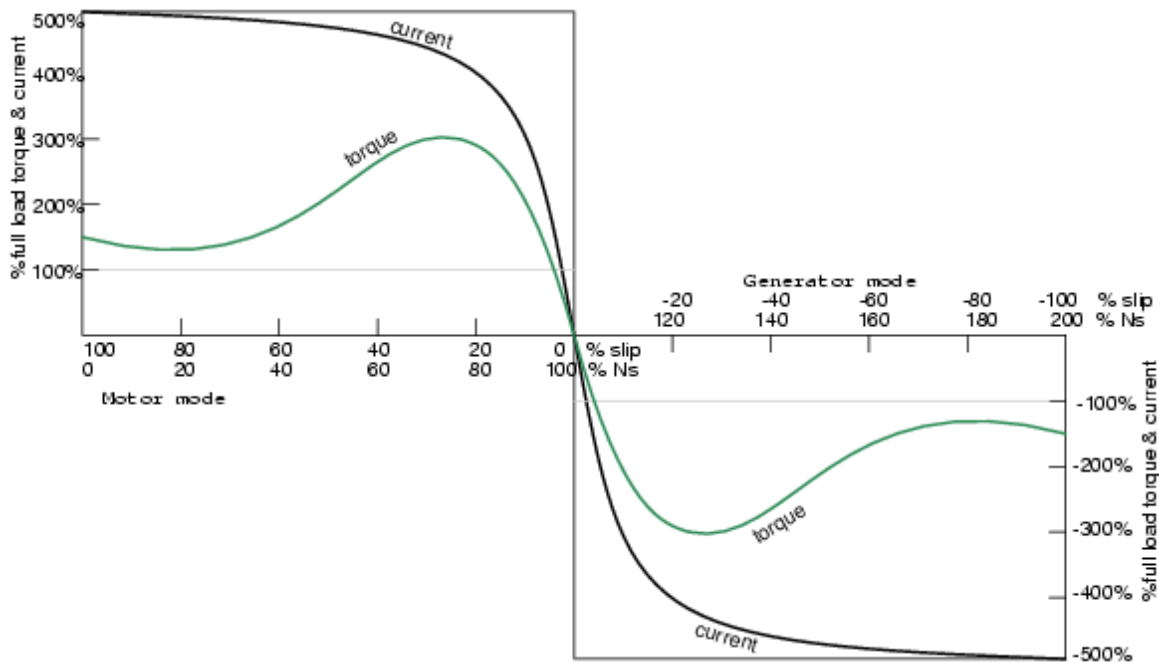


Figure 3.8 Motor & generator modes of an electric machine. Torque and current vs synchronous speed ( $N_s$ ) and slip[75].

In our case, three sinusoids are generated all of which are separated 120 degrees from the next. The slip (in a typical synchronous or asynchronous generator) is a measure of the frequency difference between the frequency of the rotor (shaft speed,  $\omega_r$ ) that rotates past each armature coil and that of the resulting induced signal seen at the armature coil terminals (synchronous speed  $\omega_s$  – the speed at which the rotor, in a traditional generator, is synchronized to the grid).

The slip (see Figure 3.8[44]) is a number between 0 and 1 that reveals: 1) Whether the device is operating as a motor (positive slip) or as a generator (negative slip) 2) In large generators connected to the grid, it shows whether or not the power generator is synchronized to the grid 3) In wind turbine generators, it indicates whether enough power is being extracted from the system.

For the microgenerator used in this work, the author is only concerned with the fact that the device is capable of operating as a generator when rotating at the variable speeds provided by the circulatory system (approximately 500 to 2500 RPM). Obviously, the speeds in the 500 to 1000 RPM range will not induce as much voltage into the coils, but it is necessary to consider the entire range as a measure of the potential of the SIPS to manage small amounts of energy and convert it into useful power.

The specific operating speed range will be determined by the location of implantation, which will be discussed in later sections. The slip equation,

$$s = (\omega_s - \omega_r) / \omega_s \quad (\text{Eq. 3.2})$$

shows that when the rotor speed,  $\omega_r$  is the same as the synchronous speed  $\omega_s$ , the rotor is idle and there is no induction and no torque, as is seen in Figure 3.8[45]. When  $\omega_r$  increases past  $\omega_s$ , the machine works as a generator and is able to produce power or convert the torque experienced by the turbine into useful electrical energy.

It can be seen from the graph of Figure 3.9 that the slip of our generator is appropriately negative. The points on the graph were obtained by measuring the frequency  $f_s$  (in Hz) of the signal induced at one of the stator coils and using slip Eq. 3.2, with the rotor speed  $\omega_r$  obtained from Eq. 3.1.

In order to measure the frequency  $f_s$ , the set up of section 3.1.1 was used with a  $10 \Omega$  load across a single coil of the generator. The frequency was then measured from the coil signal obtained with the oscilloscope.

It must be noted that for a particular generator (or motor), for a small enough slip, between 0 and 0.1, the slip is directly proportional to the torque. And for larger slip values above 0.1, the torque is inversely proportional to the slip[46]. By inspecting the graphs in Figures 3.8 and 3.9, it is important to notice that the slip values of our generator in Figure 3.9 are below 0.1 (10%) and that the graph is actually directly proportional to the torque graph of Figure 3.8. Notice that at the linear part of the slip curve in Figure 3.9 is in the expected RPM operational speed range (500 to 2500 RPM). Since the power is proportional to the torque, the author can expect to extract the power needed to support his hypothesis that the SIMS would be able to power an appropriately chosen IMD.

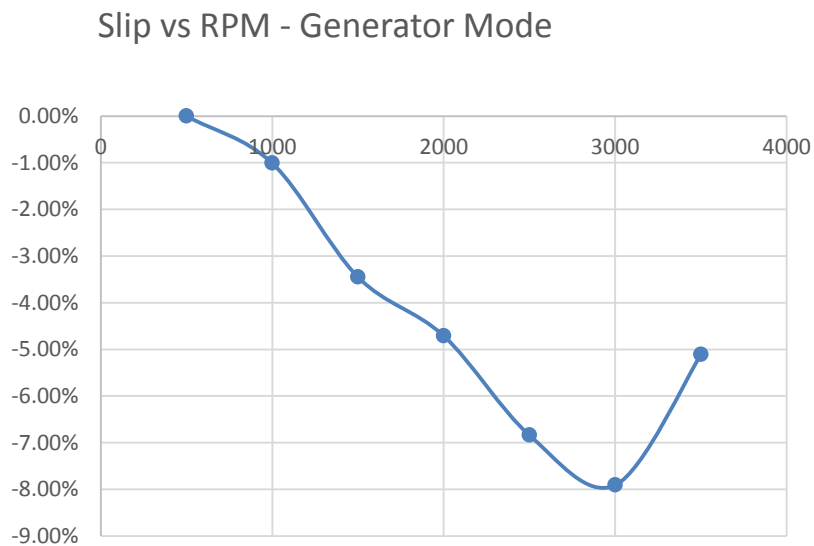


Figure 3.9 Micro-generator single coil characterization shows negative slip with increasing rotational speed using a  $10 \Omega$  load.

## CHAPTER 4: SYMBIOTIC INTRACORPORIAL POWER SOURCE (SIPS) DESIGN AND SIMULATIONS

### 4.1 Overview

In this section, it will be shown how the process of energy extraction from the circulatory system is possible and what implementation options are available to ensure that enough power is obtained to source the IMD of choice. This is a process of integration through which each part of the system is coupled and optimized for implantation, maximum power transfer and efficiency, in that order. If implantation is not optimized, then the other too may be sacrificed to negotiate a suitable operating point that still manages to provide the power needed for as many IMDs as possible.

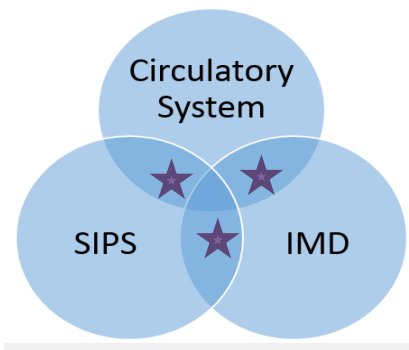


Figure 4.1 Symbiosis of SIPS revisited.

The symbiotic relationship of the SIPS with the circulatory system is revealed for the first time in Figure 2.1. The graph is updated and reprinted in this section as Figure 4.1 for ease of understanding. The intersecting areas of Figure 4.1 (each marked with a star) are explained further to ensure integration.



Notice that the area between the Circulatory System and the SIPS is where the turbine operates, since it is the point of interface between these two areas of the system. In other words, it is where the mechanical energy is transferred to the generator's rotor. Likewise, the area between the Circulatory System and the IMD can be termed Implantable Biocompatible Electrodes (IBE), which is a topic of extensive on-going research in biomedical engineering, but is not a proposed topic of investigation in this work. Suffice it to say that the SIPS provides the necessary energy for many types of IMDs which may require different types of electrode systems.

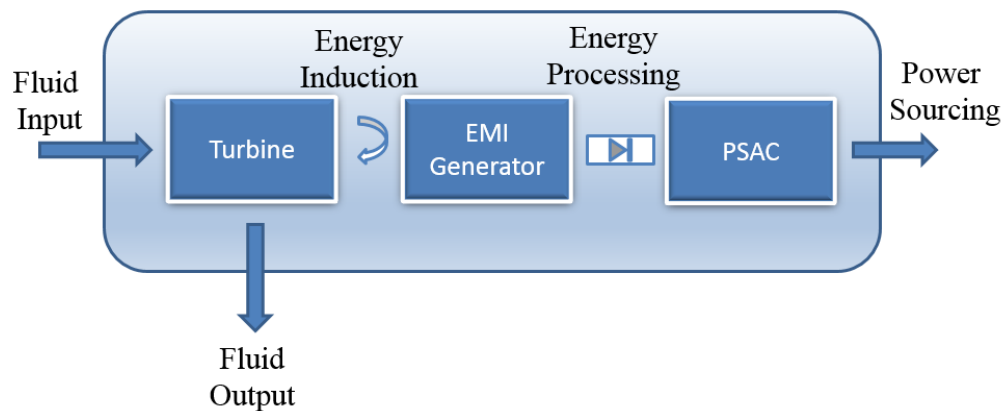


Figure 4.2 SIPS block diagram illustrating integration of its salient features.

The last area to consider, and the one that will be extensively discussed in this work, is that which lies between the SIPS and IMD circles. This area (including the Turbine) is presented as a block diagram in Figure 4.2 below. Here, it can be seen that the circulation of blood (fluid input to fluid output) provides impulse to the notched blades and should maintain a constant flow of blood with only 10% in pressure drop in the circulatory system, as described by Cabra in [28]. If 10 mW of power is extracted, it could also be described as a power harvest of approximately 1 mW per mmHg.

Since two generators' permanent-magnet rings connect to the turbine on either side, the turbine action is balanced and the two rings will rotate simultaneously, in opposite (clockwise and anti-clockwise) directions. The resulting moving magnetic fields then induce a current into the armature coils and each voltage can be measured at the coil ends. This voltage and current will increase with the rotational speed and will need to be rectified, then stored in a capacitor before the output can source the IMD.

The following sections depict different PSAC configurations, and present an analysis of the same, always seeking to minimize the size, maximize power and increase efficiency.

## **4.2 Voltage Rectification**

As it was explained in previous sections, the raw power obtained from our generator has to be rectified and conditioned to accommodate the requirements of the IMD. This AC to DC conversion must be analyzed to ensure that the size of the circuit is minimized and the output DC level is maximized. There are multiple ways to achieve these goals depending on the available real estate and the amount of power needed.

### **4.2.1 Full Rectification**

A full wave rectifier presents the advantage of maximum power extraction, but it will occupy a greater area. Figure 4.3 below[47] shows a typical full-wave rectifier able to extract power with every excursion of the oscillating signal. But notice that for every peak of the sinusoid (positive and negative), two diodes conduct at the same time and there is a double internal loss per phase.

If the generator output is 0.9 volts (see table 4.1), then for a typical diode with 0.7 internal drop, then there is not enough amplitude to support a 1.4 volt drop across two diodes, and the output is zero.

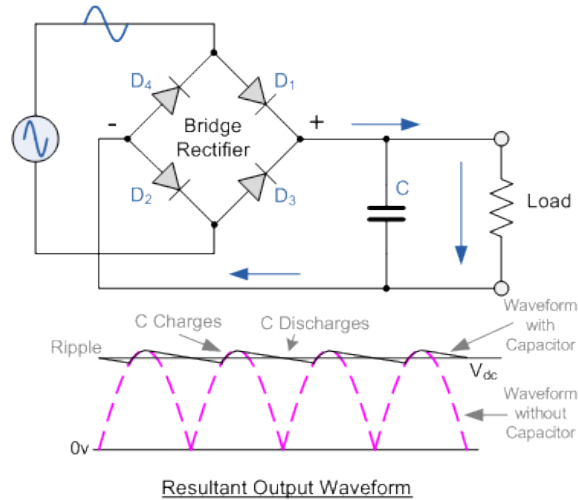


Figure 4.3 One full-wave rectifier per phase.

If Schottky diodes are used with a typical voltage drop of 0.3 volts, then there is 0.3 volts available per phase at the output and 0.9 volts per generator, which becomes 1.8 volts for a dual-generator system. This is still not sufficient to power most an active IMDs such as, a pacemaker, cardiac defibrillator, neurological stimulator, drug pump or cochlear implant[39]. From table 3.1 it can be seen that in order to obtain 0.9 volts out of this generator, the turbine must be able to maintain a rotational speed of 4.5 kRPM, which is not may not be supported by the circulatory system. Additionally, a full wave rectifier per phase with a dual generator system would mean 24 diodes and 6 capacitors, a very expensive proposition in terms of real estate. Therefore, another solution must be explored that would help in minimizing real estate and maximizing power output.

Another approach is to use a 3-phase, full-wave rectifier as shown in Figure 4.4[48]. Here all 3-phases are rectified using a set of only 6 diodes, thus reducing the number of diodes per generator by 6. This is encouraging since the space available for implantable devices is limited and must be reduced whenever possible to minimize the impact on the body.

The problem of two diodes conducting at the same time is still a reason of concern; one that can cause a huge loss at the expense of the output. Another approach is to simply use a half-wave rectifier as a compromise between output power and real estate.

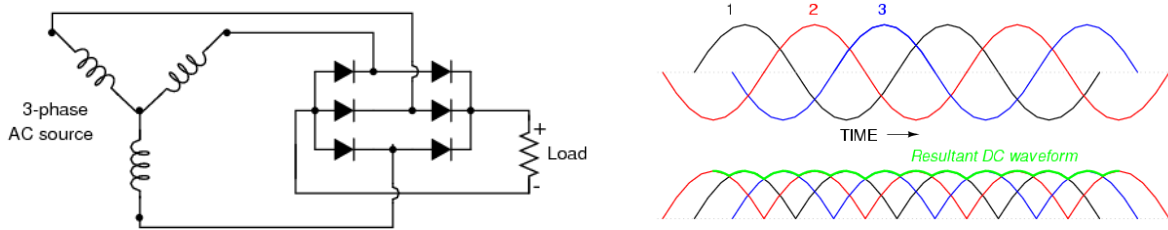


Figure 4.4 Full wave, three-phase rectifier circuit.

#### 4.2.2 Partial Rectification

The most simple circuit to use is a single diode per phase or half-wave rectifier. This would cut in half the internal voltage drop. Using one capacitor per phase would increase the number of capacitors, but the output voltage would also increase as they are added in series. If all the diodes are connected to one capacitor, a drop in voltage is seen since the partially rectified sinusoids are not in phase and their peaks will add constructively only partially.

The standard CMOS source voltage of 3.6 volts seems ilusive, but it is possible to increase the peak amplitude before rectification by using a small transformer. Texas instruments and Coilcraft are two of many companies now focused on producing small discrete and integrated devices designed for use soly in small energy harvesting systems.

It is then possible that by using a small 4 mm<sup>2</sup> transformer such as the Coilcraft LPR4012 in a 1:10 ratio that the needed 3.6 volts can be produced as long as the generator is able to maintain an output of at least 360 mV and the impedance can be matched to that of the generator's. This means that the turbine must maintain a rotation of at least 2 kRPM according

to Table 3.3. This would reduce the current by a factor of 10 though, which may not be optimal for some IMDs.

Additionally, using a 1:10 or higher ratio transformer will require the use of a separate regulation and stabilization circuits that are already found in a DC to DC converter in addition to maximum power point tracking capabilities.

### 4.3 DC to DC Conversion

Figure 4.5 shows the TINA (Toolkit for Interactive Network Analysis) simulation results obtained using a 1:3 transformer and a single Schottky diode. Here, a worst-case scenario is presented where at 1kRPM, the 200 mV output from a single phase of the generator (VG1) will produce an output voltage VF1 equal to 500 mV (without load) in less than 10 msec. The same result can be obtained using a higher RPM and the V<sub>high</sub> output of the generator. The simulation was done with the transformer to highlight the fact that at the lowest end of the RPM spectrum (1KRPM), the output voltage out of one phase (200 mV) is not enough for the BQ25504 to cold start, but it can be brought up to 600 mV by using the transformer. Then subtracting 100 mV drop (at low currents) across the diode, the 500 mV rectified output remains and is stored in the capacitor.

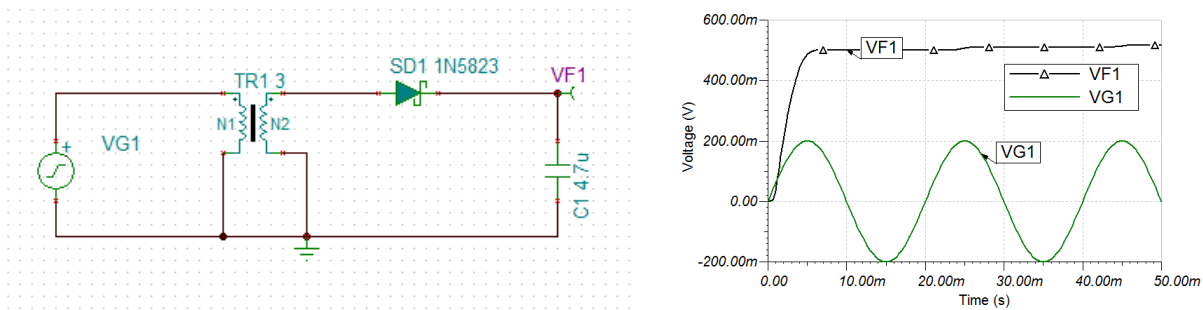


Figure 4.5 P-SAC TINA simulation results with a transformer and single rectifier diode.

Although this 500 mV is not sufficient to power any IMD, it can be converted by use of a tiny integrated circuit, designed specifically for energy harvesting.

One such IC, the BQ25504 is an ultra low power boost converter from Texas Instruments able to produce a 3.6 volt output from a single 330 mV startup voltage, which can be further reduced to a minimum of 80 mV in steady state.

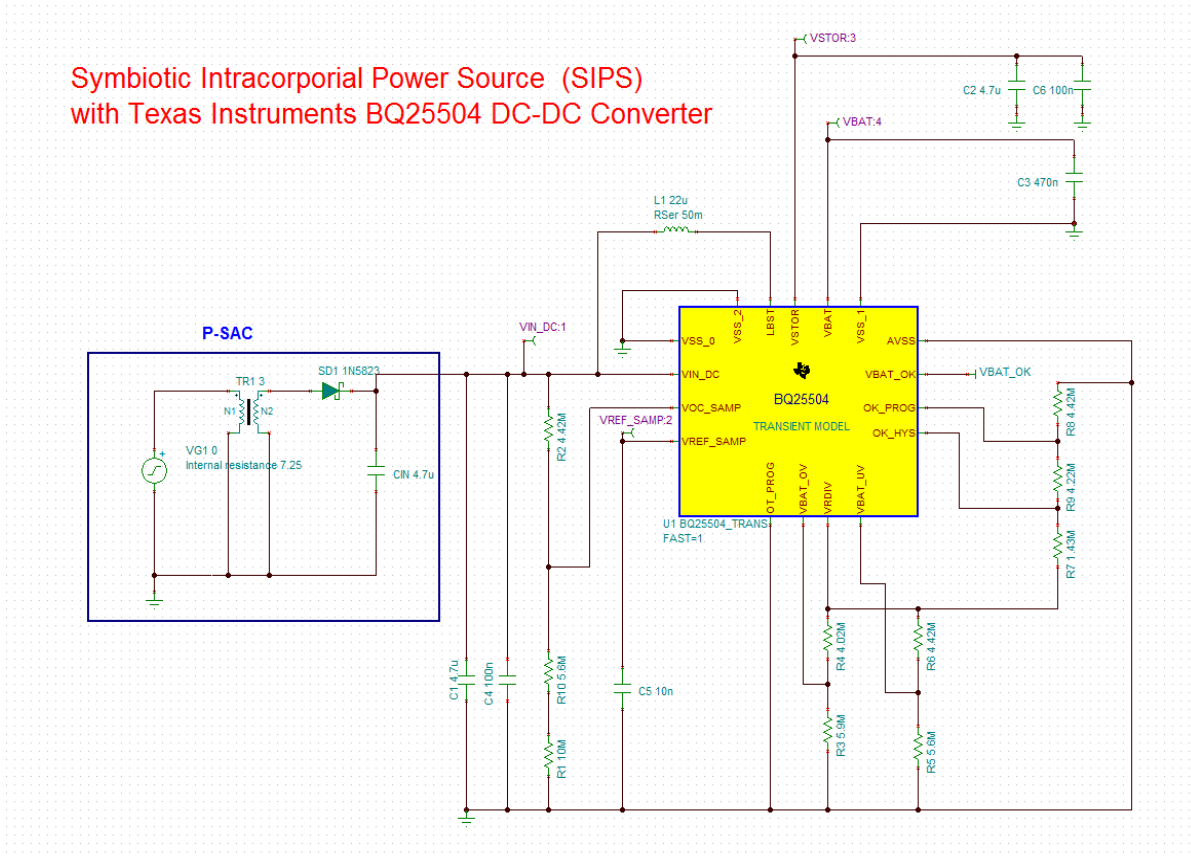


Figure 4.6 SIPS circuit comprising minimized P-SAC and DC-DC converter

Figure 4.6 below shows the proposed circuit and Figure 4.7 shows the simulation results of the DC-DC converter, powered by a single-phase, single-diode P-SAC. This DC-DC converter can be used in many applications (see Figure 2.2[19]) with different types of transducers which cannot be implanted or produce insufficient power to make it a possibility.

The proposed microgenerator integrated into this design by use of the P-SAC and its specifications are presented here. The type is: 3-phase asynchronous induction generator, with internal resistance per coil: 7.25-7.30 at 100-251 Hz (corresponding to 1000 to 2500 RPM).

The output voltage (200 mV at 100 Hz) corresponds to the minimum value of the above range, which corresponds to the voltage measured at two contiguous coils ( $V_{high}$ ), and not with respect to ground.

The maximum power available can be found by connecting a matching load to the output of the generator and measuring the current and voltage at the load. Then by a simple  $V$  times  $I$  calculation the maximum power delivered can be found[49]. Also, the generator's output voltage may not be rectifiable due to insufficient amplitude, which can be remedied by using a boosting circuit that will increase the signal's amplitude.

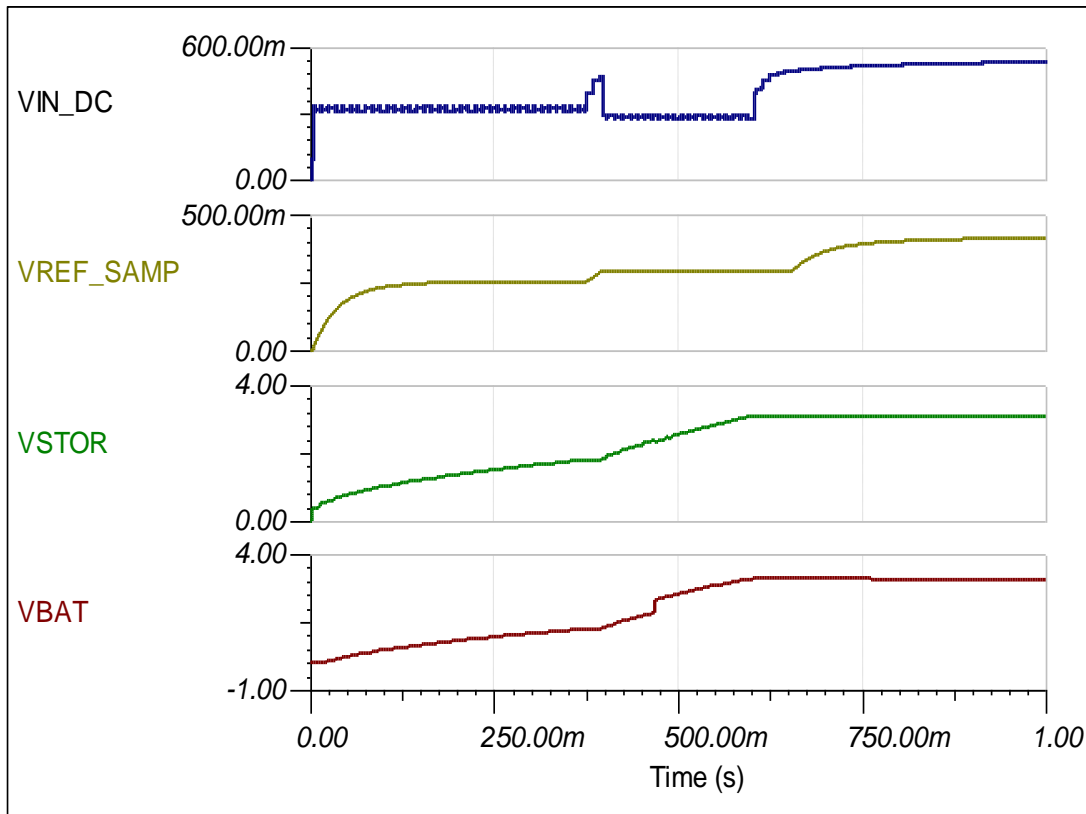


Figure 4.7 Simulation results of SIPS circuit of Figure 4.6

One option is to use a transformer which can be used to boost to a much higher voltage and obviate the need of the DC-DC converter, but transformers used in this manner are much bulkier, incur winding and core losses that produce more heat than is desired in IMD applications. The author will continue the approach of using a DC-DC converter and consider other converters, such as the LTC 3105 and LTC 3108, since they offer the advantage of starting at a lower input voltage than the BQ25504. The circuits above can then be implemented without the transformer by simply allowing the generator to rotate at a higher RPM and by using two contiguous coils in series, producing the higher voltage and current ( $V_{high}$  and  $I_{high}$  in Table 3.1) that are needed.



## CHAPTER 5: HEMODYNAMIC ANALYSIS OF THE CIRCULATORY SYSTEM

The cardiovascular system of a higher mammal is a vast source of energy that supports life not only in the physiological sense through the constant exchange of nutrients and waste products at the cellular level, but mechanically as well, maintaining consistent pressure and flow of the blood. Most of this energy goes unused and can be classified as pressure energy, kinetic energy and volumetric potential energy.

### 5.1 Principles of Blood Flow

The continuous pumping action of the heart (a mechanical pump) in the circulatory system helps maintain pressure on the sides of the vessels and imparts kinetic energy to the blood.

The greatest energy can be seen in the aortic arch as the blood leaves the left ventricle on its way to the major vessels of the body. As the blood moves farther from the heart, the arteries narrow and bifurcate (divide) into smaller arteries, arterioles and finally capillaries, where the exchange of nutrients and waste products takes place.

Since the blood has mass, the kinetic energy that it carries is proportional to  $\frac{1}{2} mv^2$ , where  $v$  is the velocity of the blood. If the diameter of the vessel is decreased, by the law of conservation of mass, the velocity  $v$ , must increase in order to move the same mass through the vessel. The pressure is said that has been converted to kinetic energy. Once past the narrowing part, the flow will resume as before and the pressure increases back to the level prior to the narrowing.

This is a very important application of Bernoulli's principle[51], illustrated below in Figure 5.1[52], where the total energy of flow through a narrowed portion is conserved by converting pressure energy to kinetic energy and vice-versa.

At two different points, P1 and P2 of a vessel with corresponding cross-sectional areas A1 and A2, where  $A_2 < A_1$ , it follows that  $P_1 > P_2$  and velocity  $v_2 > v_1$ .

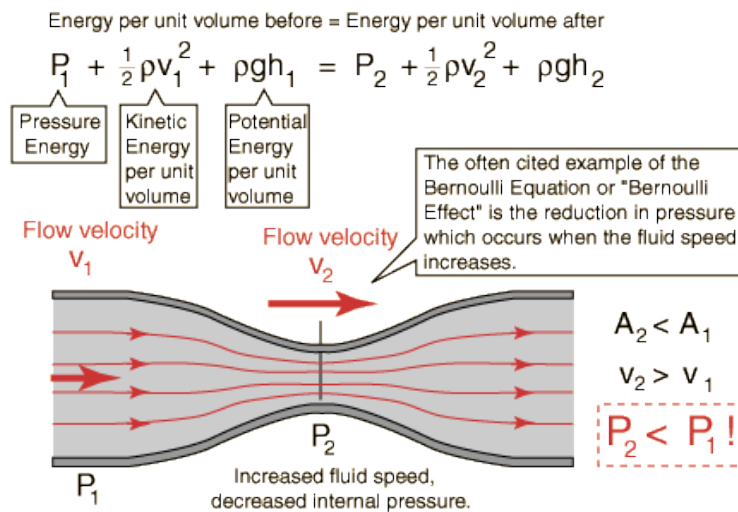


Figure 5.1 Bernoulli's principle of blood flow[76].

The movement of blood in the blood vessels is therefore determined by the pressure difference between to given points. This allows for the placement of our generator in different areas of the body as long as the pressure differential is sufficient to maintain proper flow and sustain turbine action. Figure 5.2[42] below shows a measure of the energy distribution due to both pressure energy and kinetic energy of the blood in the circulatory system. Here both the highest pressure in mmHg and the highest speed in cm/s can be found in the aorta.

From Figure 5.2 below, it can be seen that the average pressure found in the aorta is about 100 mmHg, which is average of the systolic and diastolic pressures, while the average flow rate out of the left ventricle of an adult into the aorta is approximately 5 L/min.

This means that the average power the heart produces can be calculated by the product of the pressure and the flow rate. Using simple conversions into SI unit, a pressure of 100 mmHg is  $100 \times 133.32$  Pa and a flow of 5L/min is  $5 \times (.001 \text{ m}^3/60\text{sec})$ , or  $.0000833 \text{ m}^3/\text{sec}$ , therefore, the power produced by the heart is 1.111 Watts. Using the same rational, the power produced by the heart in one stroke (70 mL) is 15.5 mW. In order to use this power judiciously, a rule of thumb for power extraction can be instituted here, limiting it to no more than 10% of the cardiac output, which means that no more than 111.1 mW should be extracted from the heart's output per minute or no more than 1.55 mW should be extracted per stroke for every beat. On average, the length of a beat is typically 1 second, then 1.55 mJ of energy per second can be extracted from the heart. From Table 2.2 it can be seen that cochlear implants are at the top of the power consumption chain with 10 mW, so in order to power 100% of the devices on the table, care must be taken to store enough energy in a capacitor and use it intermittently if the rule of thumb established above is strictly enforced.

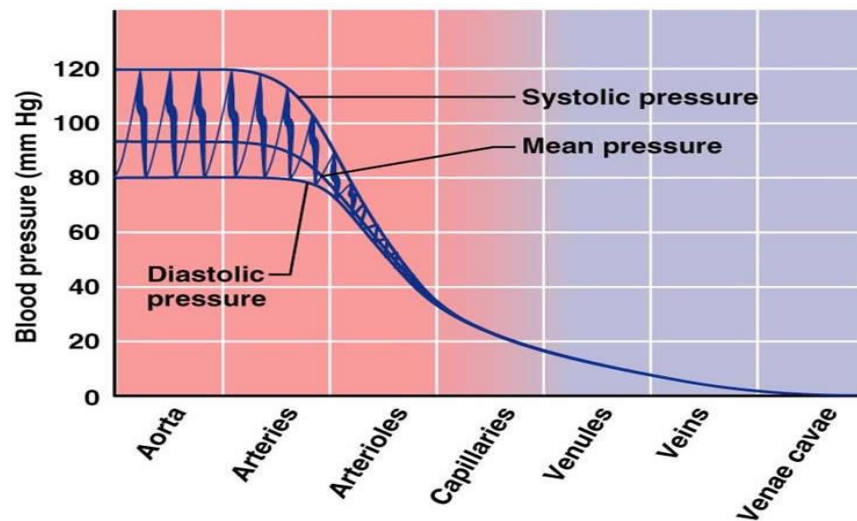


Figure 5.2 Blood pressure levels in the circulatory system[77].

According to Bernoulli's principle, pressure can be converted into kinetic energy thus ensuring that the speed of the flow is sufficient to maintain the proper rotational speed of the turbine as described in previous sections.

The following section explores different ways to connect the turbine to the different vessels of the circulatory system in order to maintain such speed.

According to [28], the 3.5X design of the notched turbine generator will produce a 10% drop in blood pressure when the turbine is connected to a closed-loop system. Figure 5.3 shows the relationship between the inlet pressure and the associated volume flow rate.

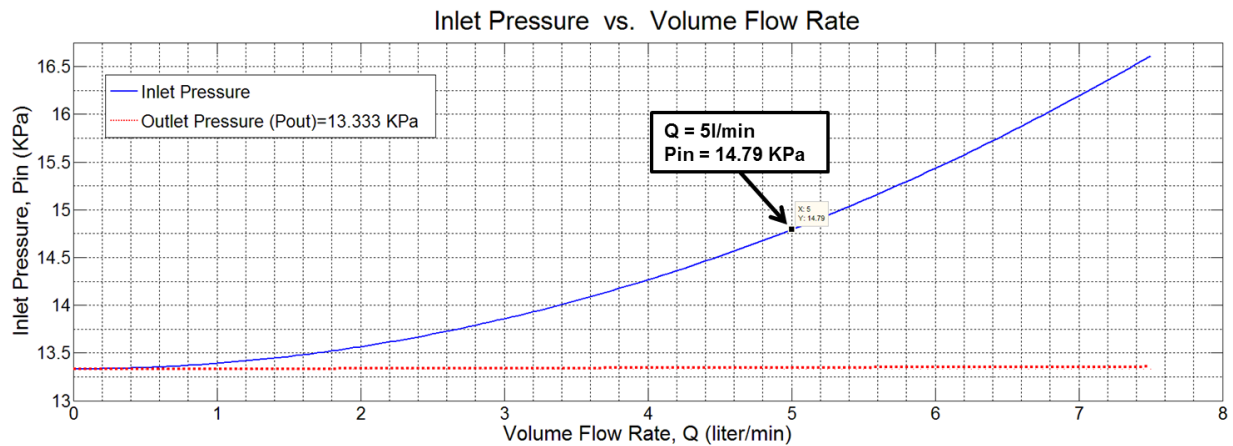


Figure 5.3 Inlet pressure vs. volume flow rate of a notched-blade turbine[28].

Assuming that the outlet pressure is held constant at 13.333 KPa, changes in the inlet pressure will determine how much of a drop the system will experience. The relationship is inversely proportional, that is, the lower the inlet pressure, the lower the drop in pressure to the system.

The small turbine proposed as an integral part of the SIPS would have a much smaller working volume, which may lead to a similar drop in system pressure assuming all other conditions and variables are not changed.

The exact calculation and measurement of this drop will be accomplished as a hemodynamic test bench analysis once the turbine's 3D model is printed.

Additionally, inherent compensatory mechanisms that adjust the blood pressure in major vessels by controlling the resistance of distal vessels must be considered (autoregulation of organ blood flow[53]), since they ensure the correct perfusion of organs within a wide range of blood pressure limits below the normal 120/80 mm Hg defined by the American Heart Association (AHA).

The ultimate decision to implant a SIPS rests with the physician that knows best the patient's history and have ascertained the best course of action for treating their patient.

## **5.2 Anastomoses and Cross-Coupling of SIPS**

In order to covert mechanical energy into electrical energy, the blood in the circulatory system must be diverted into the SIPS' turbine to produce the alternating electromagnetic waves at the stator coils that are then rectified and conditioned for use by an active implantable medical device (AIMD). The input and output to the turbine must then be surgically connected (anastomosed) to the circulatory system in one of several ways, according to the need for power and location of the AIMD. This connection can be made in parallel or in series and will be termed according to the type of vessels with which the connection is made.

## **5.3 Artery-to-Artery Anastomosis**

This is a naturally occurring connection, necessary for the efficient perfusion of important tissues in every higher mammal. The most famous example being the Circle of Willis found at the base of the brain which ensures adequate perfusion to this most important organ in the body[54]. Therefore, the proposed system can be anastomosed by connecting its input to a high pressure artery, and its output to a lower pressure artery as can be seen on Figure 5.4.

It is noticeable that the blood vessels of higher mammals have bilateral symmetry (they run together in vein-artery pairs that bring the blood to the tissues' individual cells and return it to the heart).

This provides multiple potential locations for anastomosis and affords much versatility to the proposed system. The vascular tree shown in Figure 5.5[55] can be used to identify pairs of vessels for possible anastomoses depending on the application.

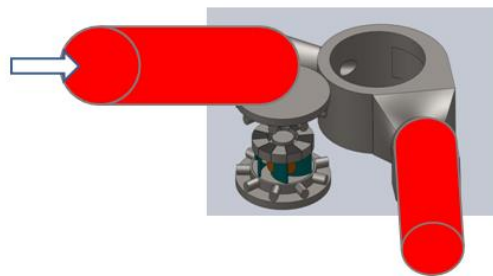


Figure 5.4 Dual stator turbine connection between a high pressure artery (input) and a lower pressure artery (output) with flow direction.

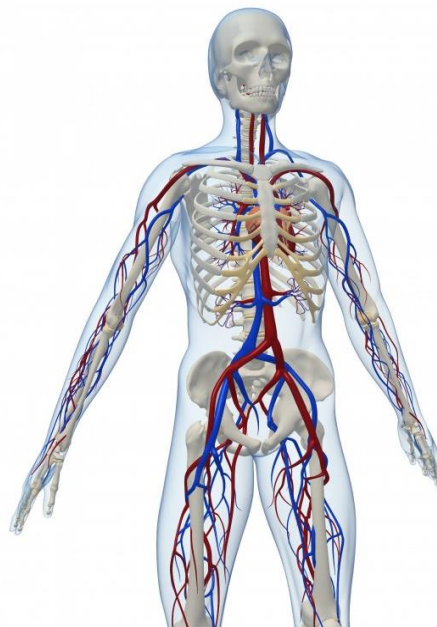


Figure 5.5 Vascular tree of the human body[55].

For example, arteries and veins in the pelvic region can be used to supply the energy for an incontinence device, while vessels of the trunk can be used to power cardiac pace makers, medication delivery pumps or nerve stimulation units to treat a host of conditions that range from chronic pain to drug resistant diabetes [56].

#### 5.4 Arteriovenous Anastomosis

This is a shunt configuration that connects the blood circulating in an artery to that circulating in a vein (Figure 5.6), much in the manner that an arteriovenous fistula is created or an arteriovenous graft is connected to provide access to the circulatory system of patients that require dialysis treatment for end-stage renal failure [57], as can be seen in Figure 5.7[58],[59] below, or surgically made to establish proper connections to extracorporeal support devices during transplantation surgery [60].

It is important to chose a proper location and materials to prevent complications and disturbances to the circulatory system such as embolitic events caused by blood coagulation due to blood pooling or platelet activation due to high shear stress as was found in [7].

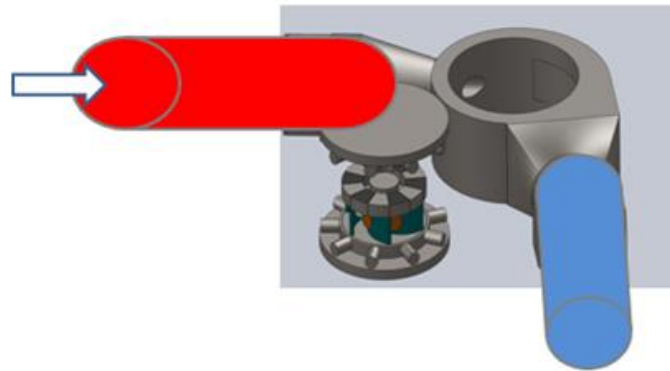


Figure 5.6 Dual stator turbine connection between an artery (input) and a vein (output) with flow direction.

The proper site takes advantage of the high pressure of the arterial circulation and ensures prompt return of the blood to the heart for continued flow to the lungs and throughout the rest of the body.

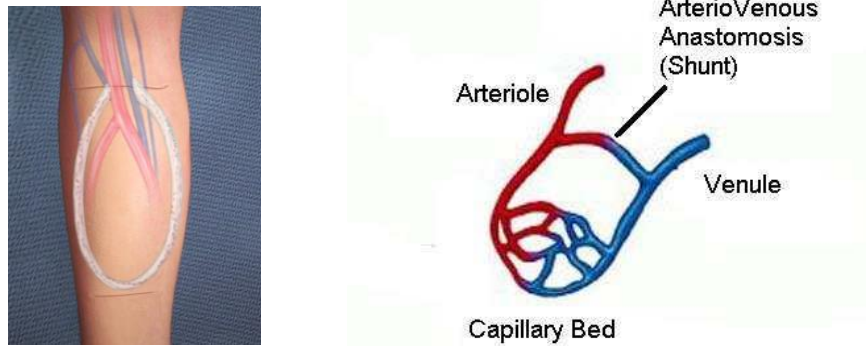


Figure 5.7 Arteriovenous anastomosis (right), and arteriovenous graft (left) [78]

The turbine in the SIPS will see a pressure difference between its input and output, thus ensuring a steady fast flow from the artery into the vein of choice [61]. This flow is indispensable to produce the maximum rotational velocity possible, since the voltage depends on the flux linkage between the magnetic field from the magnets and the coils [10].

## 5.5 Blood Components

The blood is probably the most important fluid in the human body as it carries out very important functions, such as oxygenation of body cells such as the transport of cells that carry O<sub>2</sub> and CO<sub>2</sub> (RBC), fight infection (WBC) and even prevent hemorrhage when injuries occur (Platelets). Blood is composed of plasma and elements of differing forms. In this section those functions are considered very briefly in order to come to a better understanding of the importance of biocompatibility and hemo-compatibility in the design and implementation of IMDs.



### 5.5.1 Plasma

Plasma is a yellowish fluid that makes up about 60% of the volume of whole blood and is composed of mostly water (91.5%), several proteins (7%) and traces of solutes (1.5%) that give it a density of 1.4 times that of water[103].

Plasma is the lifeline of all cells in the body, as it carries the blood cells, oxygen, carbon dioxide, hormones, glucose, clotting factors, and nutrients, just to name a few.

### 5.5.2 Blood Cells

There are three important types of blood cells considered here, the Erythrocytes (~7.8  $\mu\text{m}$  in diameter), also known as red blood cells (RBC) because they give the whole blood its red color, stemming from the iron in their hemoglobin, a specialized protein that is able to grab a hold of molecules of  $\text{O}_2$  and  $\text{CO}_2$  during transportation to and from the body cells and as well as to and from the alveoli.

RBCs are able to pick up  $\text{O}_2$  and drop off  $\text{CO}_2$  at the lungs and conversely drop  $\text{O}_2$  and pick up  $\text{CO}_2$  at the cellular level. They have a concave shape on both the front and back because they don't have a nucleus. This allows them to squeeze into hard to reach places and perform their functions[79].

Leukocytes, also known as white blood cells (WBC) are specialized for fighting infections and are able to identify foreign microorganisms that may cause harm to the body.

Thrombocytes or platelets are fragments of cells about 2  $\mu\text{m}$  in diameter in the shape of a flying saucer and are of great importance to our work, since they can be activated to change shape, grow dendrites and release coagulation factors that start a chain reaction that culminates in the formation of a clot[80] which would alter the normal functioning of our turbine and produce adverse systemic effects.

## 5.6 Density, Viscosity and Hematocrit

Density is defined as weight divided by volume. When considering fluids, both gases and liquids, density is simply the weight of the fluid in Kg per unit volume in liters or its equivalent cubic meters or cubic centimeters (cc). At standard temperature and pressure (STP), nitrogen is a gas and has a density of 1.2504 Kg/m<sup>3</sup>, while water at STP has a density of 1 g/cc or 1000 Kg/m<sup>3</sup>. Conversely, human blood at 37 °C, has an average density of 1060 Kg/m<sup>3</sup>.

The concept of viscosity is less straight forward than density, since there are different types of viscosity. Two important types of viscosity are: kinematic viscosity, which is defined as a fluid's natural resistance to flow when only gravity is acting on the fluid. The other type is dynamic viscosity ( $Vd$ ) which is related to kinematic viscosity ( $Vk$ ) by the density ( $\rho$ ) of the fluid.

$$Vd = Vk * \rho \text{ (Eq 5.1)}$$

Kinematic viscosity is measured in centistokes (cSt) while dynamic viscosity is measured in units of Pascal times seconds (Pa\*s) or in centipoise (cP), in honor of Jean Poiseuille who discovered the way incompressible fluids flow under laminar (non-turbulent) conditions. The law of Poiseuille states that the flow rate of an incompressible fluid in a cylindrical vessels such as a vein or artery is proportional to the pressure difference between the ends of the vessel multiplied by the fourth power of its radius, and that the flow rate is inversely proportional to the fluid's density  $\eta$  times the length of the vessel  $L$ . A constant of proportionality consisting of the fluid's density and the number  $\pi$  produce the following equation,

$$dV/dt = dP \pi r^4 / 8\eta L \text{ (Eq. 5.2).}$$

The normal range of viscosity in the human blood is between 3 and 4 cP, and is linked to the concept of hematocrit, which is simply the ratio of RBCs to the whole blood in the system.

The greater the amount of RBCs, the higher the density and the viscosity. This causes the blood to move more slowly due to a higher resistance to flow. This higher density may help our turbine because the blood would have more momentum, and the higher viscosity would generate a flow speed that produces a steady, lower RPM rate. This is beneficial only if the generator in the design presented in chapter 2 is able to produce high enough voltage levels at low RPMs rather than high current levels.

## **5.7 Platelet Activation**

Three different mechanisms by which platelets are activated will be considered in this section. One of them is well understood, which is due to injury or breaking in the continuity of a blood vessel. The other two, are due to changes in the flow of blood, such as abrupt acceleration or deceleration. These cause high shear stress of the endothelium (cells that form the inside walls of the blood vessels) and pooling or circular flow respectively and are not as well understood as the former[81].

It can be concluded that care must be taken not to disturb the natural flow of blood to prevent this platelet activation. One way to do this is by using biocompatible materials such as Ni-Ti alloy and also by designing a turbine that limits high shear rates and prevents pooling of the blood inside the blade assembly chamber. Another way to reduce the possibility of platelet activation is by reducing the operating volume in the blade assembly chamber as well as the contact time between the blood and the inside of the chamber. The reason for this is that under normal circumstances the endothelium secretes chemical compounds such as nitric oxide that inhibit the activation of platelets, and since the inside of the turbine would not have these cells, it is quite possible that a longer time in the chamber could trigger platelet activation[82].

## 5.8 Biomaterials and Hemocompatibility

A study of any implantable medical device would not be complete without an analysis of its compatibility with the human body, especially one that is designed to be in contact with the most intimate part of our anatomy, the circulatory system. Therefore it is important to discuss not only biocompatibility, but hemo-compatibility as well.

Biomaterials can be defined as simply as artificial or otherwise materials that can be used to augment, assist or even replace some biological system[83]. The same can be said for hemo-compatible materials with the added caveat that they must not react with or otherwise obstruct the normal functioning of the circulatory system, especially its most sensitive components, the blood cells. Therefore, hemolysis or the damage of RBCs, WBC's, platelets, etc must be avoided at all cost. The sensitivity of the platelets to high shear rates or low shear rates that cause blood recirculation and stagnation is also of grave concern. It is for these reasons that it is important to adhere to tried and true methods that have shown success in the use of devices with intimate implantation requirements, those in contact with blood as it courses through the network of vessels that make up the circulatory system.

Although there are several approaches to the problem of hemo-compatibility, such as the use of hemo-compatible materials like titanium (considered to be the most biocompatible material) and some alloys (Ni-Ti or Co-Cr used in cardiovascular stents)[83], no approach is 100% effective and the use of anticoagulants is still necessary whenever a blood-contacting IMD is implemented. Another approach is to use ceramics such as SiC in a process called plasma enhanced chemical vapor deposition (PECVD) at temperatures as low as 80 °C[84] in the form of coatings, a process for which the Silicon Carbide Group at USF has been recognized worldwide[85].

Other materials used in stents, such as hemo-compatible polymers may be used as an internal coating covering the inside of the casing and composing the blade assembly, they are not as durable as the hemo-compatible metals mentioned above, but they are certainly much cheaper.

In this work the proposed materials were not tested. Rather, this information is presented to help those continuing this line of research to select which is the best option to implement, out of those already established systems. In other words, the conclusions chapter will include some suggestions, since the applied materials research needed to implement the hemocompatibility requirement in the current work is beyond the scope of this dissertation.

## CHAPTER 6: TESTING METHODS

In order to complete the integration of the EMI generator with an IMD, the circuits and designs presented in the previous sections must now be implemented.

### 6.1 Structural Integrity

The fabrication of turbine that is to operate in a closed loop system must be approached by making sure that the material is strong enough to prevent fracturing of the turbine walls under the pressure of the fluid, that the 3D printer's minimum feature size is small enough to prevent leaking of fluid through the walls and that biocompatible and non-thrombogenic materials be identified. Additionally, the circuit of Figure 4.6 may be manufactured on printed circuit board and assembled into the casing of the generator along with the turbine, which is to be coupled to the single or dual generator of Figure 5.3.

### 6.2 Testing Methodology

The testing of the proposed energy harvesting system will be completed in the following manner:

1. No more than 3 turbine models are to be tested in-vitro.
2. Each. model consists of a turbine rotor with notched blades which are to be mounted onto the rotor of the generator and enclosed by the casing. The blades, casing and connectors will be designed by use of a computer assisted design (CAD) software and 3D printed using a system and material compatible with biomedical research[64].

3. Preliminary testing of the system will be completed using nitrogen gas and mass flow controller and pressure gauges to determine the pressure difference and flow necessary to rotate the blades and harvest the energy needed to power most implantable medical devices.
4. Secondary testing will consist of creating an closed-loop system where water is circulated through the turbine. The energy harvested will be documented at different RPMs as well as the differential pressure (pressure drop) and flow across the system.
5. Final testing will be conducted in the same manner as in step 4 above, replacing water with a blood simulant that carries the same properties of density and viscosity as blood.

This testing phase will show the actual performance of the assembled device in order to determine whether any changes or adjustments are necessary and to see new potential applications and the possibilities of future works.

### **6.3 Data Collection Approach**

In order to measure the raw energy harvested by the system, a variable impedance load will be connected to the output of the generator and the voltage and current measured. The speed of the rotor will be assessed by the frequency of the generated sinusoidal wave as explained in section 2.1 above. This will produce a set of AC power curves that elucidate the actual capabilities of the proposed system as well as the system's ability to power an actual IMD, but first the AC sinusoidal wave must be rectified using a simple, low-drop Schottky diode and smoothing capacitor. The rectified wave will produce a DC level capable of driving the TI-BQ25504 DC to DC converter or other voltage booster.

The output of the booster can then be connected to a variable DC load to measure the voltage, current and power necessary to maintain proper operation of a typical IMD.

The following chapters present the execution, results and analysis of the proposed work to include the fabrication of a large scale turbine (LST) as described and tested by [28],[63] and its miniaturized version or miniature scale turbine (MST), as well as two iterations that optimize the miniaturized version for implantation or Optimized Turbine for Implantation (OTI).



## CHAPTER 7: DESIGN, FABRICATION AND ASSEMBLY

### 7.1 Introduction

The design and fabrication of the proposed implantable miniaturized turbine followed a very methodical and empirical approach to ensure that any needed changes were implemented on the fly instead of arriving at final conclusions and then implementing changes, and to prevent, as much as possible, relegating those changes to future works.

The aforementioned method followed the following steps.

1. Miniaturization and testing of the MST that could be iterated and adjusted in accordance with findings and goals.
2. Fabrication and testing of LST implementing changes born out of the preliminary findings in step 1 and to have a point of departure for further miniaturization. This also allowed the author to consider other potential applications of a larger system.
3. Fabrication and testing of two additional turbines (OTI-1 and OTI-2) that followed recommended changes for optimization of the MST needed to meet the implantation power density goals of being small enough for implantation yet harvest enough energy to power most IMDs currently available.

### 7.2 Model Design

Using the work proposed by [28] as a point of departure, a notched-turbine model at 3.175X scale was chosen as a point of departure to achieve the miniaturization and optimization proposed in this work. Figure 7.1 below shows the original blade assembly, rotor and casing.

Section 7.2.1 will address the size difference between the original model and the MST.

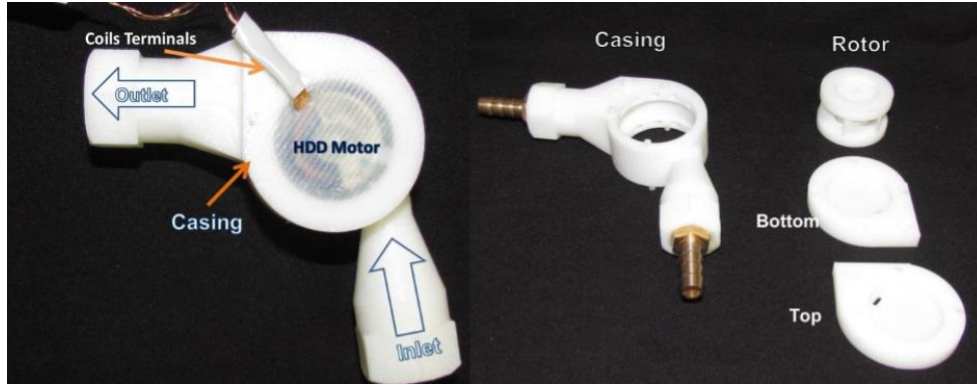


Figure 7.1 Notched-Turbine model, scale 3.175X, 2.5 inch HDD motor [28]

### 7.2.1 MST Model Design

Using the design specifications provided as a guideline, a 3D model for the MST was drawn for simulation and fabrication.

Table 7.1 shows a comparison between the size of the original turbine in Figure 7.1 and that of the MST proposed in this work. Notice that although most dimensions are reduced only by a factor of 3, the total casing volume, which is very important for implantability, was reduced by a factor of 44; while the operating volume, which represents the amount of fluid that is necessary to fill the chamber and keep the turbine in operation, was reduced by a factor of 25.

The fact that the generator's volume was only reduced by a factor of 4.51 is actually a positive and encouraging development, since the power density remains higher than if the volume followed a trend as that of the casing and rotor's chamber. Simply stated, the casing's reduction is approximately 10 times that of the generator's, resulting in a power density increase.

The results shown on Figure 7.2 seek to demonstrate the proper flow of the fluid as the rotor rotates while submerged in the fluid. Notice that the high speed (colored red) spots behind some of the blades represent points of high shear forces acting on the blades.

In the physical implementation, this is not necessarily the case because the fluid is actually driving the rotor, instead of the rotor driving the blade assembly.

Table 7.1 Size comparison between original 3.175X turbine model with generator from [28] and the new miniaturized turbine (MST) with generator proposed in this work.

Salient Feature	3.175X Original Model	MST	Reduction Ratio
Blade Assembly Diameter (mm)	34.00	10.60	3.21
Blade Assembly Height (mm)	21.00	7.10	2.96
Nozzle Diameter (mm)	3.50	1.20	2.92
Inlet Diameter (with connector) (mm)	15.40	4.50	3.42
Outlet Diameter (with connector) (mm)	15.40	4.50	3.42
Casing Diameter (mm)	48.50	14.50	3.34
Casing Height (with lids) (mm)	35.50	9.00	3.94
Casing Volume (mL)	65.58	1.49	44.13
Inlet Angle of Incidence (deg)	100.00	100.00	N/A
Outlet Angle of Departure (deg)	0.00	0.00	N/A
Rotor Chamber Diameter (mm)	35.00	11.50	3.04
Rotor Chamber Height (mm)	23.00	8.40	2.74
Rotor Chamber Volume (mL)	22.13	0.87	25.36
Operating Volume (mL)	25.00	1.00	25.00
Generator Height (mm)	8.30	3.80	2.18
Generator Diameter (mm)	27.00	18.80	1.44
Generator Volume (mL)	4.75	1.05	4.51

Also notice the dark blue region to the left of the outlet along the negative x-axis. This suggests the possibility of pooling in this area, so a further reduction in the diameter of the outlet would be beneficial, since it is highly desirable to prevent the pooling of blood in an implantable system.

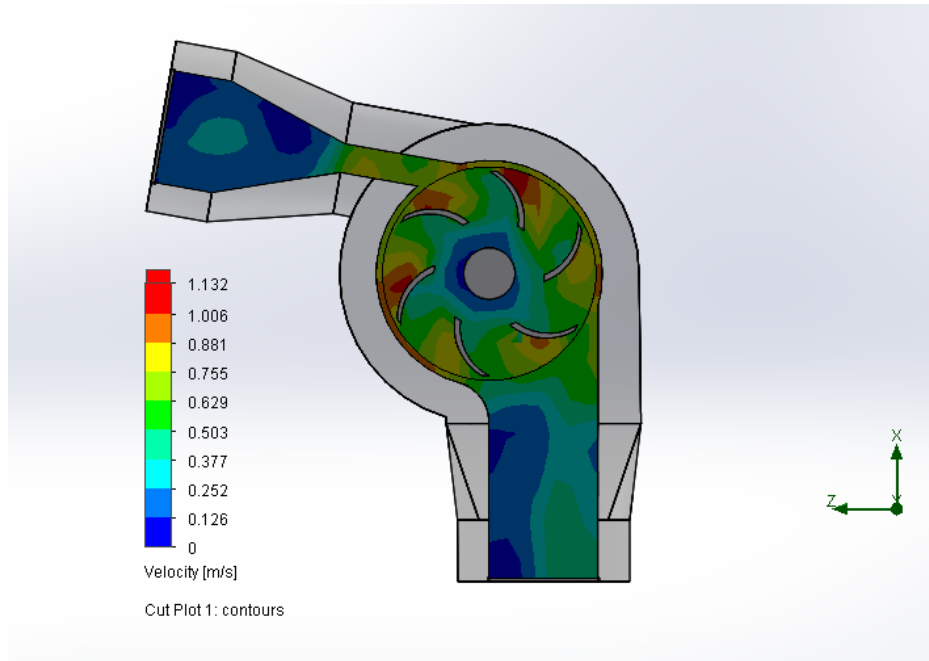


Figure 7.2 Flow velocity profile of MST fluid in a rotating mesh.

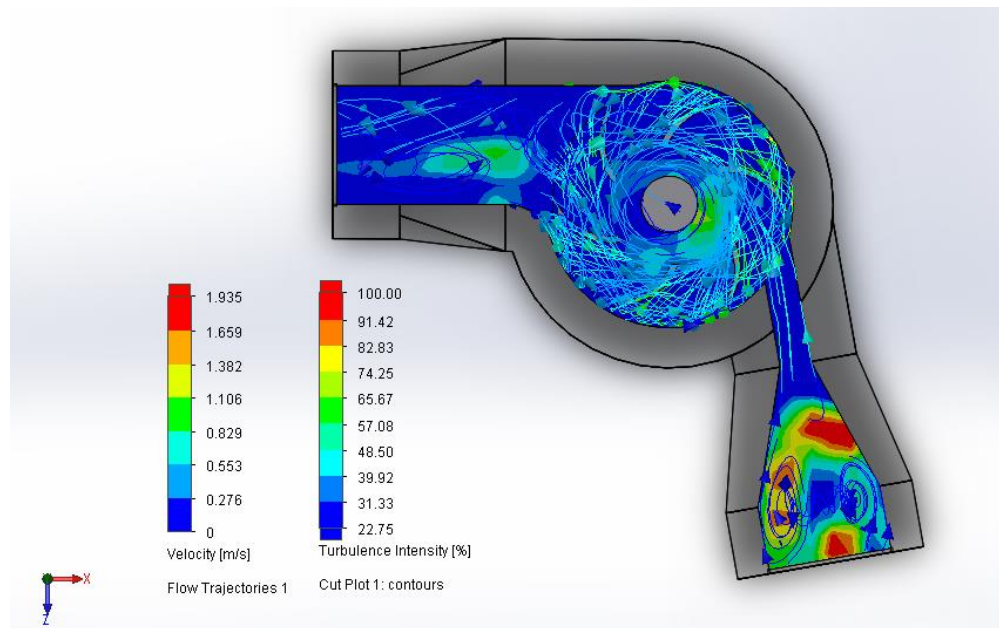


Figure 7.3 Top view of flowlines with arrow heads representing the direction of flow and background contour colors representing the presence or absence of turbulent behavior.

Figure 7.3 shows the flow trajectory represented by flow lines with arrow heads, indicating the proper direction of flow. This flow drives the rotor in the CCW direction producing an electromagnetic field that generates a current when a load is connected to the output of the generator that is connected to the rotor. The fluid is then seen exiting the chamber at the outlet. The contour colors in the background show a laminar flow inside the rotor chamber and at the outlet and nozzle. The inlet chamber on the other hand shows a bit of turbulent behavior that can be ameliorated by reducing the size of the inlet and increasing the size of the nozzle. This would decrease the nozzle velocity slightly, but it would be a good compromise between performance and optimal flow conditions.

The next subsection introduces the LST model in which the difference in inlet and outlet diameter has been decreased, and the shape of the blades has been adjusted to improve flow conditions.

### **7.2.2 LST Model Design**

The changes proposed in this section include, a widening of the blades on the blade assembly to reduce the action of shear forces behind the blades, seen highlighted in the bottom left corner of Figure 7.4. The front angle of the blades remains the same and so does the angle of incidence on the blade as the fluid leaves the nozzle and impacts the front of the blade. The inlet nozzle diameter was increased and the inlet diameter reduced to facilitate passage of the fluid without stagnation. Finally, the outlet was slightly decreased to match the reduced height of the new model. All dimensions appear on Table 7.2. The changes proposed were implemented on a large model (LST) and a new miniaturized model optimized for implantation (OTI-1) which is presented in section 7.2.3 below. This allowed the author to derive a new reduction ratio table for a comparison similar to that of Table 7.1.

Figure 7.4 shows the CAD drawing of the new LST, to include the casing and a lid that is secured to the casing at six points around the assembly. This turbine is then miniaturized and analyzed to establish a new low profile system.

The inlet and outlet connectors are not displayed, but are attached after fabrication. The entire process is discussed in section 7.3, Model Fabrication. Table 7.2 shows the size comparison and reduction ratios between the LST and the OTI-1.

### 7.2.3 OTI-1 Model Design

In this section, the new optimized LST model is miniaturized to create the OTI-1, resulting in improved flow (when compared to the MST), higher aspect ratio (width: height) and rounded corners, all very important features for IMDs.

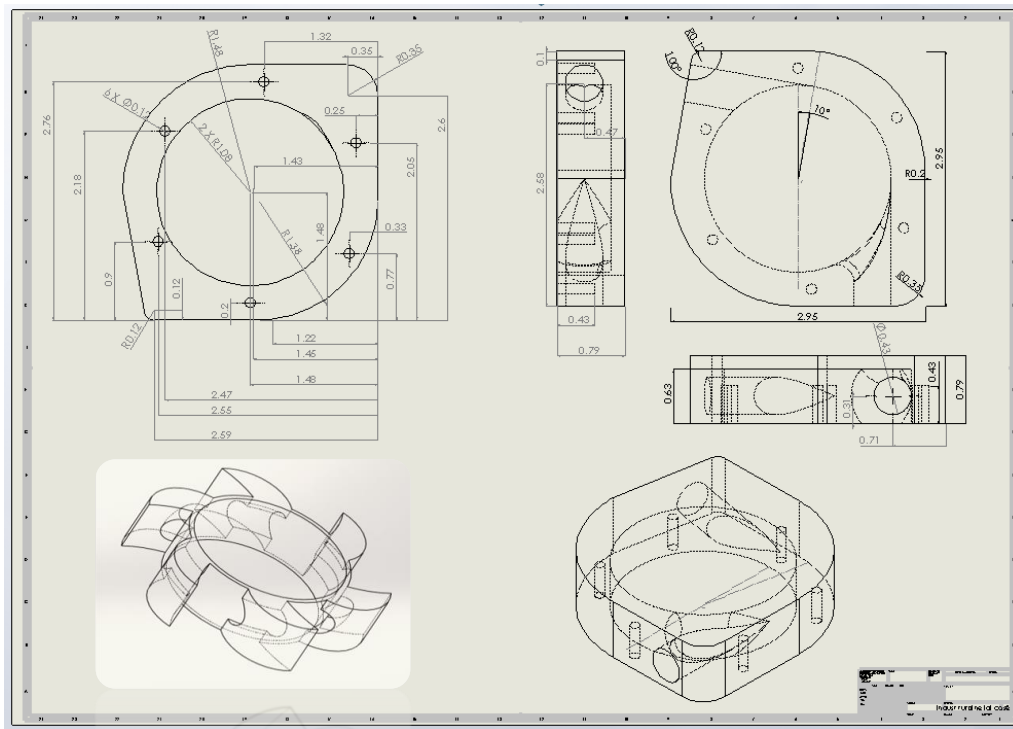


Figure 7.4 LST design implementing changes stemming from first miniaturization effort findings. All dimensions are in inches and angles in degrees. Starting at the top left corner, the lid, blade assembly and casing are shown in a CCW direction around the page.

Figure 7.4 presents the CAD drawing of the LST and Table 7.2 shows some important results that give the OTI-1 its name. Even though our first miniaturization effort achieved a remarkable reduction ratio of 44, the MST's aspect ratio and overall volume could be reduced further to facilitate implantation. It is important to notice that most organs and structures in the human body have a high aspect ratio, a rule that designers follow to ensure good conformity. Table 7.3 shows a comparison of the aspect ratio improvement. It is worth mentioning that in the human body, the aspect ratio to consider is called length: depth instead of length: height.

Table 7.2 Size comparison between the large scale turbine (LST) with generator and the optimized turbine for implantation 1 (OTI-1) with generator.

Salient Feature	LST	OTI-1	Reduction Ratio
Blade Assembly Diameter (mm)	51.15	27.15	1.88
Blade Assembly Height(mm)	13.00	3.40	3.82
Nozzle Diameter (mm)	5.00	3.20	1.56
Inlet Diameter (w/connector)(mm)	6.00	4.00	1.50
Outlet Diameter (w/connector)(mm)	6.00	4.00	1.50
Casing Diameter(mm)	74.75	35.30	2.12
Casing Height (with lids)(mm)	27	8	3.38
Casing Volume (mL)	118.49	7.83	15.13
Inlet Angle of Incidence (deg)	100.00	100.00	N/A
Outlet Angle of Departure (deg)	0.00	0.00	N/A
Rotor Chamber Diameter(mm)	54.30	28.46	1.91
Rotor Chamber Height(mm)	15.96	5.42	2.94
Rotor Chamber Volume (mL)	36.96	3.45	10.72
Operating Volume (mL)	16.00	1.50	10.67
Generator Height(mm)	12.20	6.20	1.97
Generator Diameter(mm)	25.50	19.80	1.29
Generator Volume (mL)	6.23	1.91	3.26

The spleen and kidneys have an aspect ratio of approximately 3[86], a worthy goal to achieve, but most importantly size reduction to prevent any disruption in the normal functioning of body organs in the thoracic cavity, where the device would likely be implanted.

The LST has a similar aspect ratio, but it is too large for implantation, on the other hand, OTI-1 has an aspect ratio of 4.41, which suggests that further reduction in volume would also reduce the aspect ratio if the height remains the same, making it more suitable for use in the thoracic cavity. This is why a second optimized turbine was introduced and is presented in section 7.2.4 below, the OTI-2.

Table 7.3 Improved aspect ratio (length: height) with optimization and miniaturization.

Model	Aspect Ratio
3.175x	1.37
MST	1.61
LST	2.77
OTI-1	4.41
OTI-2	3.13

#### 7.2.4 OTI-2 Model Design

The miniaturization and optimization process that culminated with the OTI-2, offers a reduction factor of 2.4 in the casing volume (3.25 mL), which reduces the displacement of local organs, preventing increases in intrathoracic pressure when implanted. This miniaturization also reduces the operating volume by a factor of 3 (0.5 mL) which demands less blood from the circulatory system to remain in operation.

Table 7.4 compares the two turbines showing the highest reduction ratios highlighted in red. Table 7.3 above also makes a final comparison of aspect ratios of all turbines considered in this work, where the OTI-2 seems to have an aspect ratio (3.13) closest to the aspect ratio of the spleen and kidneys (3) found in the left upper quadrant of the abdominal space and the retroperitoneal space, respectively. In the next section the fabrication of these models is



considered and their features are compared as this work comes closer to the goals established in the beginning chapters.

Table 7.4 Size comparison between the OTI-1 turbine with generator and the OTI-2 turbine with generator.

Salient Feature	OTI-1	OTI-2	Reduction Ratio
Blade Assembly Diameter(mm)	27.15	15.00	1.81
Blade Assembly Height(mm)	3.40	3.00	1.13
Nozzle Diameter (mm)	3.20	3.00	1.07
Inlet Diameter (w/connector) (mm)	4.00	3.50	1.14
Outlet Diameter (w/connector)(mm)	4.00	3.50	1.14
Casing Diameter(mm)	35.30	23.50	1.50
Casing Height (with lids)(mm)	8	7.5	1.07
Casing Volume (mL)	7.83	3.25	<b>2.41</b>
Inlet Angle of Incidence (deg)	100.00	100.00	N/A
Outlet Angle of Departure (deg)	0.00	0.00	N/A
Rotor Chamber Diameter(mm)	28.46	16.40	1.74
Rotor Chamber Height(mm)	5.42	3.40	1.59
Rotor Chamber Volume (mL)	3.45	0.72	<b>4.80</b>
Operating Volume (mL)	1.50	0.50	<b>3.00</b>
Generator Height(mm)	6.20	3.80	1.63
Generator Diameter(mm)	19.80	18.80	1.05
Generator Volume (mL)	1.91	1.05	1.81

### 7.3 Model Fabrication

Once the 3D CAD design was completed in SolidWorks, it was printed using a Zortrax M200 3D printer. The Zortrax M200 was selected for its quality and affordability, ease of use and history of good performance in the prototyping of biomedical devices in dentistry, medical

education and research [88]. The artificial heart depicted on Figure 7.3 below is an example of a research device printed with the M200 shown on the right.



Figure 7.5 Artificial heart on the left and the Zortrax M200 3-D printer used to create it[87].

### 7.3.1 Zortrax M200 3D Printer

The Zortrax M200 is a remarkable 3D printer that uses proprietary software called Z-suite, a simple and easy-to-use rendition software that converts Stereolithography (STL) files generated in any CAD software, to a Z-code file that the printer can understand.

Every model printed consists of 3 parts: The raft, which is a platform that securely attaches to the heated plate and supports every layer of the model. The model itself is the second part of the print and the third is the supports used to ensure accurate model replication especially for angled parts that hang from the main structure. The build volume is 200x200x180 cubic mm and the parts are built on a heated, perforated, metal plate. The layer height can be selected from 90 to 400 micrometers. At 90 micrometers (less than the diameter of human hair), the details achieved are very resolved and approximate the quality of that of an injection-molded part.

Support structures are optional, which allowed sparked the idea to design the parts and print them in an orientation that did not require the use of support structures.

Not using supports served two purposes: First the part comes out cleaner and smoother as any remnants of support material are simply non-existing.

Second, the turbine and its connectors were printed at the same time using an overlap technique where multiple parts can be printed as one solid part, without needing to remove any support material, especially from the inside of the cylindrically-shaped connectors. The nozzle of the printer can heat up to 375 °C which allows for the raft that supports the model to melt into the perforations on the build plate, preventing any shifting in the model while it is printing. The models discussed in the previous section, were all printed using the Zortrax 3D printer.

Additionally, each model was printed in Z-ABS, a proprietary filament especially design for this printer. But different brands of filaments can be used by adjusting the nozzle temperature according to the manufacturer's instructions.

The models were also fabricated in PMMA (Acrylic) using the more traditional CNC machining process, which afforded a stronger, more durable and leak proof material during the liquid testing process. A layout of each part as presented on Figure 7.4 above was submitted to the Engineering Technical Support Services (TSS) machine shop, College of Engineering, University of South Florida (USF) for fabrication. They were also able to create threads for the barbed connectors that joined the turbine's casing to the flow tubing in the closed-loop test bed used to characterize each turbine.

Figure 7.6 shows a completely printed turbine lid and blade assembly. The half-finished casing shows the typical honeycomb fill structure inside the walls. Changing the fill percent setting changes the density of the part as well as its rigidity and durability. The narrowing part of the inlet at the bottom of the image forms the nozzle.

The amount of filling material is adjustable, as a percentage, but the higher the percentage, the longer it takes to print.

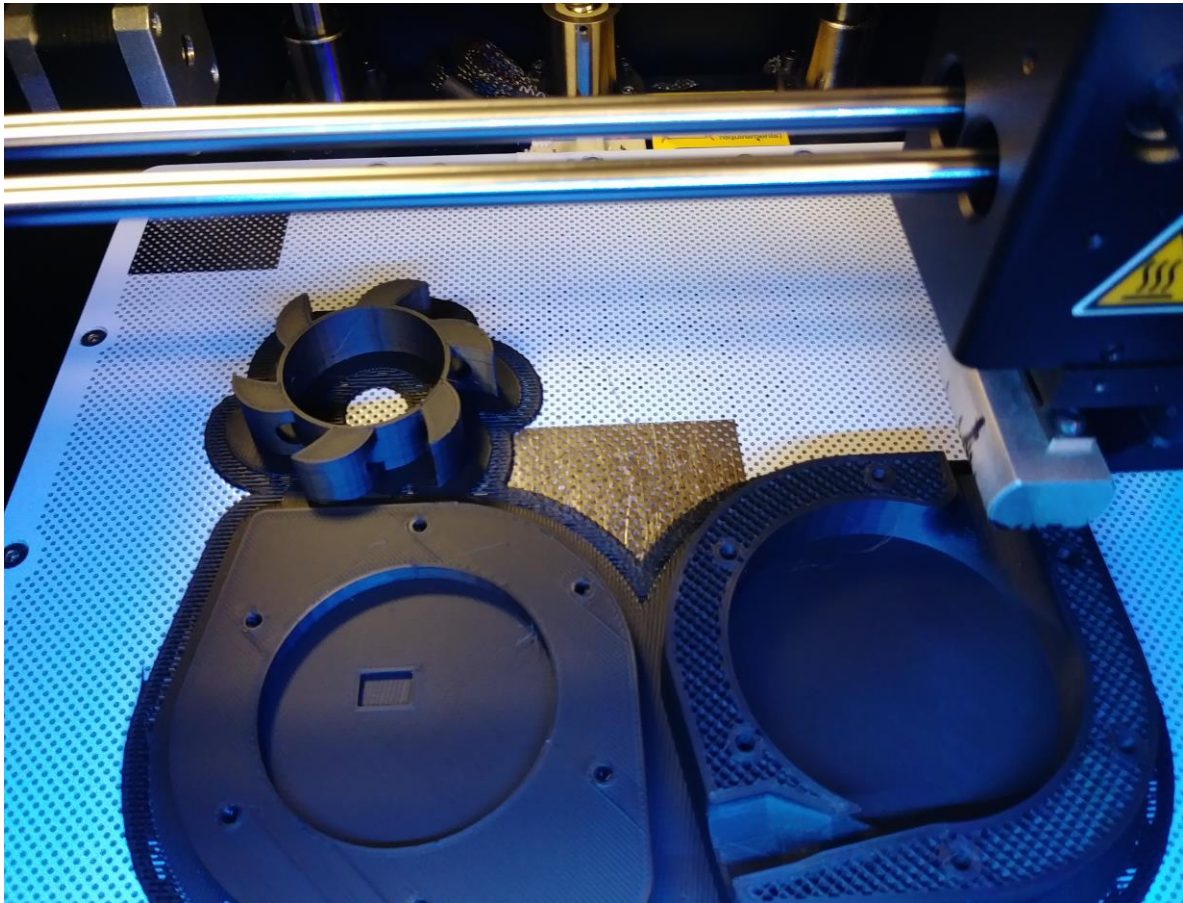


Figure 7.6 Zortrax printer in action, printing the LST blade assembly (top), lid (lower left) and casing (lower right).

Usually it is advised that the fill be adjusted down to minimize the probability of a failure during the print, but in particular, the M200 is highly reliable compared to other printers regardless of how long the job takes to complete. In the author's experience, setting the printer to work over night and returning to a finished product was commonplace and very convenient. The detachment of the model from the heated plate that is common with many 3D printers in the market is simply non-existent with the M200 because the perforated plate technology it employs, allows the initial raft to stay securely in place during the completion of the entire process.

### 7.3.2 MST Model Fabrication

The MST was the first turbine fabricated and tested, following the design specification of Cabra in [28]. Notice in Figure 7.7 that the inlet and outlet are attached to 3D-printed barbed connectors that accept the flow circuit's tubing. This turbine resulted from the reduction of the NTEG by a factor of 44 (see section 7.2), but it presented additional challenges that led to the changes seen in the LST and subsequent turbines. The red and black wires allow for connection to the load for AC testing or to the rectifier for DC testing.



Figure 7.7 Miniaturized-scale turbine (MST) 3D printed in ABS and assembled for testing in a transparent holder.

The changes suggested by the analysis in section 7.2 led to the design and manufacturing of the LST to establish a basis for comparison before the next miniaturization attempt was completed. Those changes resulted in a reduction in height that produced low-profile turbines (OTI-1 and OTI-2), as needed for implantation purposes.

### 7.3.3 LST Model Fabrication

The LST model was fabricated, then tested and characterized only with a nitrogen delivery system that controlled the flow and measured the differential pressure between the inlet and outlet. This process is described in its entirety in chapter 8. For now, Figure 7.5 displays the 3D printed model in ABS with a 200 micron resolution and no supports. It consists of 3 parts: 1) The chamber that comprises the nozzle, the inlet and the outlet; 2) the lid, which holds the generator; and finally 3) the blade assembly whose blades are impacted by the fluid and transmits its rotational energy to the generator's rotor.

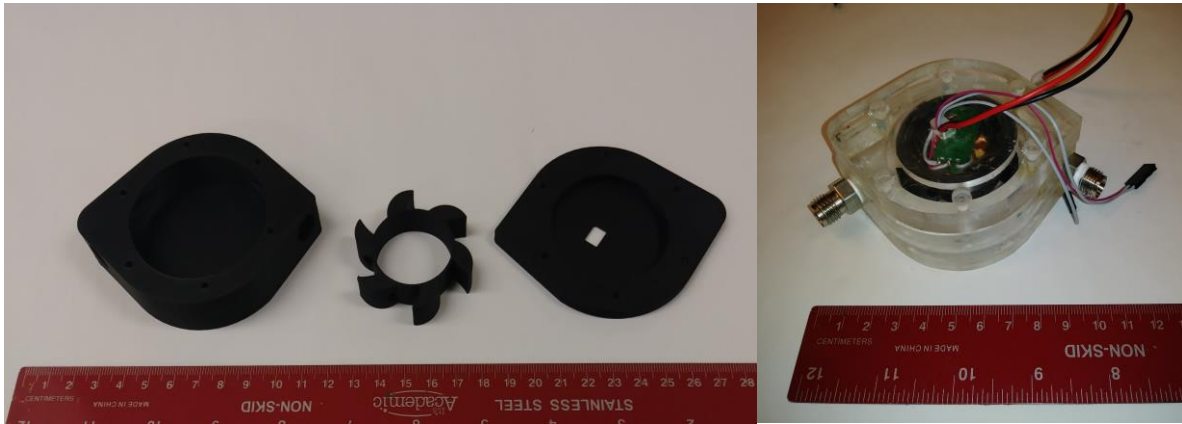


Figure 7.8 LST casing rotor and lid 3D printed in ABS on the left and CNC-machined LST assembled for testing on the right.

The CNC-machined LST seen on the right side of Figure 7.8 was fabricated in PMMA and consists of 3 main parts just like its 3D printed counterpart, but only the casing and lid were CNC machined. The blade assembly was 3D printed. This allowed the author to clearly see the rotation quality of the rotor during testing, as the PMMA is transparent and the blade assembly is opaque. The perforation in the middle of lid allows for the connection wires to be accessed and connected to the load.

### 7.3.4 OTI-1 Model Fabrication

The OTI-1 is the first step in miniaturization and optimization for implantation, and it is based on the low-profile shape of the LST. Figure 7.9 shows the OTI-1 both 3D-printed in ABS (bottom left) and machined in PMMA. The top left and top right images depict completely assembled devices ready to be tested with nitrogen gas and water.



Figure 7.9 Optimized turbine for implantation (OTI-1) 3D-printed in ABS and machined in PMMA with different barbed connectors and blade-assembly-loaded generator.

The center of Figure 7.6 displays the motor used as a generator for OTI-1, notice that the blades fit tightly around the circumference of the rotor while the stator sits below the blades and is held in place by the casing. The bottom center shows a casing without barbed connectors. A single connector is shown at the 7-cm ruler mark. These connectors can be 3D printed as part of the casing, as seen at the bottom left of the figure. The brass version can be seen at the top left, which can be used with certain applications.

### 7.3.5 OTI-2 Model Fabrication

The last turbine considered is the OTI-2, which takes the OTI-1 as a starting point. Its fabrication was also done in ABS through 3D printing and machined in PMMA. It is smaller in diameter and height than the OTI-1, as is described in Table 7.4.

Figure 7.10 shows the parts of the unassembled OTI-2. Notice that the notched-blade assembly was 3D printed in ABS, while the casing was machined in PMMA. Once the blade assembly is mounted on the generator (bottom right), they are sealed onto the casing. The rotation of the blade assembly can be clearly seen on the underside of the casing as it turns.

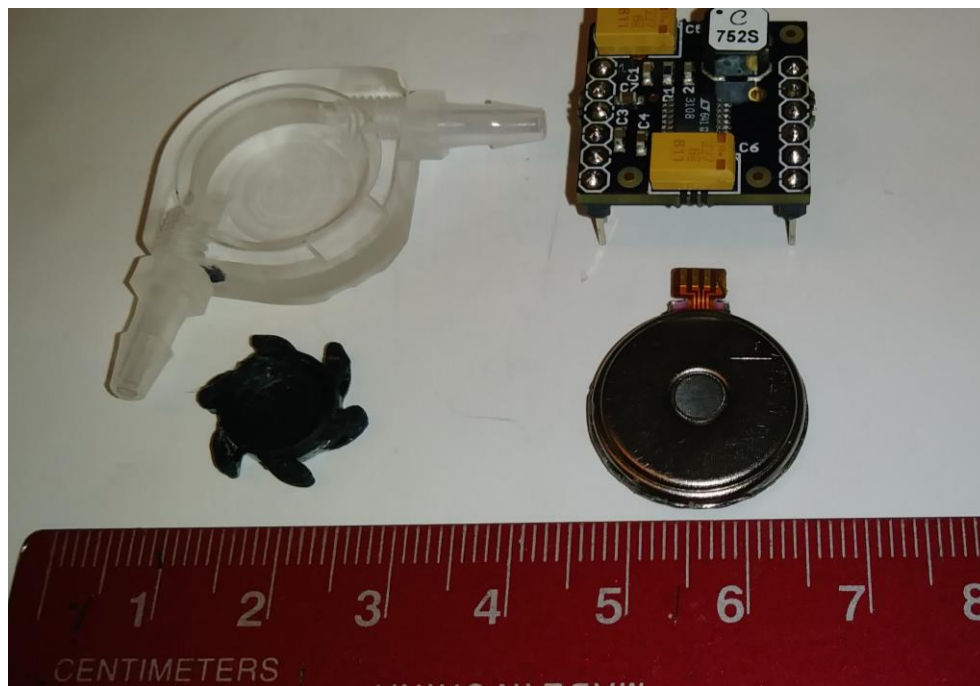


Figure 7.10 OTI-2 parts: Blade assembly (bottom left), generator (bottom right) and PMMA casing with barbed connectors, along with LTC 3108 femto (top right)

The circuit seen here in the top right corner of the image is a DC to DC converter that will be explained in later chapters. The machining of this turbine tested the limits of the machining capabilities at USF.



New desk-top CNC machines will soon be available in the market and our research group too will be able to machine even smaller parts needed to continue this work in the future. Finally, this turbine was tested in nitrogen gas, in water and in simulated blood using flow especially designed flow circuits and test beds.

## CHAPTER 8: SYSTEM TESTING

Once the turbines were fabricated and assembled with their respective generators, they could be considered as energy harvesting systems capable of producing treated power that could be verified and calculated from measured values by connecting the system to a variable load and finding the voltage across the load and the current through the load. The product of these two numbers gives us a measure of the power produced or generated by each turbine. This power will depend on mainly on two factors: The rotational speed of the turbine in RPM and the load connected to the generator's output. Even though these turbines use a 3 phase generator, only two internally connected phases were connected to the load for AC voltage and current measurements and to a single Schottky diode rectifier coupled to a DC to DC converter for DC-load measurements. These measurements were obtained by varying the load at different flow and pressure difference conditions.

### 8.1 Testing Circuits

The circuit shown in Figure 8.1 depicts the voltage harvested from the flow as AC voltage source  $V_{Iac}$ . This voltage is either connected directly to variable load L1 or to a rectifying circuit composed of a Schottky diode and a 470  $\mu$ F capacitor as is shown in Figure 8.2. These circuits were assembled by soldering all components onto a perforated prototyping board and fitting them with pin connectors. This strategy allowed led to making them modular for interconnection between the energy-harvesting turbine system for AC measurements using the circuit of Figure 8.1 or DC measurements using the circuit of Figure 8.2.

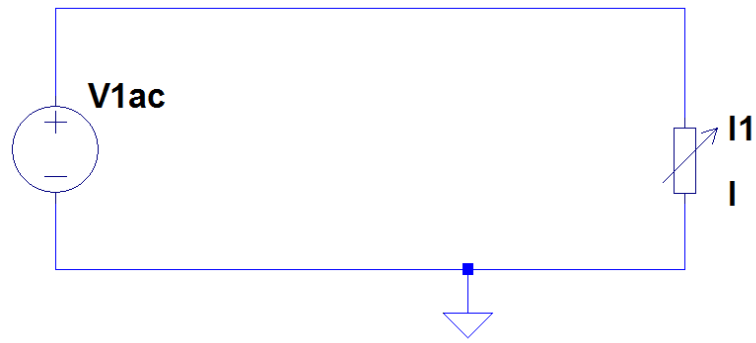


Figure 8.1 Voltage source representing the sinusoidal output from the turbine system's generator, connected to a variable load L1, used for AC testing.

### 8.1.1 Rectifier

The rectifier circuit was also assembled separately on a perforated board and outfitted with pin connectors that couple to the generator. Notice that this is a Schottky low-drop diode with internal resistance that increases with increases in current flow, therefore producing a higher voltage drop when the turbine is operating at higher RPM.

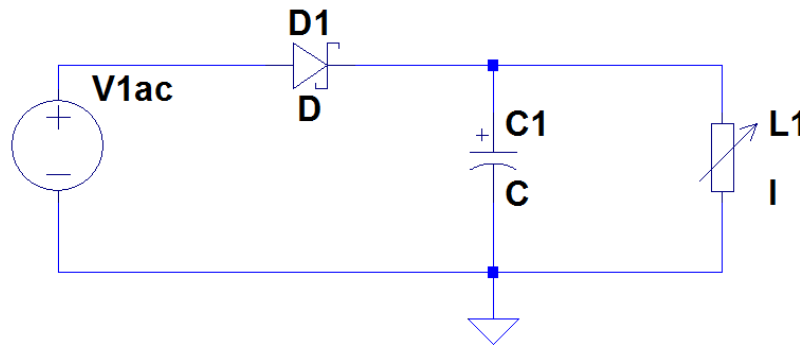


Figure 8.2 Turbine system generator (V1ac) connected to rectifying circuit (D1, C1) and to variable load L1 for DC testing.

Figure 8.3 shows the Schottky diode I-V curves that determine how much useful voltage is left after rectification. This rectification is necessary to change the raw power produced by the generator into useful power that can be used by an IMD.

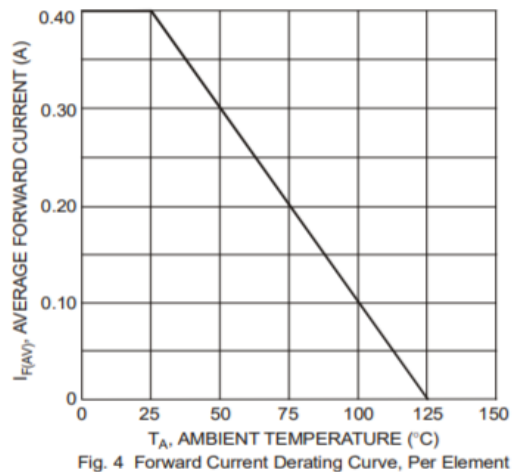
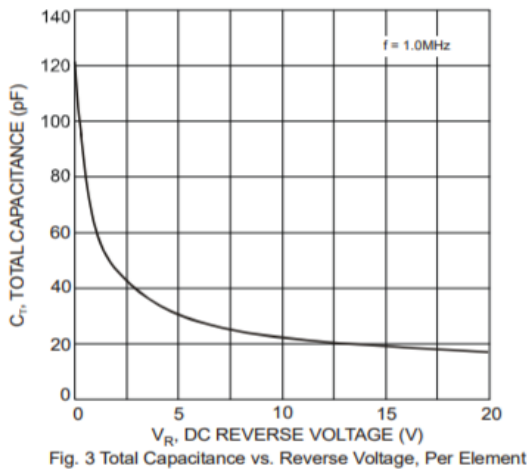
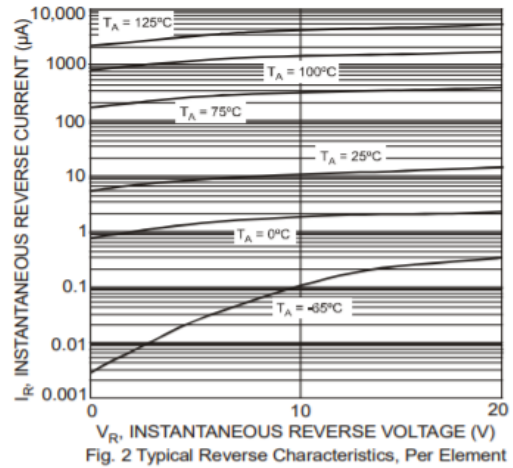
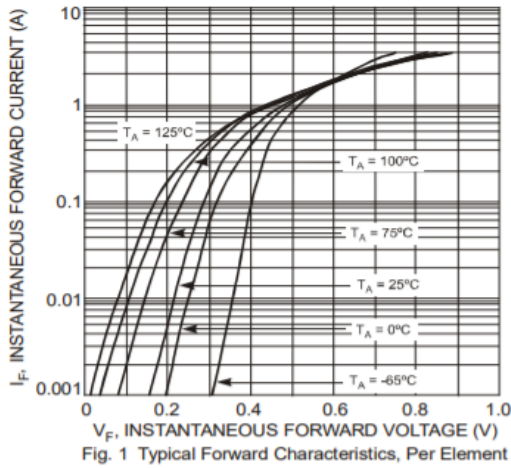


Figure 8.3 Schottky rectifier, CW from top left: Typical forward current, typical reverse current, total capacitance and forward current derating current characteristic curves[104].

### 8.1.2 Variable Load

Figure 8.4 shows the rectifier circuit connected to the variable load, which is composed of two variable high precision potentiometers (1 KΩ to the left and 10 KΩ the right of the first proto board) that can be selected individually by choosing the position of the jumper seen above the second potentiometer. The board seen on the right shows 5 potentiometer connected in series configuration to allow for the measurement of very small currents that are typical with pacemakers and other low power IMDs.

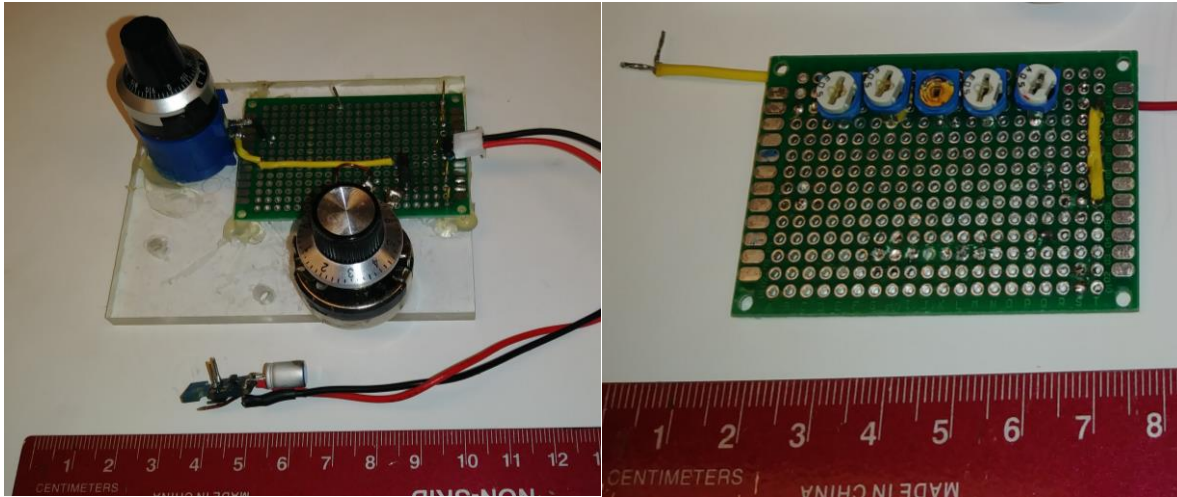


Figure 8.4 Variable load configuration for testing AC and DC output with and without rectifier (bottom left) and high impedance measurement load on the right.

The energy harvested from each flow tested (nitrogen, water and simulated blood) is of a sinusoidal form and needs to be rectified before it can be used by a device. The rectifier seen in Figure 8.4 is a single diode rectifier and a capacitor. This single diode approach makes it simple to construct, test and diagnose any issues during testing. Also a single diode (as opposed to a full bridge) reduces the loss incurred before the DC level it produces can be fed to the DC to DC converter depicted in the diagram of Figure 8.8. Figure 8.5 shows the four DC to DC converters used in this work.

1. TI BQ25504 in the bottom right corner of the figure. This board is made by Texas Instruments and delivers 3.3 volts DC from a minimum input of 0.3 volts DC and a input impedance of 3 K $\Omega$ .
2. LTC 3105 in the bottom left corner of the picture. This converter is made by LTI semiconductors and is able to produce a variety of voltage levels available at two outputs, the low drop output (LDO) at 1.5, 2.2 and 3 volts DC, and the standard

output (SO) at 1.8, 3.3 and 5 volts DC from a minimum input of 0.25 volts DC, with a maximum power of 80 mW, and input impedance of 13 K $\Omega$ .

3. LTC 3108 Supercapacitor is seen at the top right of the figure. This board is made by LTI semiconductors and it is configurable to 2.3, 3.3, 4.1 or 5.0 volts available at two outputs (Vout and Vout2) from a minimum input of 0.2 volts. Its input impedance was found to be 8  $\Omega$  and a bank of four 1F, 2.7-volt supercapacitors.
4. LTC 3108 femto, top left corner of the figure, is the smallest of the four and it produces an output of 2.2 volts DC from minimum input of 0.2 volts and input impedance of 12.4  $\Omega$ .

Each of these boards was used to boost the DC voltage produced by the rectifier and maintain a regulated output that can be used by an IMD. Once the DC to DC converter is integrated with the turbine, the assembly becomes an energy harvesting system that takes energy from flow and converts it to raw electrical energy that is rectified and then boosted and regulated by the DC to DC converter.

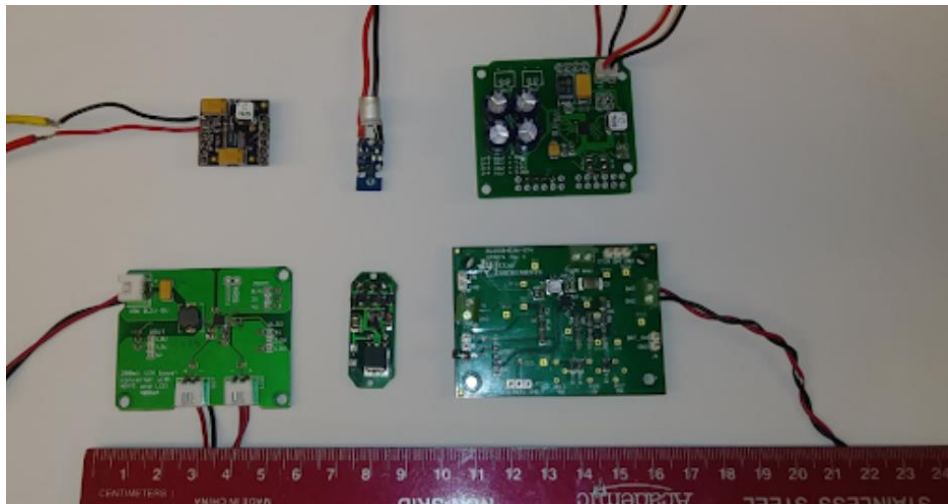


Figure 8.5 Rectifiers and DC to DC converters used to convert harvested energy to DC and boost it to an appropriate level for IMD's. CW from the top-left, LTC 3108 femto, Schottky diode rectifier, LTC 3108 Supercap, TI Bq25504, 3 Phase rectifier and LTC 3105 DC booster.

The originally proposed work included the simulation and use of only one DC to DC converter, the BQ25504, but as the work continued, it was obvious that as the density of the fluids used increased, the efficiency decreased and did not allow for increases in power. Therefore other DC to DC converters with lower cold-start voltage (LTC 3105 and LTC 3108) were tested to mitigate the losses and stay within the parameters of what is physiologically possible in the circulatory system.

The LTC 3105 allowed the author to evaluate different input levels that correspond to the use of the turbines in IoT applications, while the LTC 3108 supercapacitor (LTC 3108S) was needed to analyze the SIPS ability to operate as a power source for an implantable defibrillator (ID), where the number of shocks delivered for defibrillation requires a lot more energy than that of the pacemaker.

The analysis of how well the LTC 3108S is able to source an ID is relegated to future works, but it is introduced here as a tool of future investigation. Similarly, the LTC3108 femto (LTC 3108F) board is to introduce to give future investigators an idea to miniaturize the board into a size small enough to fit in the walls of the turbine casing.

Using one single DC to DC converter and designing a circuit to for use with a single IMD would restrict this work to a single application problem and a particular solution. Rather, it is more interesting to explore several approaches and use four different DC to DC converters as tools of investigation, rather than as a single one that answers one particular set of questions.

## **8.2 Nitrogen Gas Flow Energy Harvesting**

In this section, energy is harvested from a flowing gas in particular, nitrogen as it flows from a pressurized tank through a regulator and mass flow controller (Figure 8.6).

The gas flow circuit is an easy-setup and a preliminary test that simplified the troubleshooting process on the way to achieving the goal of producing a turbine capable of harvesting energy from blood flow. Additionally, it provided a platform to explore and compare the turbine's behavior under different flow conditions and consider other potential extracorporeal applications.

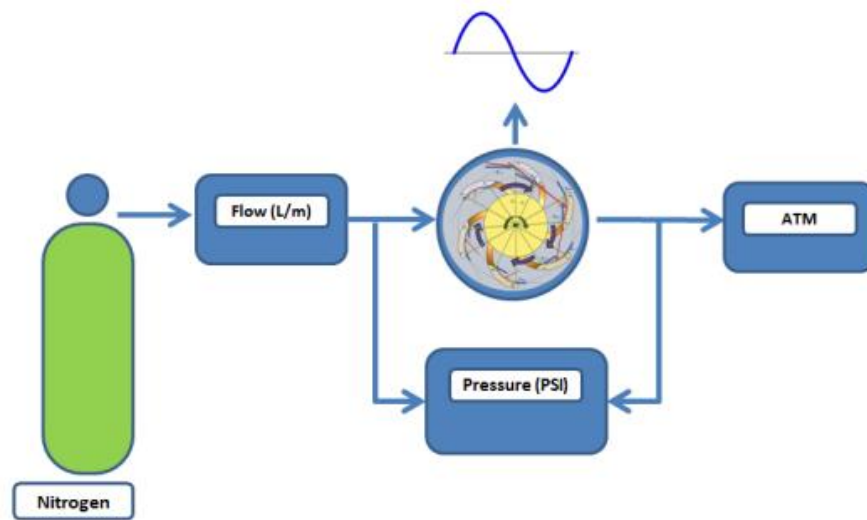


Figure 8.6 Setup of nitrogen flow through the turbine system for energy harvesting.

### 8.2.1 Equipment

The following equipment was used to complete the nitrogen flow harvesting test on each of the four turbine systems (LST, MST, OTI-1 and OTI-2)

1. 2500 PSI NI300 compressed nitrogen tank as the gas source.
2. Dual pressure regulator with gauge to step down the pressure to 0-60 PSI.
3. UFC 3020 mass flow controller from UNIT Systems, Inc.
4. Unit Systems URS-100 mass flow controller power supply and display/control unit.
5. GFC 1143 Dwyer mass flow controller.



6. Tektronix TDS 3052 oscilloscope to measure the RMS voltage and frequency from the turbine's generator output.
7. Phillips PM2534 system multimeter used to measure the current through the load.
8. Hewlett Packard 34401A multimeter for measuring the voltage across the load.

### 8.2.2 Setup

The output from the turbine in Figure 8.6 was coupled to the input indicated by the short arrow in Figure 8.7 below. This configuration allowed for the measurements to be recorded in video format by focusing the camera on the various displays, providing a big picture permanent record of how the different meters adjusted to changes in the load, being careful to turn the potentiometer slowly enough for the instruments to acquire and display the measured values, thus ensuring greater accuracy.

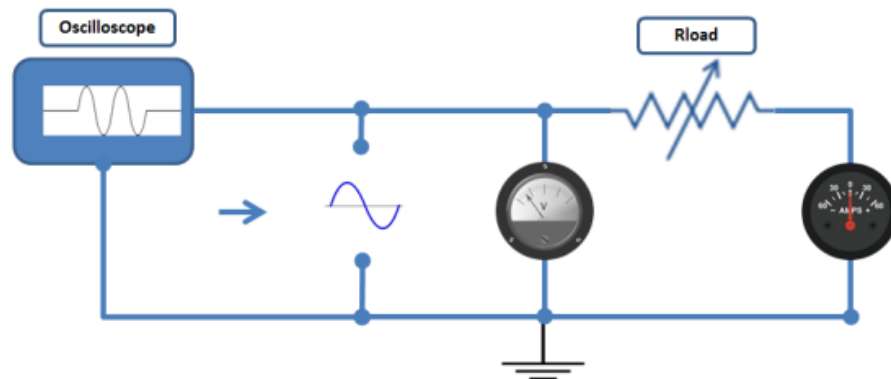


Figure 8.7 Circuit diagram for measuring AC voltage and current at the load.

As the gas flowed from the tank, depicted in Figure 8.6, the turbine rotated at an RPM commensurate with the flow, generating a sinusoidal voltage wave measured by the circuit in Figure 8.7. The flow output from the turbine was allowed to vent into the atmosphere (ATM) and the differential pressure gauge measured the difference in pressure between the input and the output. The resulting power curves obtained are presented in chapter 9

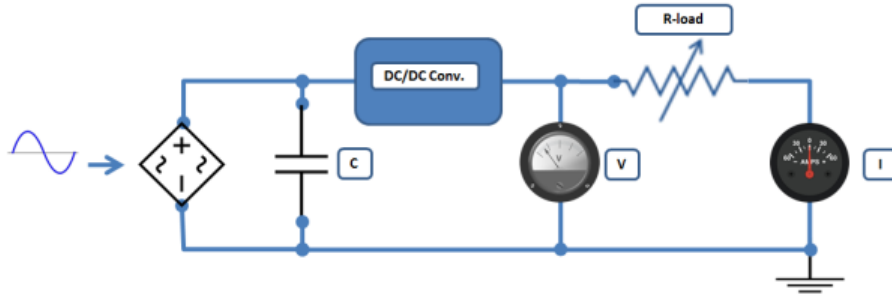


Figure 8.8 Circuit used for DC voltage and current measurements.

Again, the voltage output from the turbine system is used as a voltage input to this circuit and is indicated by a short arrow that goes into the rectifying circuit (Figure 8.8). Notice that the output from the regulator now becomes the input to the DC to DC converter that boosts the voltage from tenths of volts to 2.2 or 3.3 volts depending on the converter used. The load was then connected to the output of this DC to DC converter and the DC voltage and current are measured across and through said load.

Figure 8.9 shows the actual physical set up used in the AMBIR lab. The instruments seen here are described in the previous section. This setup was used for DC voltage and current measurements. The same instruments were used for AC measurements, with minor changes that are described by the circuits of Figures 8.6 and 8.7. In other words the rectifying circuit and the DC-DC converter were not used and the meters were set to measure AC voltage and current RMS values.

The use of the UFC 3020 mass flow controller enhanced the testing process by allowing for the testing of the turbines under lower flow rates when compare to the GFC 1143 controller. This controller was simpler to setup though, since it has a built in display unit while the UFC 3020 had to be connected to a separate display on the URS 100 power supply.

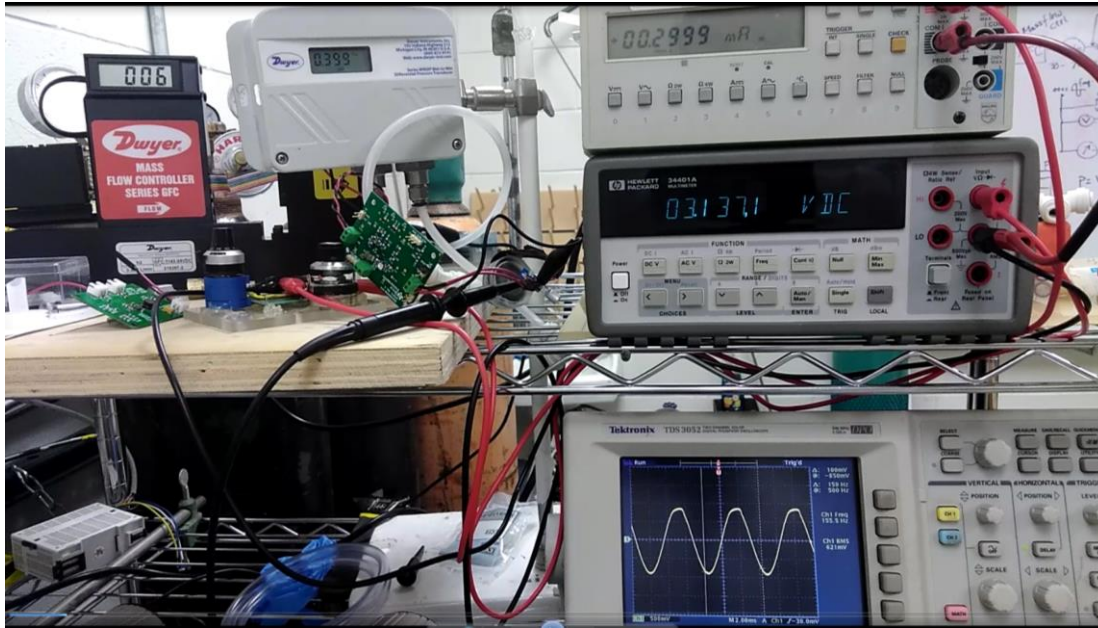


Figure 8.9 Actual lab setup described by the circuits of Figures 8.5 and 8.6

Once the setup was completed, the pressure difference across the turbine,  $P_d$  was adjusted incrementally and the load changed gradually. At each incremental point, the following measurements were taken:

1. AC Measurements: Generator voltage and frequency in Hz,  $V_g$  and  $f_g$  from which the RPM was calculated; the current through the load from which the power to the load was calculated; and finally, the differential pressure,  $P_d$  between the inlet and outlet, and the voltage produced by the flowmeter,  $V_f$  from which the efficiency and flow were calculated.
2. DC Measurements: Generator ac voltage and frequency,  $V_g$  and  $f_g$ , from which the flow power and RPM were calculated, the DC voltage across the load  $V_L$ , as delivered by the rectifier and the current through the load  $I_L$ , from which the power delivered to the load was calculated; and finally, the pressure difference across the turbine and flowmeter voltage from which the flow was calculated.

### 8.3 Water Flow Energy Harvesting

After testing each turbine using the nitrogen flow circuit, a new closed-loop circuit was devised using a small water pump that moved the water from a reservoir through the turbine and through an ultrasonic flowmeter, allowing the water to flow unrestricted back into the reservoir.

#### 8.3.1 Equipment

The following equipment was used to complete the water flow harvesting test on three turbines systems, the MST, OTI-1 and OTI-2.

1. Sealed water reservoir.
2. One Cynergy3 Ultrasonic flowmeter.
3. One ZKSJ DC30A-1230 Brushless DC pump.
4. Two 0-5 PSI, DPG-101, calibrated Dwyer pressure gauges.
5. Tektronix TDS 3052 oscilloscope to measure the RMS voltage and frequency from the turbine.
6. Phillips PM2534 system multimeter to measure the output of the flowmeter.
7. Hewlett Packard 34401A multimeter for measuring voltage across the load.
8. Extech Instruments TrueMultimeter 430 to measure the current through the load.

The ultrasonic flowmeter used is preferable to a rotational flowmeter, because it does not obstruct or slow down the flow; it simply senses the signal from each of two ultrasonic generators and calculates the difference in arrival times by making use of the Doppler effect principle[89]. See Figure 8.10 for a visual representation of this process.

Figure 8.11 shows the closed-loop circuit implemented to test three of the turbines' ability to harvest energy from water flow. The MST, OTI-1 and OTI-2 were evaluated.

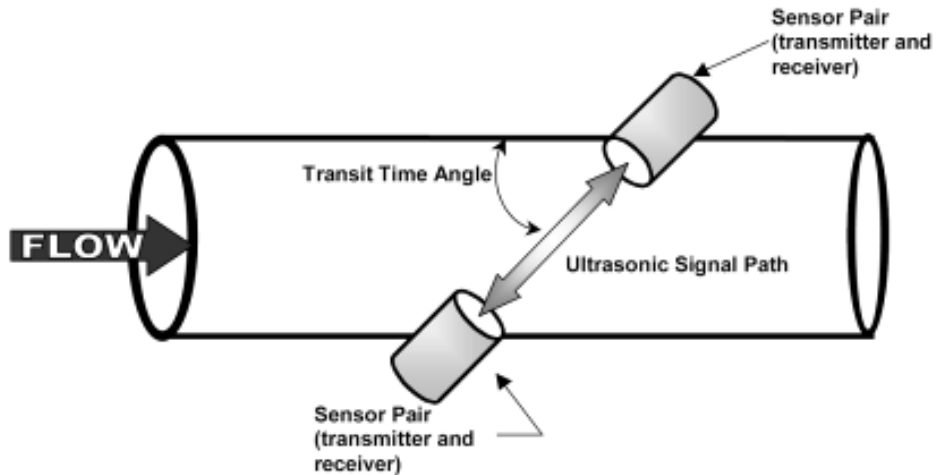


Figure 8.10 Principle of operation of ultrasonic flowmeter used in this work[89].

### 8.3.2 Setup

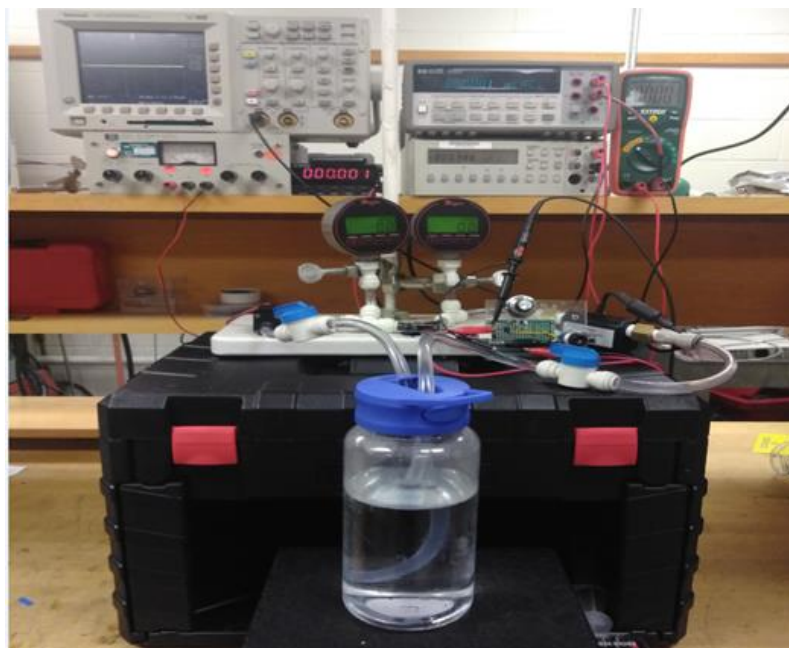


Figure 8.11 Closed-loop circuit setup used to evaluate the MST, OTI-1 and OTI-2 turbines' ability to harvest energy from water flow.

A small DC brushless 2 LPM pump (Figure 8.12) was used to pump water from a 1-liter reservoir through a valve into the turbine, causing the turbine's blade assembly to rotate and the generator's rotor along with it.



Figure 8.12 Water pump, tubing, push –fit connectors and valves used on closed-loop circuit

The flow continued through the flow meter, past a secondary valve and finally back into the reservoir, completing the circuit in a continuous uninterrupted loop. The pressure transducers are connected as close to the inlet and outlet of the turbine by T-push-fit connectors. The reduction adapter seen in the middle on Figure 8.12 connects 3/8” to 1/4” tubing to secure a proper connection to the OTI-1 and OTI-2 low profile turbines.

The clear tubing and PMMA casings helped to ensure no air was trapped in the tubing that may affect the pressure readings especially. Additionally, the blade assembly could be seen as it started and stopped rotating during the test.

The DC pump was controlled by a variable voltage source that facilitated the indirect control over the speed of rotation of the turbine by changing the flow through it when the voltage to the pump was adjusted up or down. Once again, the output from the turbine was connected directly to the load for AC measurements (Figure 8.7) or to the rectifier circuit and DC-DC controller the same way it was done in section 8.2 and established by the circuit of Figure 8.8.

Once the setup was completed, the water pump was set to full half and one fourth power and during each setting, the variable load was changed in small increments.

At each incremental point, the following measurements were taken:

1. AC Measurements: Generator voltage and frequency in Hz,  $V_g$  and  $f_g$  from which the RPM was calculated; the current through the load from which the power to the load was calculated; and finally, the differential pressure,  $P_d$  between the inlet and outlet, and the voltage produced by the flowmeter,  $V_f$  from which the efficiency and flow were calculated, respectively.
2. DC Measurements: Generator ac voltage and frequency,  $V_g$  and  $f_g$ , from which the flow power and RPM were calculated, the DC voltage across the load  $V_L$ , as delivered by the rectifier and the current through the load  $I_L$ , from which the power delivered to the load was calculated; and finally, the pressure difference across the turbine and flowmeter voltage from which the flow was calculated.

#### **8.4 Simulated Blood Flow Energy Harvesting**

In this section an in-vitro test of the OTI-2 turbine system was conducted in order to estimate the power harvested from blood flow in the circulatory system of a higher mammal by using a specially formulated fluid that displays some of the same characteristics as human blood, in particular, its consistency; more specifically, its density and viscosity. The fluid was circulated using the closed-loop system described in section 8.3 by use of a small variable pump.

##### **8.4.1 Equipment**

In addition to the equipment described in section 8.3, three more important pieces of equipment were used to prepare and characterize the simulated blood (SB) solution, namely, a U.S. Solid microscale, a Genie 2 Fisher Vortex mixer and a Smart-Series Fungilab rotational viscometer. Figure 8.13 shows this equipment as described from left to right.

The section on setup below describes the SB preparation in detail and the characterization necessary to match the viscosity of human blood.



Figure 8.13 Left to right: Microscale, vortex mixer and viscometer with attachments.

#### 8.4.2 Setup

In order to more accurately approximate the flow of blood in the human body some changes were made to the fluid (water) used in section 8.3. Using the conclusions in [105] a 600 mL solution was prepared, consisting of 38.15% Glycerol, 49.07% water and 12.78% Sodium Iodide (NaI) powder by weight.

The mixture was shaken vigorously in a 1 liter sealed flask and agitated for 15 minutes using the Ginie 2 vortex mixer. 10.6 mL of the solution was poured into the Fungilab sample container seen in Figure 8.13. The system was set to measure viscosity of the fluid using spindle TR9, seen on the far right in Figure 8.13. The spindle was placed inside the filled sample container and then set to rotate at 100, 60, 50 and 30 RPM. The test was conducted at standard temperature and pressure (STP) with a lid and the results were entered into Table 8.1 below.



The values of viscosity obtained were found to be within normal values found in human blood, as reported by [90], as a Mean  $\pm$  Standard Deviation of  $4.4 \pm 0.6$  (cP) and by [91] as 5.83 cP. The shear rate as seen in Figure 8.14 is the gradient of the velocity as the layers of fluid in motion move closer to a static or stationary structure. In the case of a blood vessel, the center of the vessel is where the blood moves the fastest, decreasing as the rings of fluid (assuming laminar flow) get closer to the endothelium. The endothelial cells are deformed under high shear, and this deformation is called shear stress, which is the force per unit area that is needed to ensure gradient behavior depicted in the figure.

Table 8.1 Measured values of shear rate, shear stress and viscosity for varying RPM

RPM	Shear Rate( /s)	Shear Stress (Pa)	Viscosity (Cp)
<b>100</b>	34	1.6	4.2
<b>60</b>	20.4	0.9	4.5
<b>50</b>	17	0.8	5.2
<b>30</b>	10	0.6	5.5

The equipment setup and measurements taken during the simulated blood harvesting process were identical to those presented previously and used for the water flow harvesting.

The aorta, which is the largest vessel in the human body has a diameter of  $31.1 \text{ mm} \pm 3.9 \text{ mm}$  (females) and  $33.6 \text{ mm} \pm 4.1 \text{ mm}$  (males)[92] and is where the highest blood speeds are seen, between 430 cm/s to 720 cm/s, increasing with age[93].

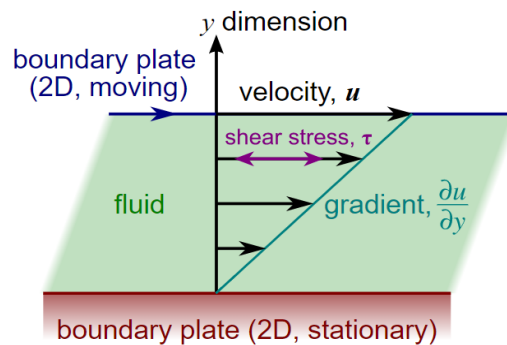


Figure 8.14 Shear of fluid between a moving and stationary plate under laminar flow conditions.

## CHAPTER 9: TESTING RESULTS AND DISCUSSION

For each setup, gas, water and simulated blood, both AC and DC measurements were taken and annotated in an Excel spreadsheet, from which the voltage and current were used to calculate the power. The rotation of the turbine at each frequency setting was calculated using Eq. 3.1. The resulting plots are presented in the following subsections and discussed in chapters 9 and 10.

### 9.1 Nitrogen Flow Harvesting Results

Nitrogen gas was chosen to conduct the turbine testing because it is a safe, inexpensive and very commonly used gas in industry and in academia with a myriad of applications. Additionally, it allowed for the use of already available setup in the AMBIR lab.

#### 9.1.1 AC Power and Efficiency

Testing results for all four turbines are presented in the order of implementation that led to the modifications necessary to optimize for implantation, starting with the miniaturize scale turbine (MST)

Figure 9.1 shows the assembled MST on the left and its components (casing, blade assembly and generator) on the left. AC power curves generated using nitrogen gas as an energy harvesting source can be seen in Figure 9.2 on a logarithmic scale. The efficiency was calculated by dividing the electrical power generated by the turbine by the inherent power from the flow of nitrogen through the nozzle, which can be expressed as,

$$P_{flow} = \rho Q v_{nozzle}^2 / 2 \quad (\text{Eq. 9.1})$$

In Eq. 9.1,  $\rho$  is the density of the fluid in  $\text{Kg/m}^3$ ,  $Q$  is the flow in  $\text{m}^3/\text{s}$ ,  $v\text{-noz}$  is the velocity at the nozzle in  $\text{m/s}$ . Additionally, given that velocity is related to distance and time in seconds by  $v\text{-noz} = d/t$  and volumetric flow can be expressed as  $Q = V/t$ , then using simple substitution,  $v\text{-noz} = Q/A$  or  $Q/\pi*r^2$ , where  $V$  is volume in the nozzle and  $A$  is the cross-sectional area of the nozzle. It then follows that since the flow comes out of the nozzle at a 10 degree angle with the horizontal axis,

$$v\text{-noz} = Q \cos(10^\circ) / \pi r^2 \text{ (Eq. 9.2)}$$

By substituting Eq.9.2 into Eq. 9.1 and programming the resulting equation into a spreadsheet, the power from a specific flow rate is found and since the electrical power has already been calculated from the product of the current and voltage, an efficiency calculation can be derived for every curve seen in Figure 9.2 at the peak and as an average of the useful part of the curve, between the peak and the tail end where the power drops out to very low levels.



Figure 9.1 Assembled MST on the left and its components on the right.

The average peak efficiency (PE) for the MST using nitrogen was found to be 13.1 %, while the average center-of-curve efficiency (CCE) found was 10.3 %. Notice that this efficiency is lower than that found by [28], but this is to be expected since the efficiency

decreases with increasing miniaturization due to increase of internal friction at the turbine's bearings. Notice that since the generator is actually a motor extracted from a 1-inch hard drive, designed to rotate at high RPMs, the power increases with increasing RPM, but this increase is mainly due to high current (Figure 9.3). This tells us that even though there is an increase in power, a low output voltage from the generator may limit the performance of the system due to rectification losses.

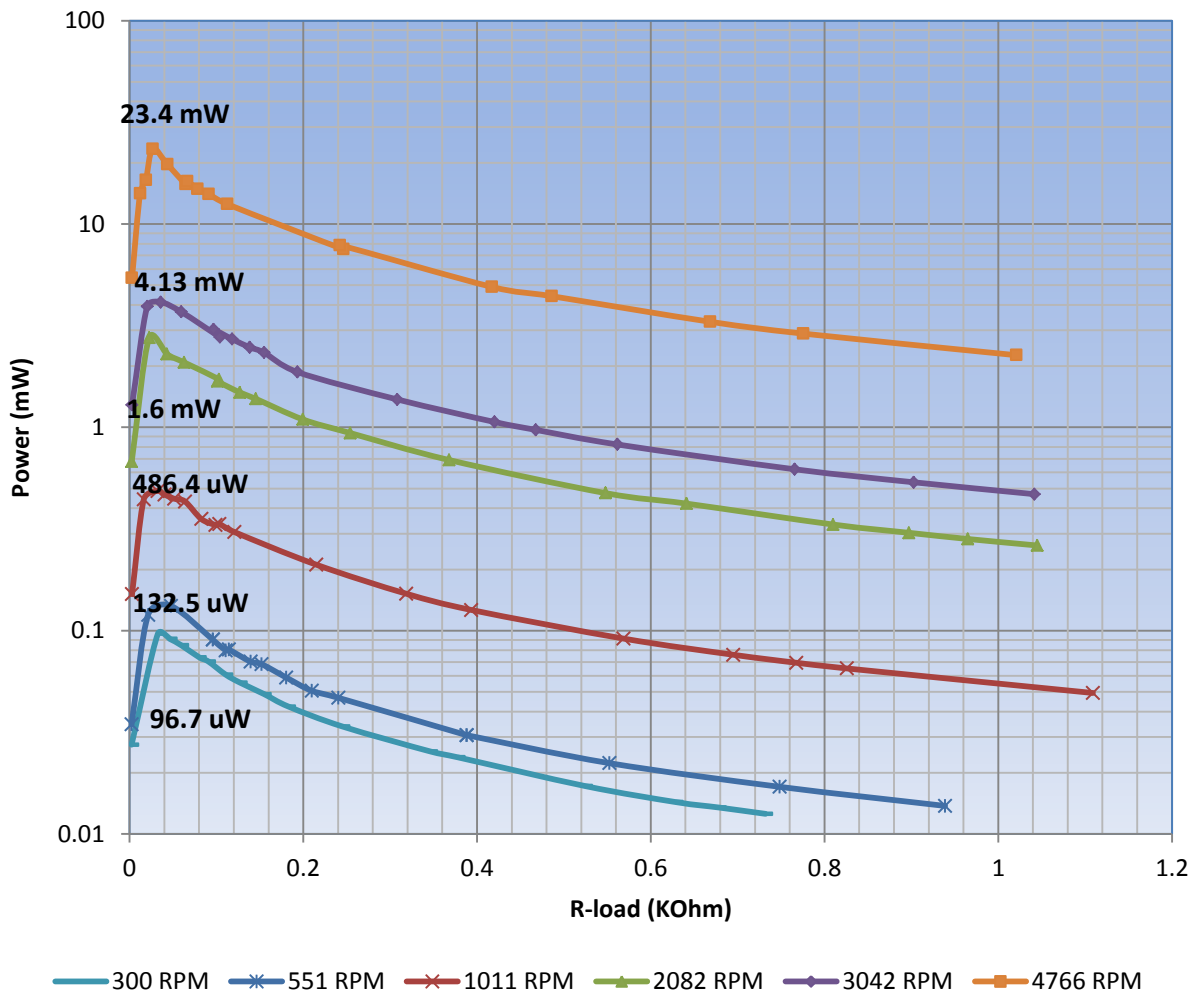


Figure 9.2 MST (N) AC power in mW vs load resistance in KΩ at increasing RPM

In other words, there will be high losses when the generator's voltage is rectified because increases in RPM produce high currents and low voltages (Figure 9.3) and the rectifier diode's internal resistance increases for higher currents (Figure 8.3).

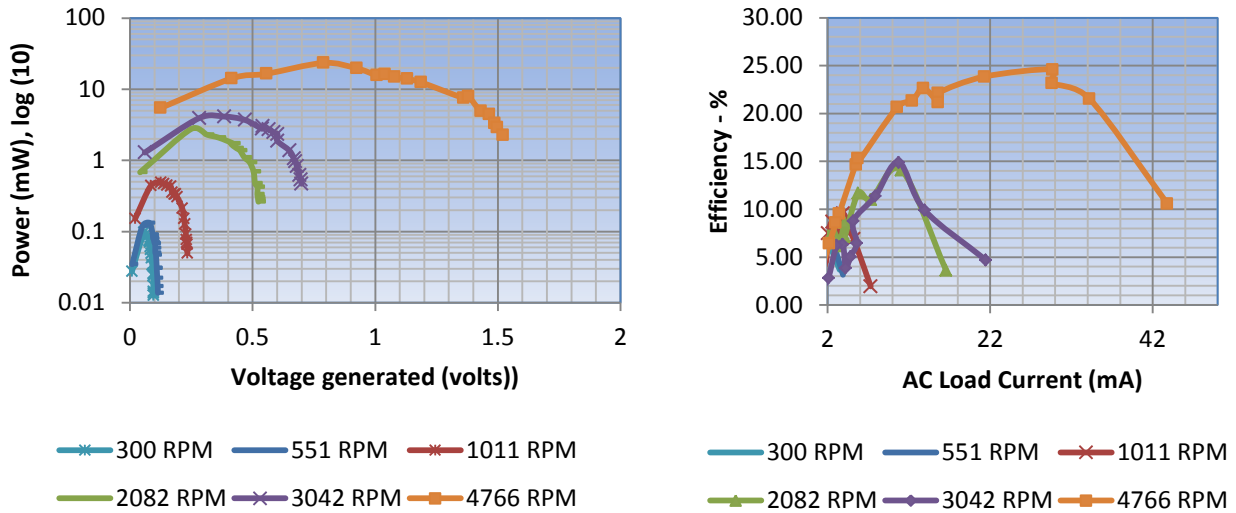


Figure 9.3 MST(N) AC power in mW vs generated voltage in volts at increasing RPM (left) and efficiency curves vs load current in mA (right)

Therefore, the author investigated the possibility of replacing this generator with a more appropriate high-torque, lower-speed one, that generates higher voltage with modest increases in RPM. Notice that this turbine can produce very high currents over 42 mA and is most efficient (25%) at high RPMs (Figure 9.3 - right).

Although the MST is small enough to be implanted, from the results seen in Figures 7.2 (high shear rate behind the blades) and 7.3 (fluid stagnation at the inlet) it was decided to decrease the turbine's height (as explained in section 7.2.3), adjust the inlet to this new height and increase the nozzle diameter to have a more balanced transition from the inlet to the nozzle to prevent stagnation of the fluid.

Since these changes would significantly alter the original design ratios (inlet to nozzle ratio increases, the blades become wider and width to height ratio increases) the recommended changes had to be implemented first at a large scale. So the large scale turbine was designed in Solidworks and 3D printed, then tested with a high torque generator able to produce a high voltage output, enough to mitigate the losses incurred by rectification.

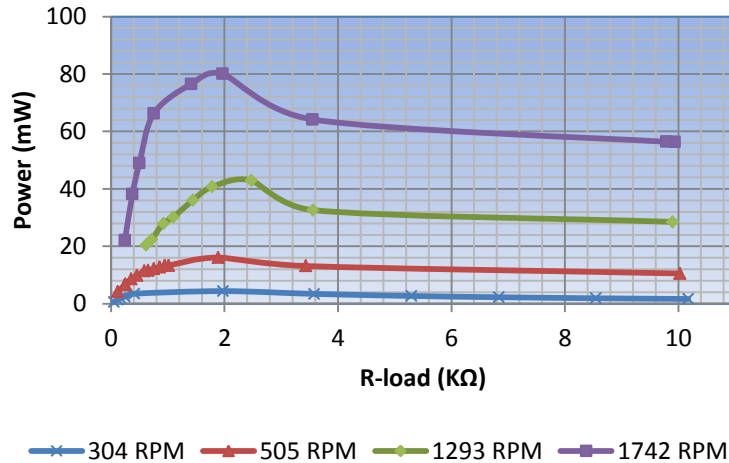


Figure 9.4 LST (N) AC power in mW vs load resistance in KΩ at increasing RPM.

The LST was tested with nitrogen gas and the power curves are seen in Figure 9.4, which provide a new starting point for miniaturization, but this time the changes made would produce miniaturized turbines optimized for implantation.

As expected, Figure 9.5 shows the efficiency curves (right) for the LST with peak efficiency over 50% at 1742 average RPM, which agrees with the findings by [28].

Furthermore, the power vs voltage curves are on the left, and it is clear that the voltage is high compare to the current in each of the power curves. A similar high  $V_{out}$  generator was needed for the MST, so negotiations were initiated with a European company to design a miniaturized generator for the next generation of optimized turbines, but due to budget limitations and time constraints it was not possible to acquire the needed generator.

It was then decided to use a larger high speed motor harvested from a laptop hard drive (center top of Figure 7.6) that fit the low profile need for implantation and could produce higher voltages than the smaller generator of the MST, even if the voltage to current ratio was lower than desired.

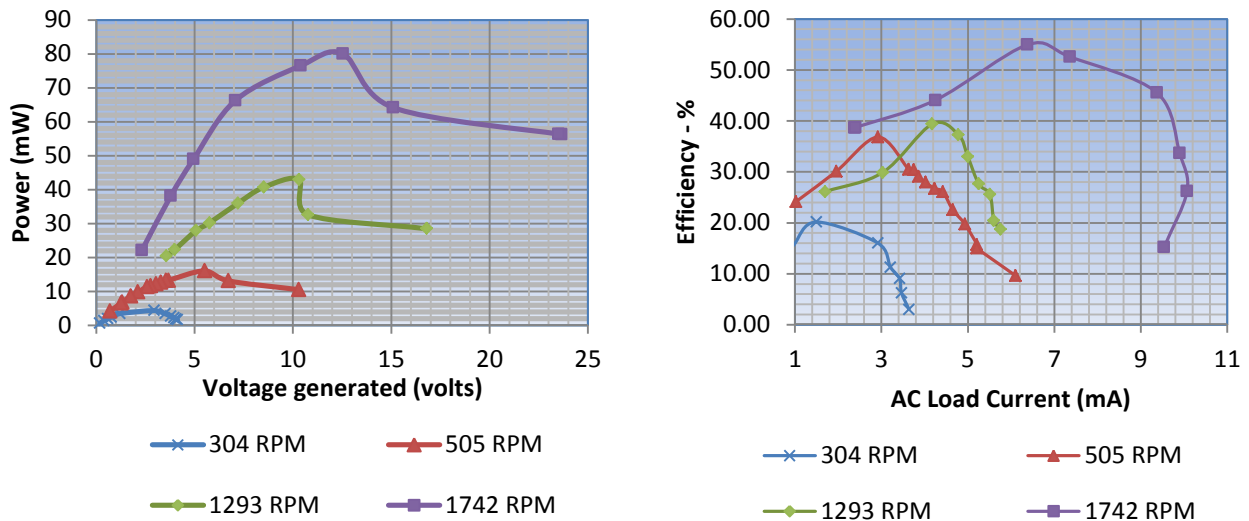


Figure 9.5 LST (N) AC power in mW vs voltage generated at increasing RPM (left) and efficiency vs AC load current in mA (right)

By miniaturizing the LST a new turbine was designed and printed, named the OTI-1 that would be based on the optimization recommendations proposed earlier. The OTI-1 is compared with the LST in Table 7.2, where a 15-fold volume reduction of the casing was achieved, as well as a 10-fold reduction in operating volume. The power curves of the OTI-1 can be seen in Figure 9.6, along with power vs voltage curves.

Notice that the OTI-1 produces higher power per RPM than the MST, as well as higher voltage as seen on the right side of the figure. The average PE and average CCE were found to be improved, 19% and 17.5% respectively. With no rectification losses, the question was posed; can this turbine be made smaller than a typical pacemaker battery?

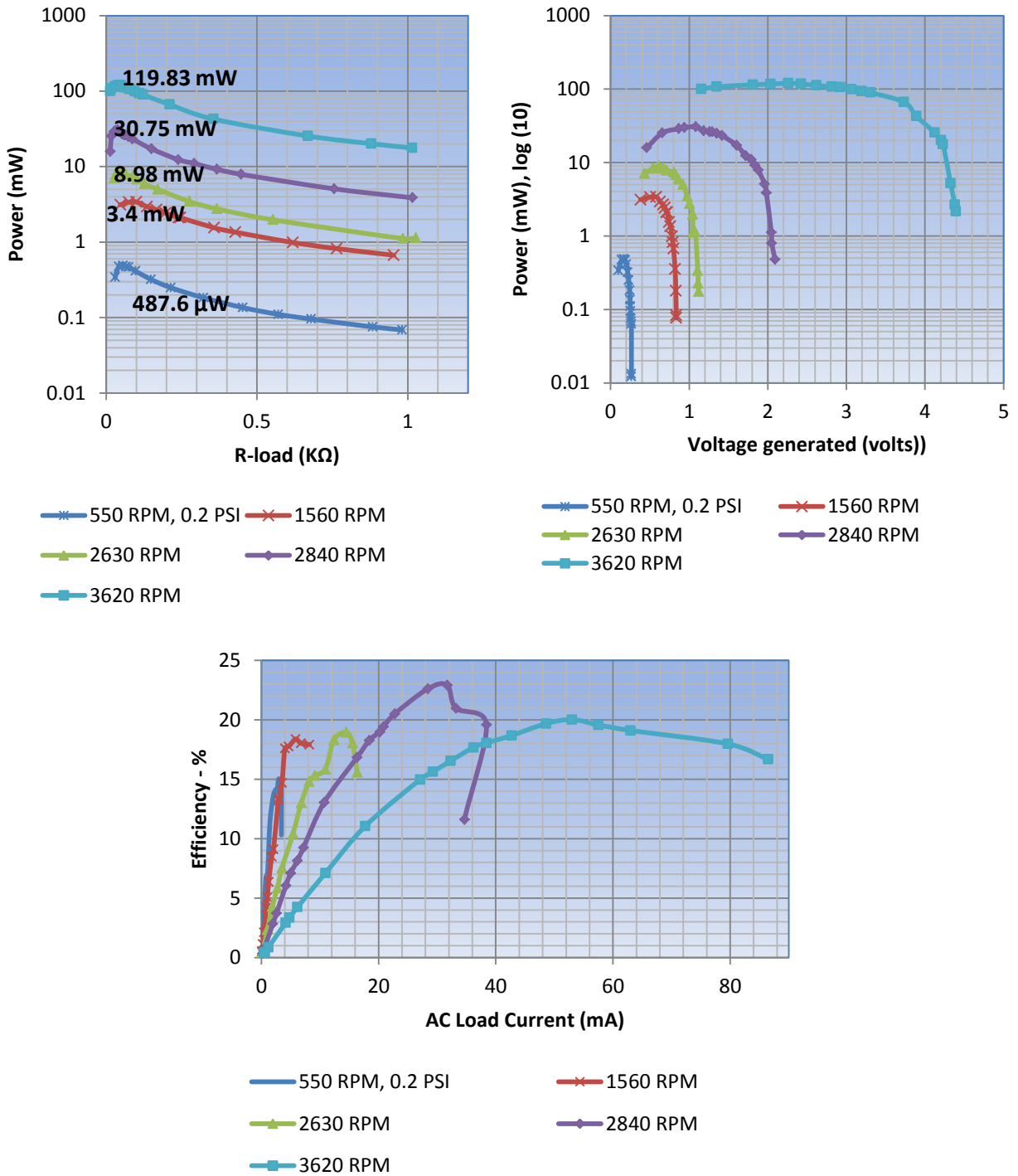


Figure 9.6 OTI-1 (N) AC power vs load resistance (left), power vs voltage (right) and efficiency vs load current in mA (bottom)



In order to answer the question posed, it was time to return to the original 18.8 mm generator of Figure 7.7 and design, 3D print and test a new turbine casing, blade assembly and connectors. It was named the optimized turbine for implantation number two (OTI-2).

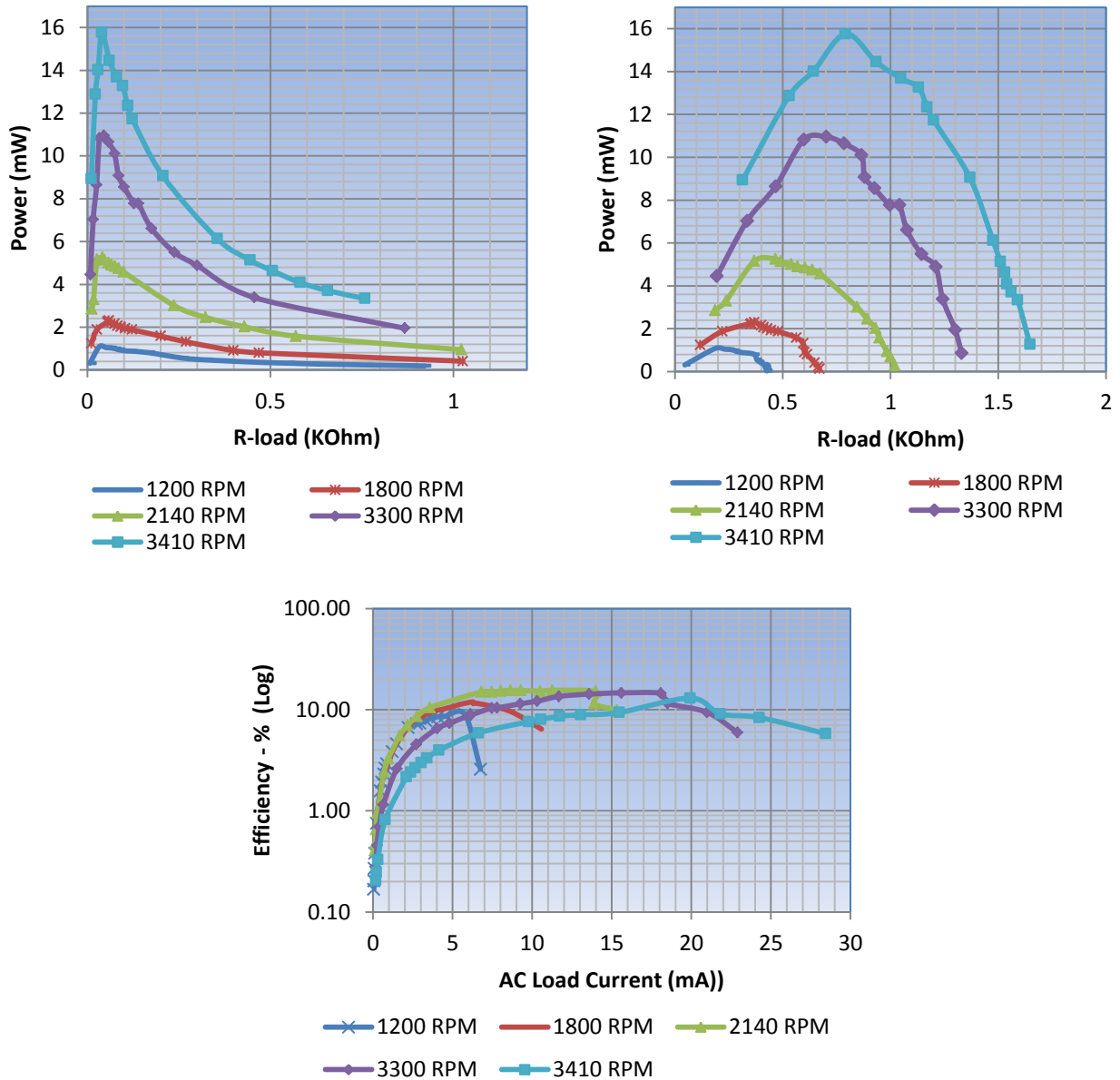


Figure 9.7 (N) AC OTI-2 power vs load resistance (left), power vs voltage (right) and efficiency vs load current in mA (bottom)

The PMMA casing was also fabricated to use as an inspection port under nitrogen flow, as it is transparent and it was possible to monitor the turbine's behavior. Later, under liquid flow testing small air bubbles were injected into the system to observe the flow characteristics through the clear tubing and casing. For now, the results of the tests using nitrogen as a harvesting source can be seen on Figure 9.7.

### **9.1.2 DC Power**

Once the OTI-2 was made smaller, more flow pressure was needed to overcome the inertia of the smaller generator with a higher internal friction. But for applications where low RPM is not a requirement, these are very good results.

Following the miniaturization of the LST down to the OTI-1 and the subsequent optimization to the OTI-2, up to 120 mW of raw power was harvested. The next logical step was to convert this raw power to a DC level by using the rectifier seen at the top center of Figure 8.5. The rectifier was connected to the MST, OTI-1 and OTI-2 turbines. The rectified voltage was then connected to the TI BQ25504 and the LTC 3105 DC to DC converters of Figure 8.5.

#### **9.1.2.1 MST DC Power**

The resulting graphs are seen in Figure 9.8 for the TI BQ25504 converter and Figure 9.9 for the LTC 3105 converter. High flow rate was needed to increase the RPM in order to compensate for the rectification losses that can amount to be more than 50%. For this reason, the  $V_{in-rms}$  voltage is much higher than the 300 mV needed by the BQ25504. The same happens with the LTC 3105 results with a slight increase of RPM. Both were able to maintain approximately 3.1 volts at the load with a peak power around 1.5 mW for the BQ25504 and 0.9 mW for the LTC 3105.

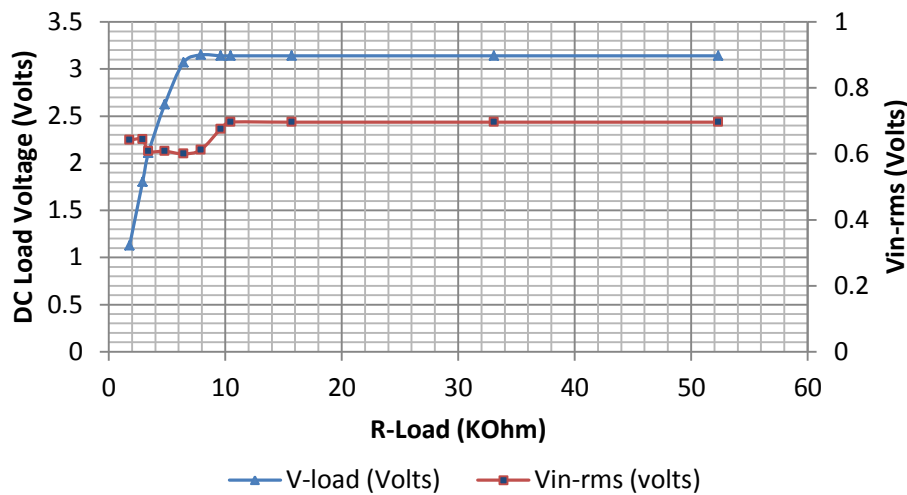
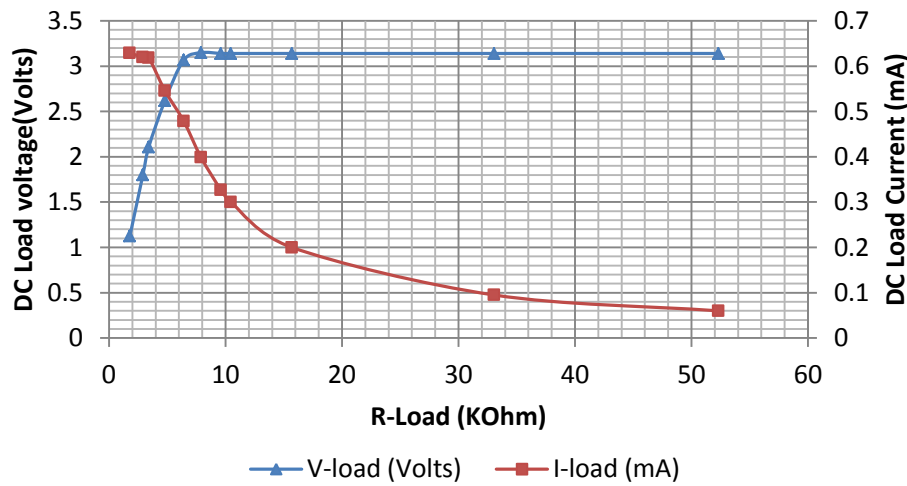
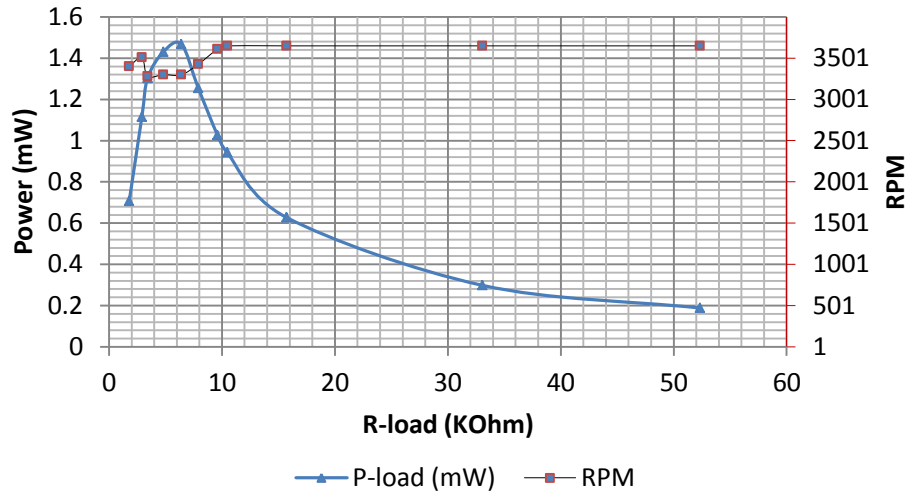


Figure 9.8 MST (N) DC power, DC load voltage/current, RPM and generator voltage against load resistance, using TI BQ 25504 to boost the voltage sent to the load.

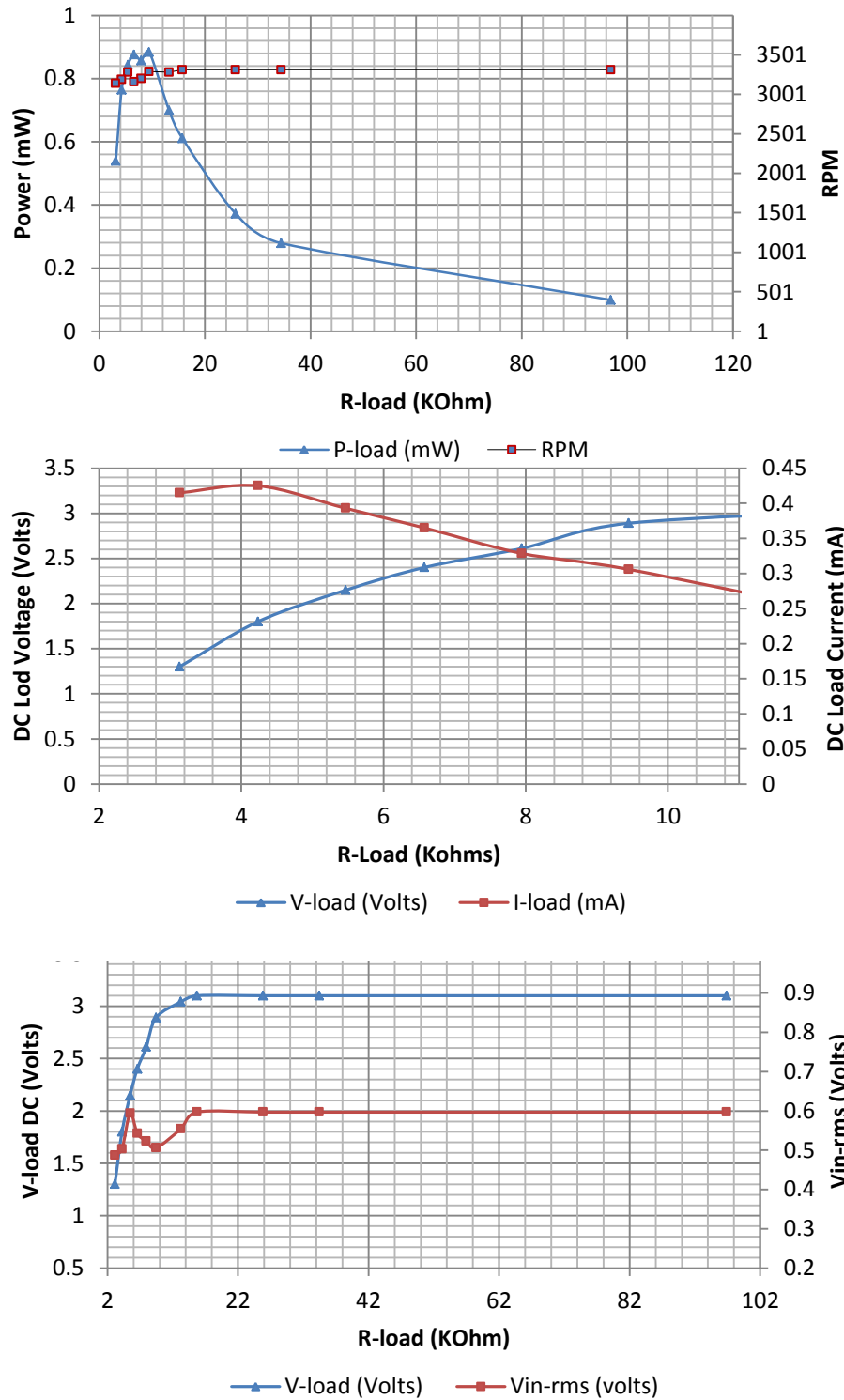


Figure 9.9 MST (N) DC power, DC load voltage/current, RPM and generator voltage against load resistance, using LTC 3105 to boost the voltage sent to the load.

### 9.1.2.2 OTI-1 DC Power

The resulting graphs for the OTI-1 turbine are presented in Figure 9.10 for the TI BQ25504 converter and Figure 9.11 for the LTC 3105 converter. High flow rate was needed to increase the RPM in order to compensate for the rectification losses causing the  $V_{in-rms}$  voltage to be higher than expected for both converters. Both converters were able to maintain approximately between 1.5 and 3.1 volts at the load at a peak power around 1.4 mW for the BQ25504 and 1.05 mW for the LTC 3105 under similar load conditions.

The generator in the OTI-1 is larger than the generator in the MST, so it is expected to see that OTI-1 requires about 1000 RPM less to maintain the 3.1 volts when compared to the MST.

### 9.1.2.3 OTI-2 DC Power

This is the last turbine to consider for the DC power harvesting from nitrogen flow, and the results can be seen in Figure 9.12 for the BQ25504 and Figures 9.13 and 9.14 for the LTC 3105. The turbine used 5000 RPM to maintain a DC voltage of 3.1 volts for former and 4500 RPM and 3000 RPM to maintain 5 volts and 3.5 volts respectively for the latter. This demonstrates the versatility of the LTC 3105 converter as it can power any system that uses a rail voltage between 1.8 and 5 volts. This is a wide margin, but the turbine must rotate at high RPMs. All in all, it is surprising that the BQ25504 requires 5050 RPM to deliver a peak power of 1.46 mW, while the LTC3105 requires 4570 RPM and delivers 3.27 mW and 3050 RPM to deliver 1.05 mW.

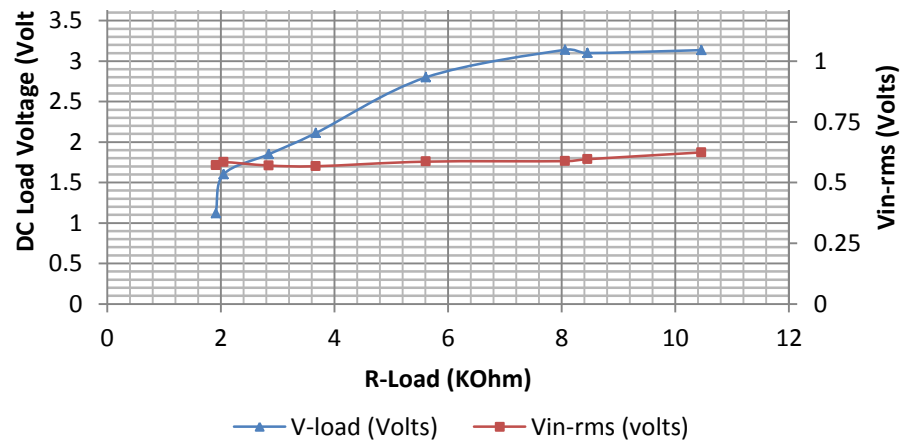
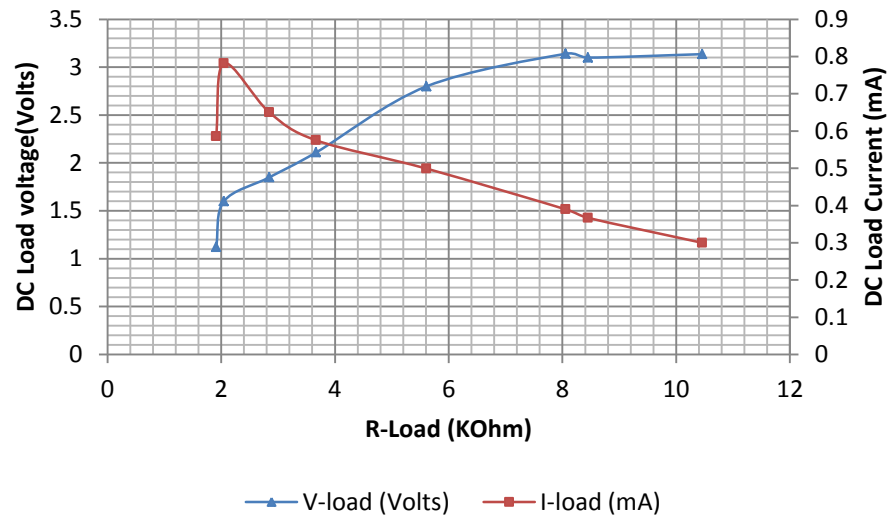
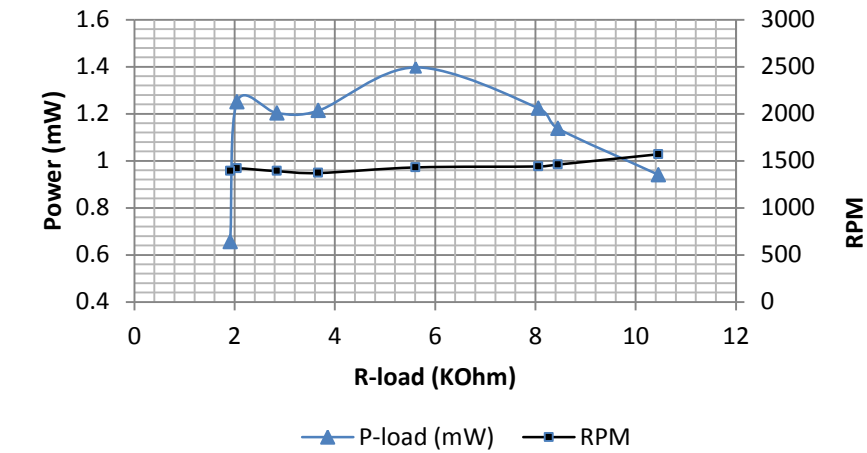


Figure 9.10 OTI-1 (N) DC power, DC load voltage/current, RPM and generator voltage against load resistance, using BQ25504 to boost the voltage sent to the load.

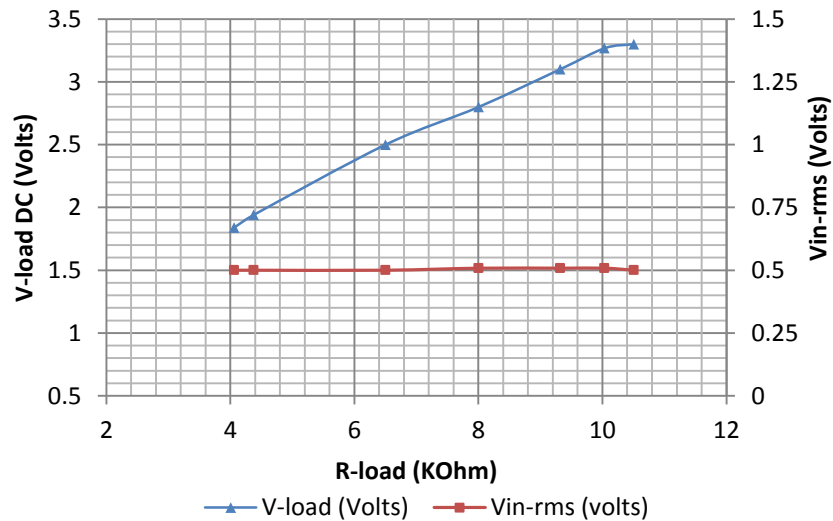
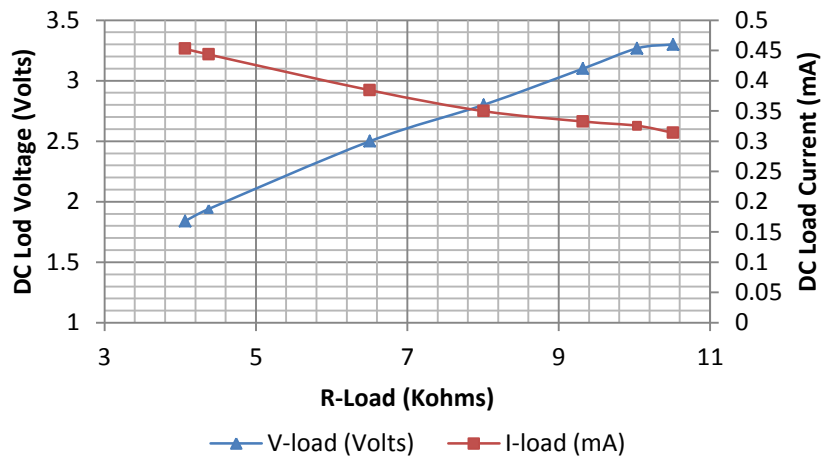
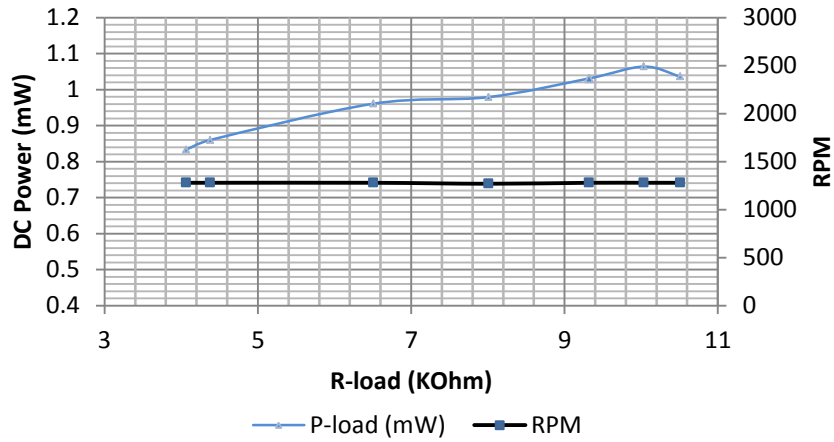


Figure 9.11 OTI-1 (N) DC power, DC load voltage/current, RPM and generator voltage against load resistance, using LTC 3105 to boost the voltage sent to the load.

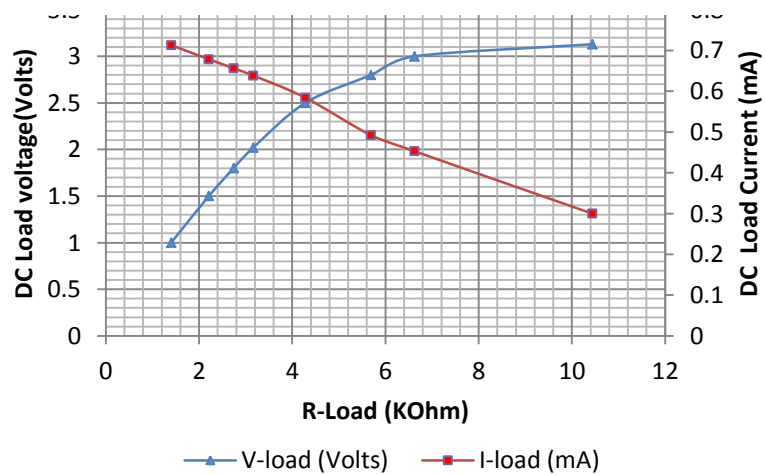
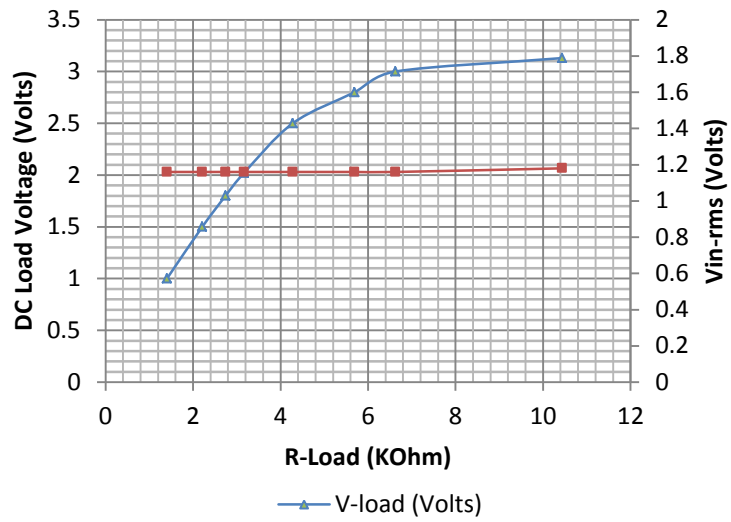
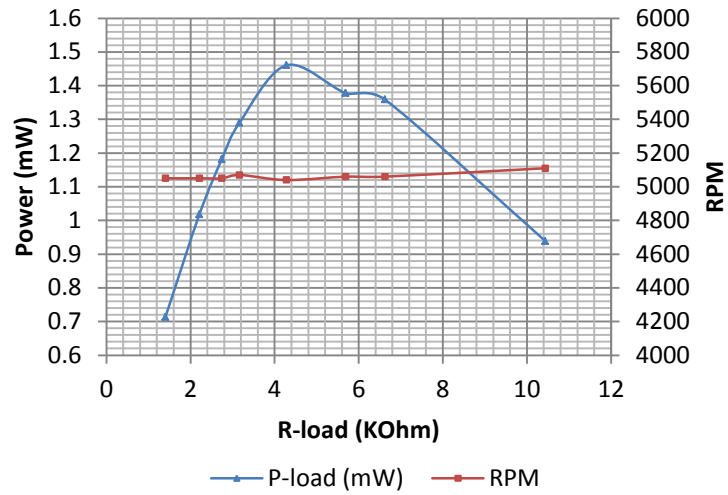


Figure 9.12 OTI-2 (N) DC power, DC load voltage/current, RPM and generator voltage against load resistance, using BQ25504 to boost the voltage sent to the load.



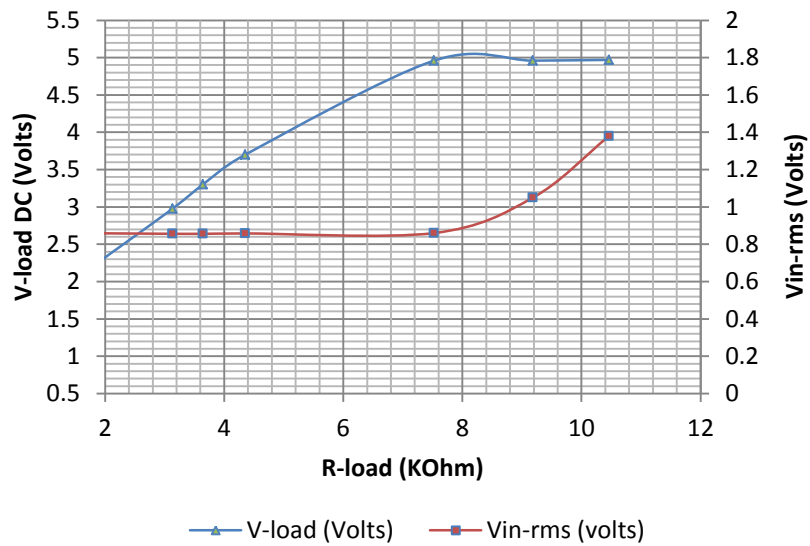
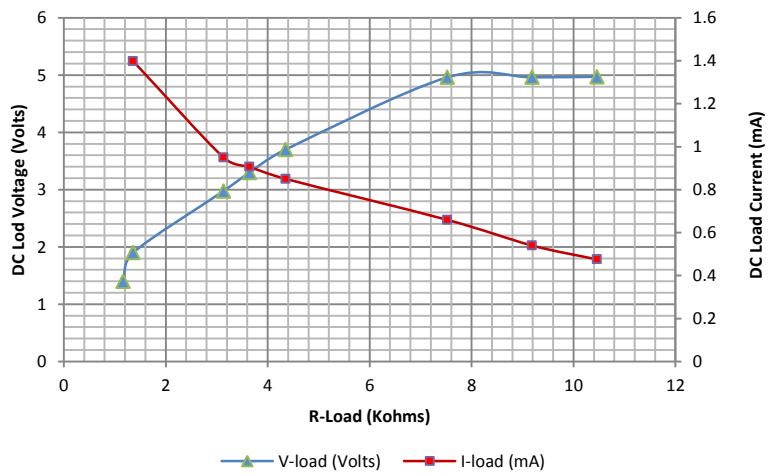
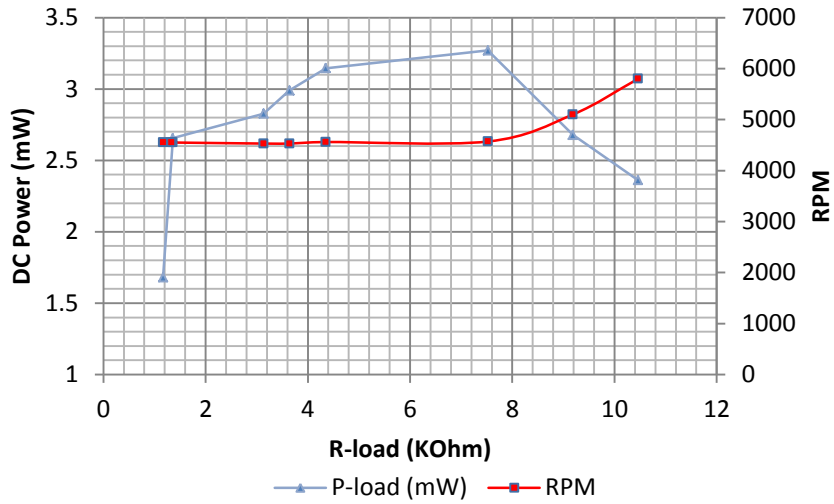


Figure 9.13 OTI-2 (N) DC power, DC load voltage/current, RPM and generator voltage against load resistance, using LTC3105 to boost the voltage sent to the load to 5 volts.

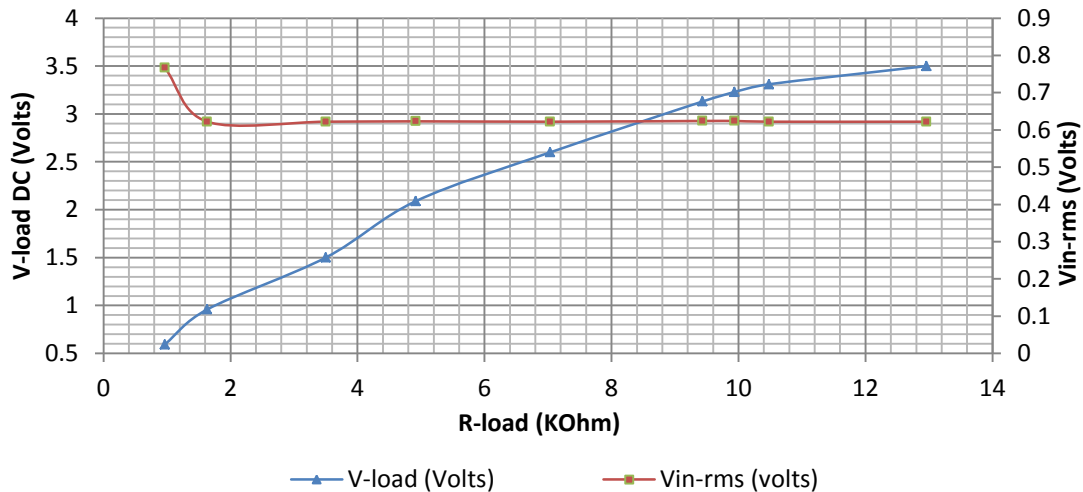
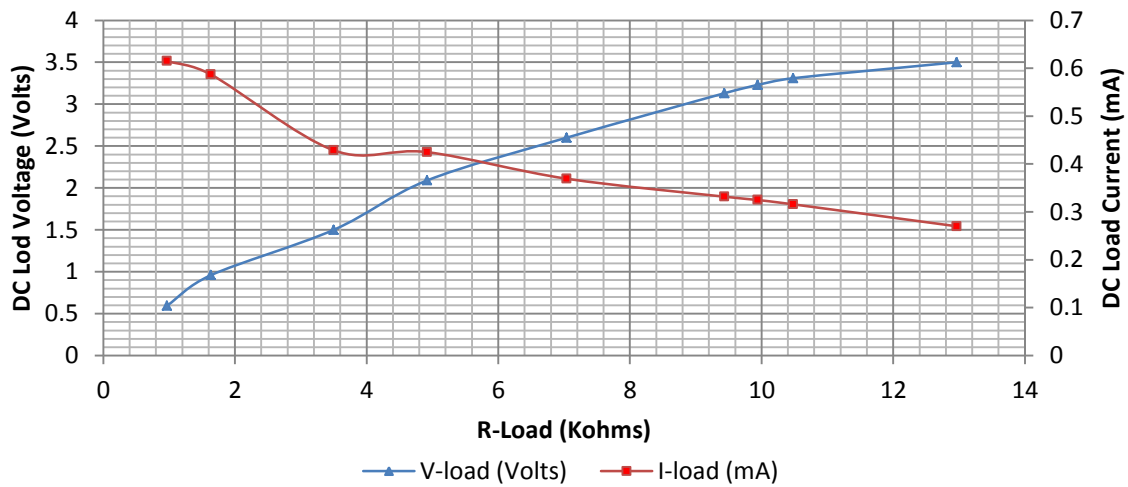
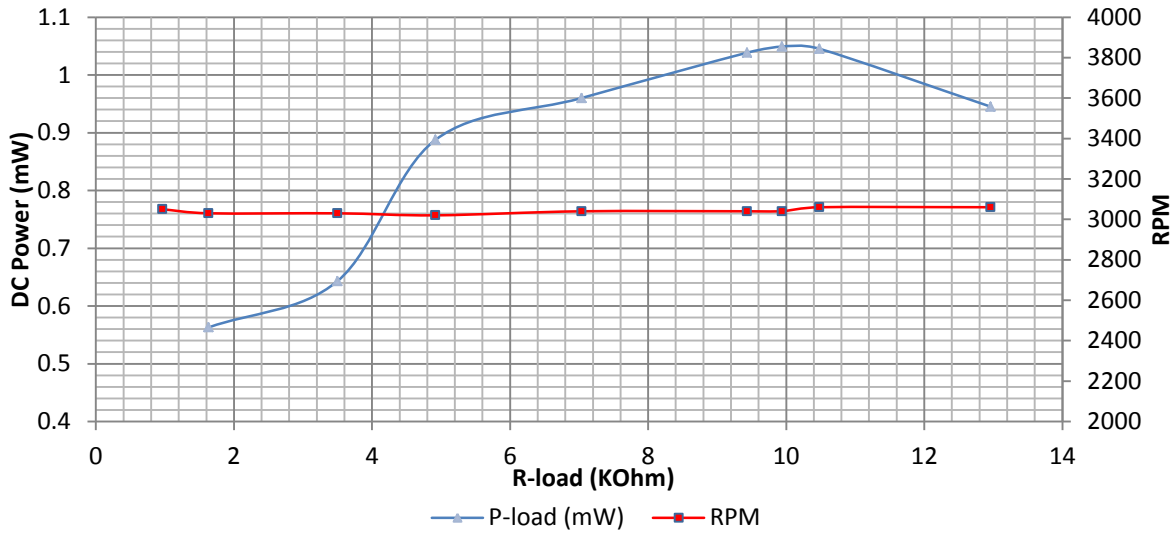


Figure 9.14 OTI-2 (N) DC power, DC load voltage/current, RPM and generator voltage against load resistance, using LTC3105 to boost the voltage sent to the load to 3.5 volts.

## 9.2 Water Flow Harvesting Results

In the next part of the evaluation the turbines were tested using water because the test could provide a basis of departure for estimating their performance using a variety of Newtonian fluids with similar density as water and foresee some performance issues that may need to be addressed before the in-vitro testing. In the following sections the versatility of these turbines can be seen as they are tested using a liquid as a harvesting source.

### 9.2.1 AC Power and Efficiency

The power curves using water flow as a harvesting source were calculated by multiplying the voltage and current at the load and the efficiency was calculated by first finding the power of the fluid flow through the turbine under the influence of the difference in pressure between its inlet and its outlet and then dividing the electrical power found at the load by the power produced by the flow. Using the Pressure-Volume-Work principle and Eq's 9.3, 9.4 and 9.5 below, where,

$$m' = v' \rho \quad (\text{Eq. 9.3})$$

and  $m'$  is the mass flow rate in Kg/sec,  $v'$  is the volumetric flow rate in  $\text{m}^3/\text{sec.}$ , and  $\rho$  is the density of the fluid in  $\text{Kg}/\text{m}^3$ . Then, if by dividing the pressure difference across the turbine by the density of the fluid, the associated work can be calculated using Eq. 9.4

$$W = (P_{in} - P_{out})/\rho \quad (\text{Eq. 9.4})$$

where  $W$  is the work in J/Kg,  $P_{in}$  and  $P_{out}$  are the pressure at the inlet and outlet of the turbine respectively in Pa ( $\text{J}/\text{m}^3$ ) and  $\rho$  is the density of the fluid in  $\text{Kg}/\text{m}^3$ .

Finally, using Eq. 9.5 the power from the flow was found as,

$$P = m' W \quad (\text{Eq. 9.5})$$

where  $P$  is the power in J/sec (Watts),  $m'$  is the mass flow rate in Kg/sec. and  $W$  is the work in J/Kg. By using substitution of Eq's 9.3 and 9.4 into Eq. 9.5, and programming the results into a spreadsheet multiple points can be calculated to obtain the average peak efficiency (PE) and the average center-of-curve efficiency (CCE) as was done previously in section 9.1.

Figure 9.15 shows the power against load resistance curves for the MST, while Figure 9.16 shows the power against rms voltage generated.

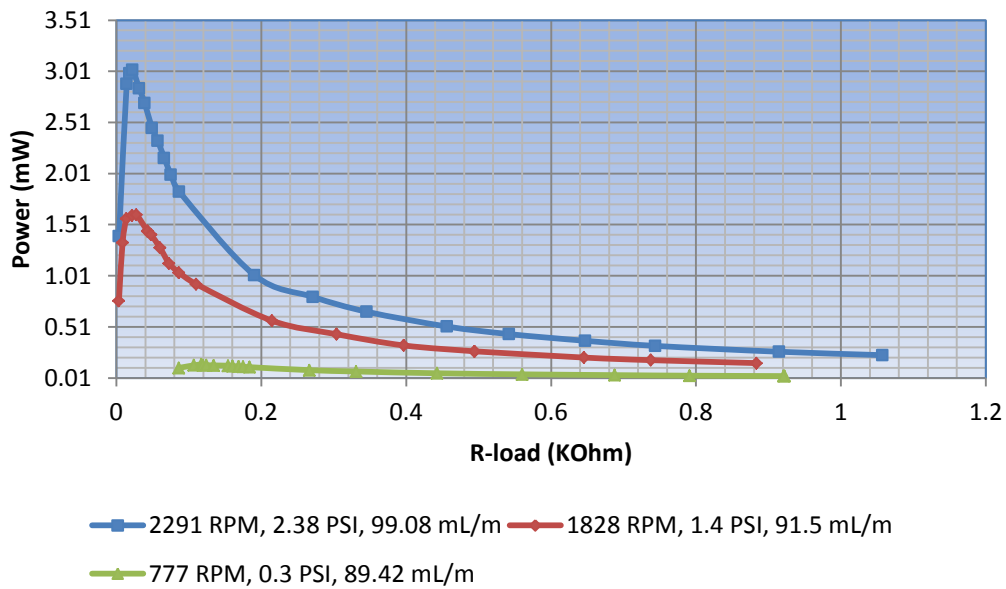


Figure 9.15 MST (W) AC power in mW vs load resistance in  $K\Omega$  for changing RPM, pressure difference in PSI and flow  $Q$  in liters/min.

The performance of these turbines in water is limited by their ability to rotate as freely as possible the way they did in nitrogen. Because water is much denser than nitrogen and the turbine blade assembly is submerged in water, the turbine is unable to achieve high RPMs, so only three power curves were plotted. This difference in density will also translate into a decrease in efficiency and lower output voltage as suggested by Figure 7.16 where the generator was only able to reach a 500 mV rms output. The MST's average CCE efficiency in water was found to be 8.1% and the PE, 9.1%

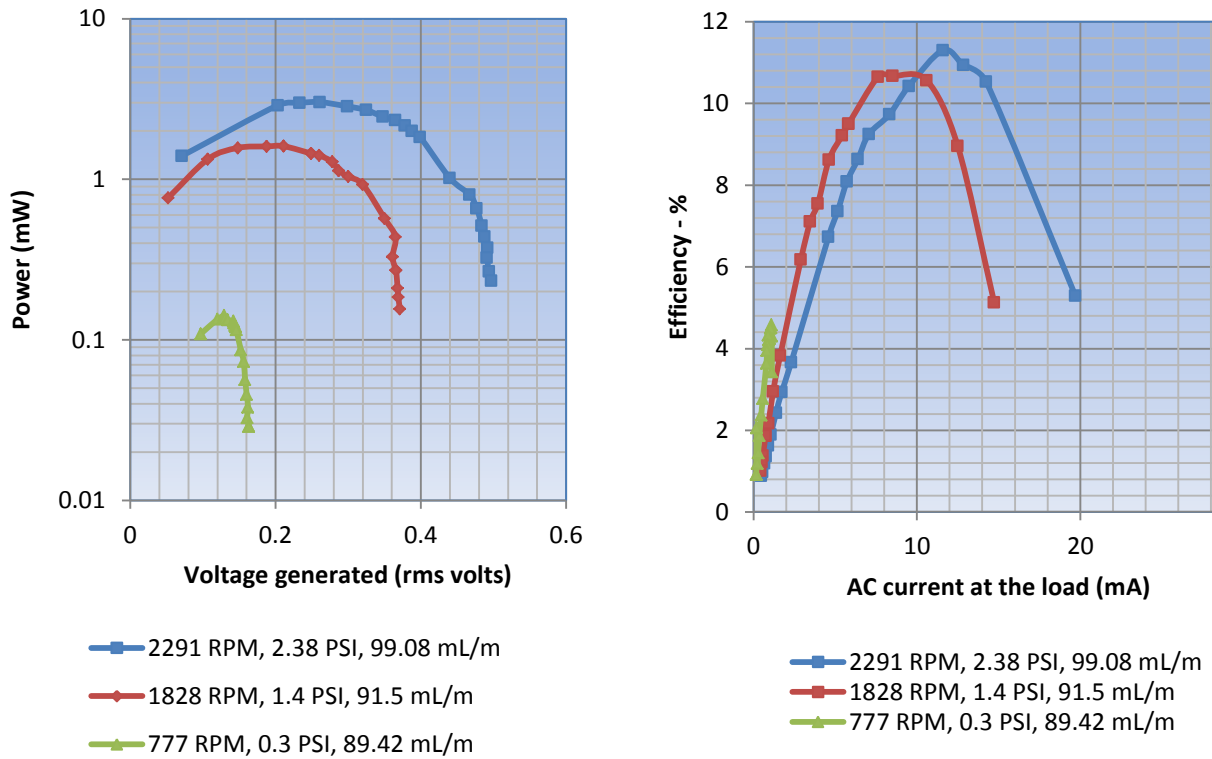


Figure 9.16 MST (W) AC power in mW vs generated rms voltage in volts for different RPM, pressure difference in PSI and flow  $Q$  in mL/m (left) and efficiency vs load current in mA (right)

The pressure difference in PSI represents the PSI drop across the turbine that sustains the given flow and produces the RPM rotation given. The power curves for OTI-1 can be seen in Figures 9.17 and 9.18 and those for OTI-2 appear in Figures 9.19 and 9.20.

### 9.2.2 Water Flow Harvesting DC Power

In order to find the power curves of the DC load, the single diode rectifier was connected to the MST, OTI-1 and OTI-2 turbines. The rectified voltage was then connected to the TI BQ25504 and the LTC 3105 DC to DC converters of Figure 8.5. These two converters afforded two different startup voltages at 385 mV and 200 mV minimum respectively.

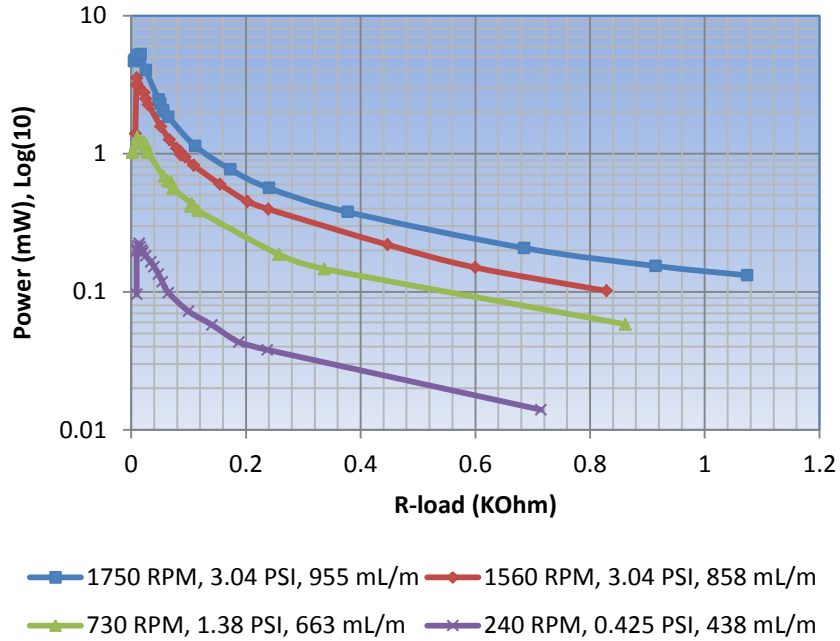


Figure 9.17 OTI-1 (W) AC power in mW vs load resistance in KΩ for changing RPM, pressure difference in PSI and flow  $Q$  in liters/min

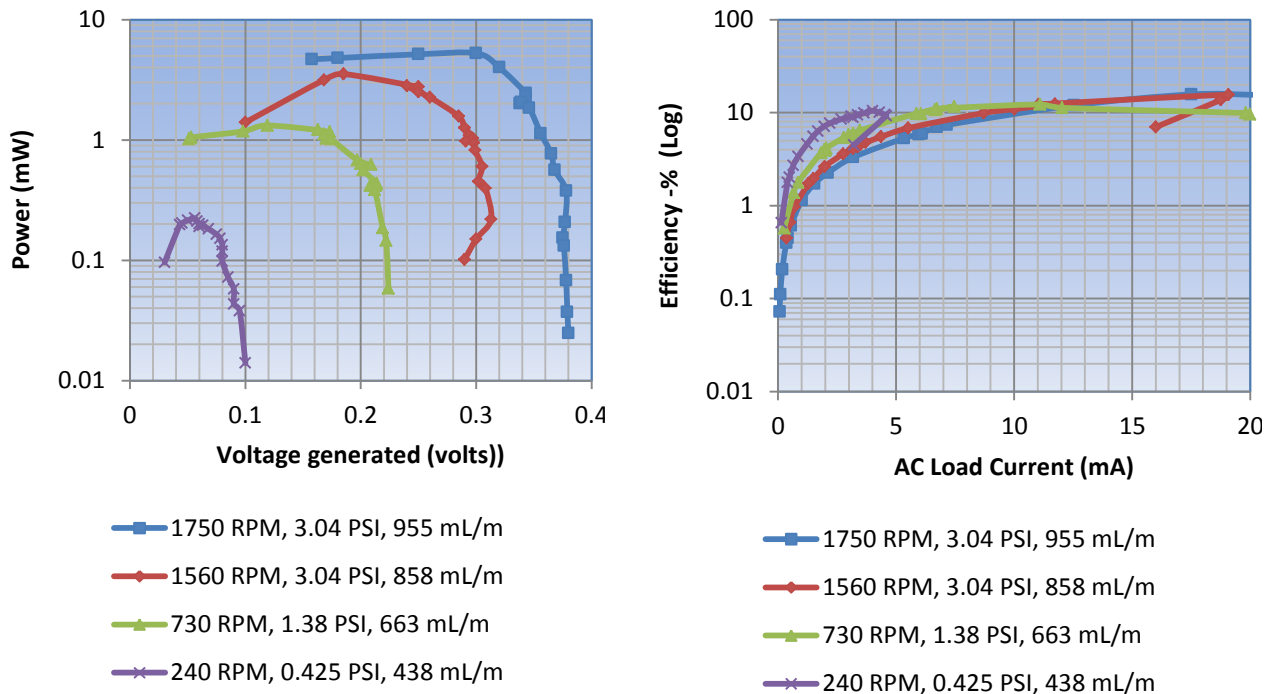


Figure 9.18 OTI-1 (W) AC power in mW vs generated rms voltage in volts for different RPM, pressure difference in PSI and flow  $Q$  in mL/m (left) and efficiency vs load current (right)

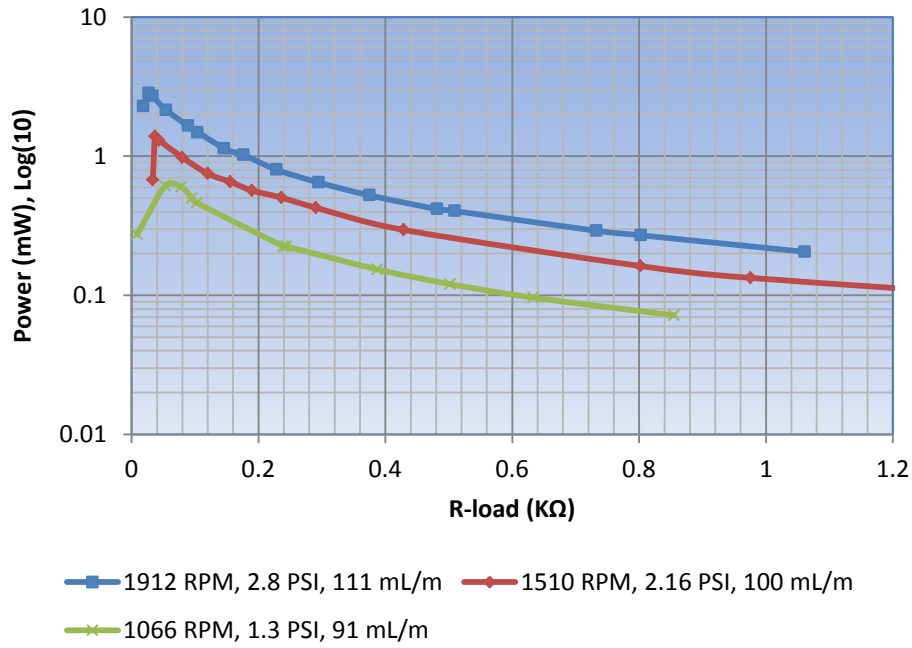


Figure 9.19 OTI-2 (W) AC power in mW vs load resistance in KΩ for changing RPM, pressure difference in PSI and flow Q in liters/min

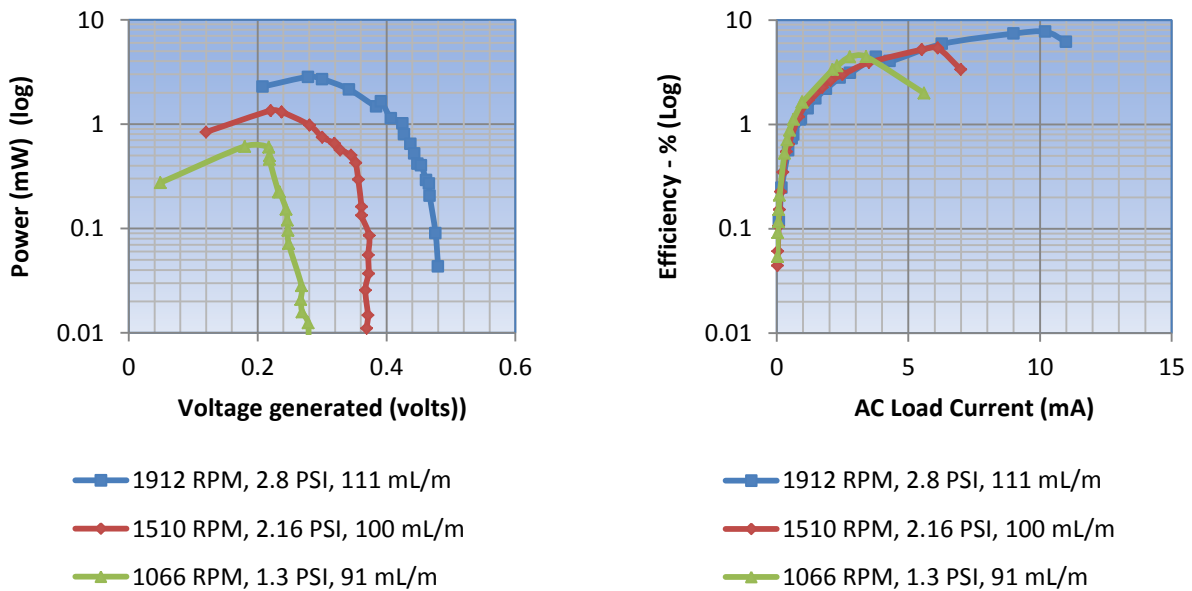


Figure 9.20 OTI-2 (W) AC power in mW vs generated rms voltage in volts for different RPM, pressure difference in PSI and flow Q in mL/m (left) and efficiency vs load current in mA (right)

### 9.2.2.1 MST DC Power

The graphs that resulted from the testing of the MST are seen in Figure 9.21 using the TI BQ25504 DC to DC converter and Figure 9.22 using the LTC 3105 converter.

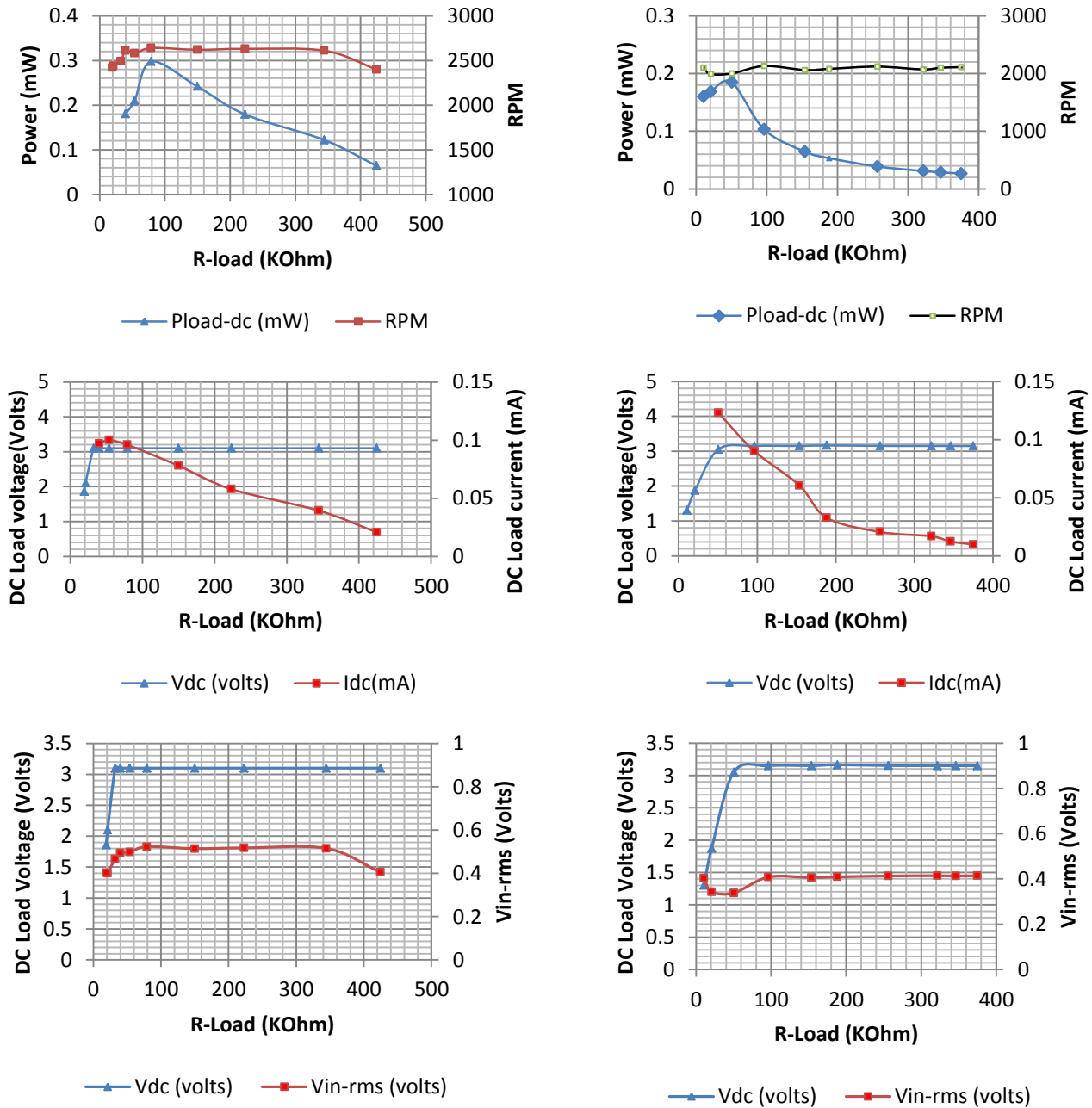


Figure 9.21 MST (W) DC power, DC load voltage/current, RPM and generator voltage against load resistance, using TI BQ 25504 to boost the voltage sent to the load at 2600 RPM (left) and at 2100 RPM (right).



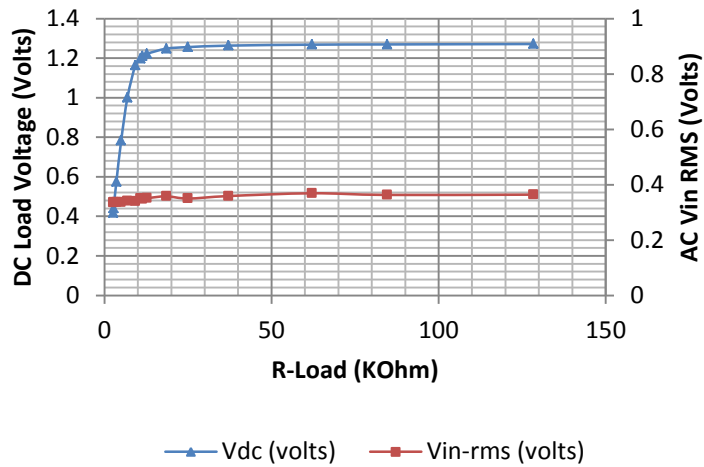
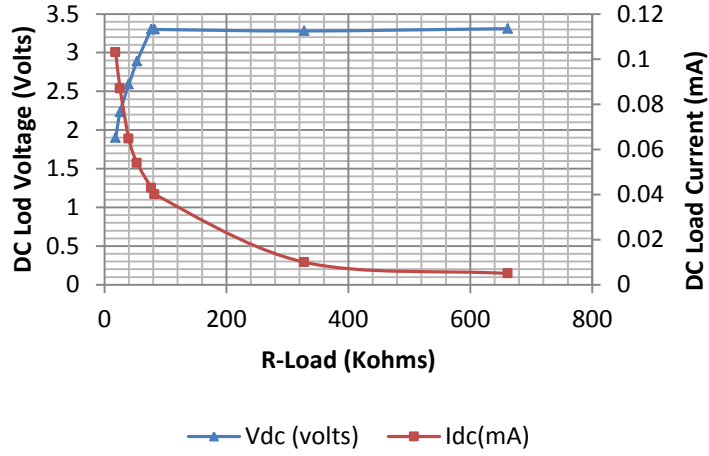
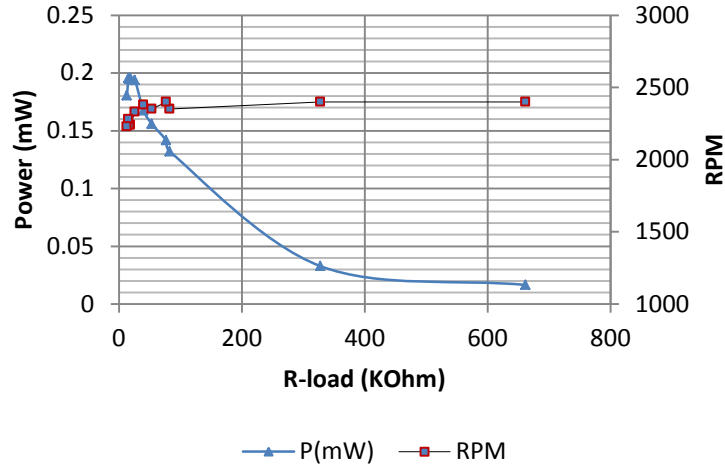


Figure 9.22 MST (W) DC power, DC load voltage/current, RPM and generator voltage against load resistance, using LTC 3105 to boost the voltage sent to the load.

### 9.2.2.2 OTI-1 DC Power

In a similar manner to the DC measurements in nitrogen, the OTI-1 DC measurements graphs using water flow as a harvesting source were obtained.

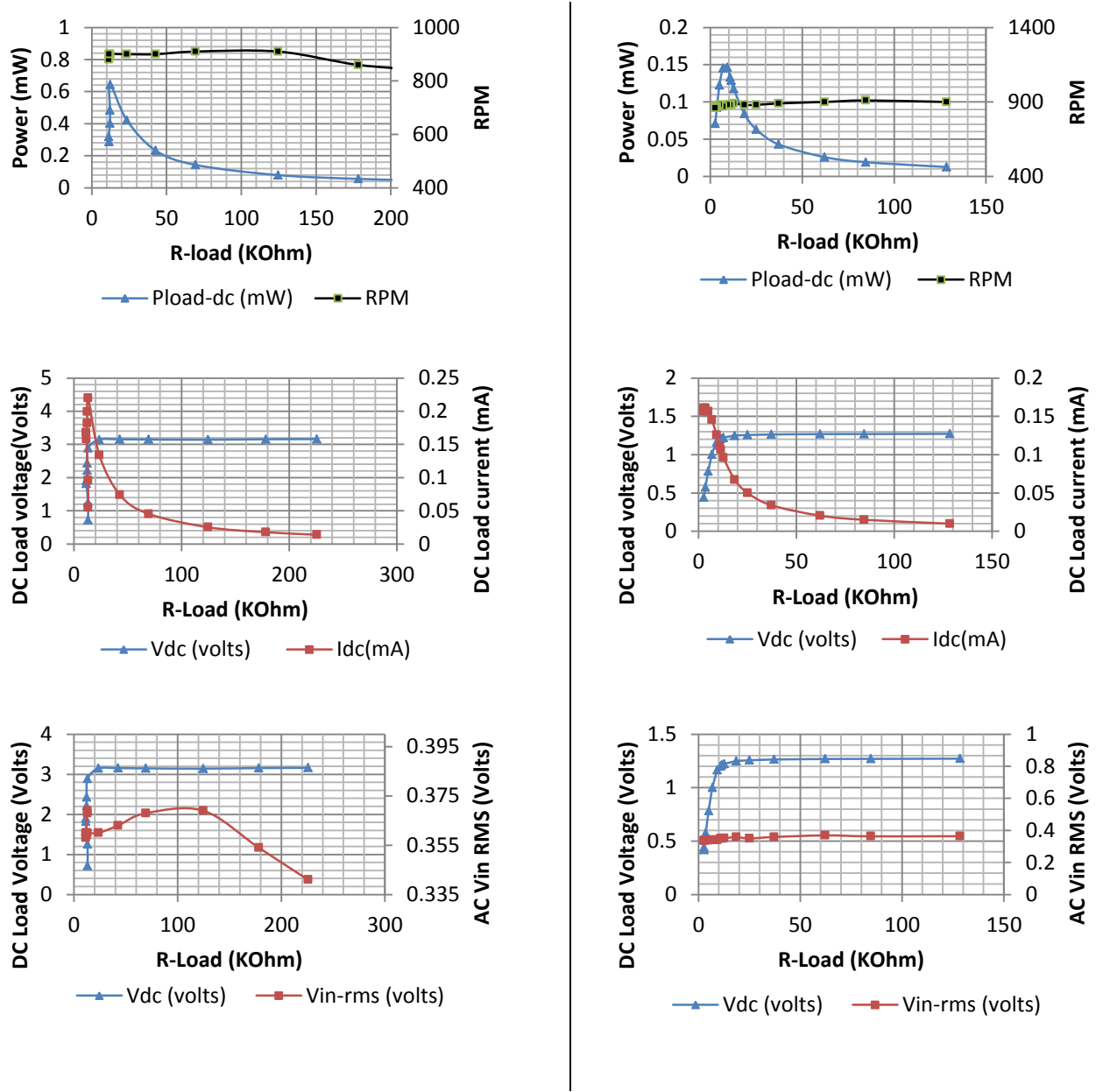


Figure 9.23 OTI-1 (W) DC power, DC load voltage, DC load current, RPM and RMS generator voltage against load resistance, using TI BQ 25504 (left) and LTC 3105 (right)

In Figure 9.23 one can see the behavior of the OTI-1 using water. Since the OTI-1 has a larger diameter than the MST, the RPM is much lower than that of the MST to maintain 3.1 volts at the load using the BQ25504. But the LTC 3105 was only able to maintain between 1 and 2 volts at the load, perhaps due to differences in input impedance.

### 9.2.2.3 OTI-2 DC Power

Lastly, Figure 9.24 shows the behavior of turbine OTI-2 in water, using both the BQ25504 and the LTC 3105. Notice that the BQ25504 is able to maintain 3.1 volts at the load demanding 2000 RPM from the generator which then generates almost 500 mV, half of which is lost at the rectifier. The LTC 3105 on the other hand is only able to source up to 2.5 volts to the load. This can be seen by comparing the power curves, where the LTC 3105 only produces 130  $\mu$ W and the BQ255 is able to produce over 500  $\mu$ W.

## 9.3 Simulated Blood Flow Harvesting Results

The turbines' behavior has examined through a thorough characterization process using nitrogen and water as harvesting sources. This chapter is concluded by examining the results of the in-vitro tests conducted on the two turbines that were optimized for implantation, the OTI-1 and the OTI-2.

### 9.3.1 AC Power and Efficiency

The power curves using simulated blood (SB) flow as a harvesting source were calculated by multiplying the voltage and current at the load and the efficiency was calculated by the same methodology employed in the previously with water and explained in section 9.2.1 with small adjustments for the density  $\rho$  since the density of blood is slightly higher than that of water.

Figure 9.25 displays the AC power.

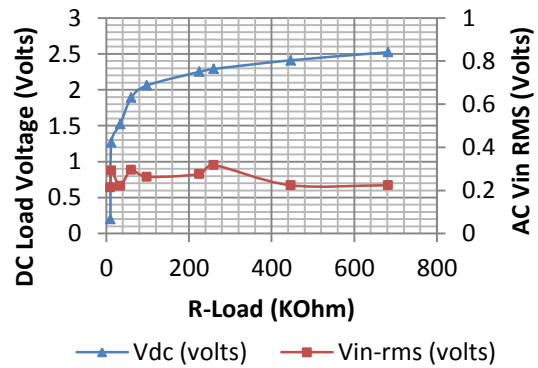
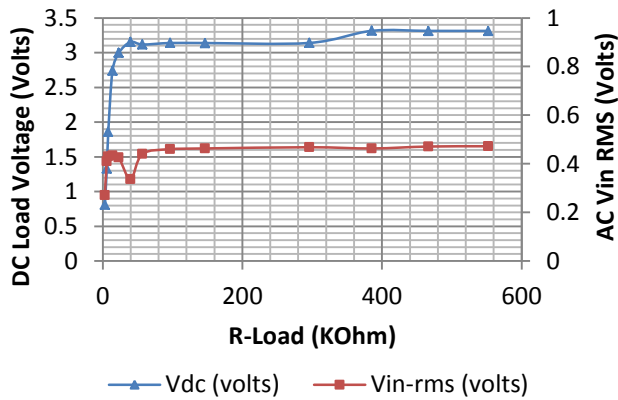
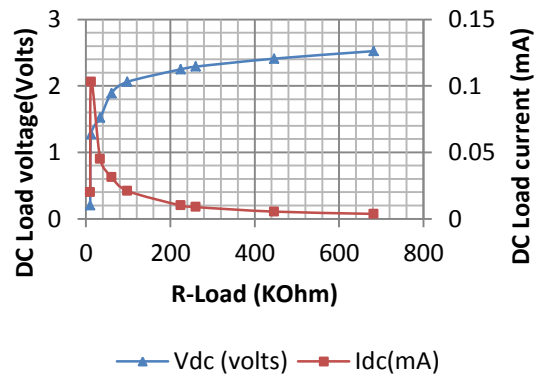
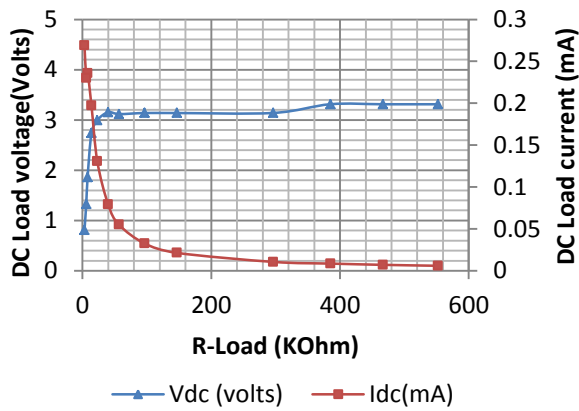
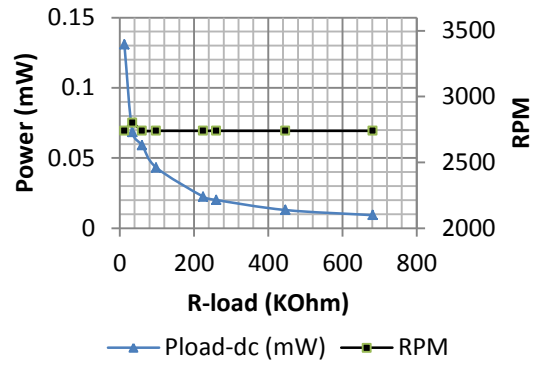
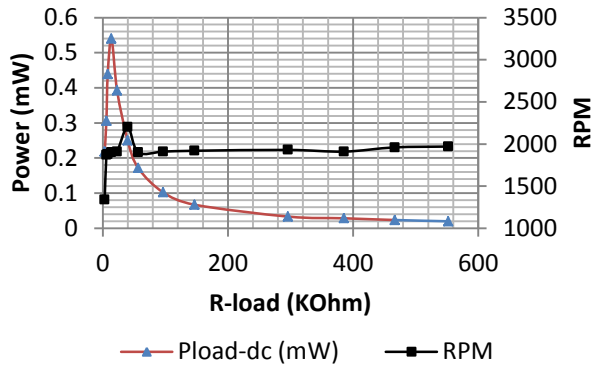


Figure 9.24 OTI-2 (W) DC power, DC load voltage, DC load current, RPM and RMS generator voltage against load resistance, using TI BQ 25504 (left) and LTC 3105 (right)

The power vs load resistance curves can be seen in Figure 9.25 and the power vs the generated voltage,  $V_{in-rms}$  appear in Figure 9.26. Given that these turbines are optimized for use as implantable devices, this time it is important to minimize the RPM to ensure that the pressure drop across the turbine is as small as possible to prevent any adverse effects in the body. The peak and average efficiencies were calculated and found to be  $PE = 10.2\%$  and  $CCE = 4.3\%$ . These low efficiency values were expected, since the turbine is immersed in the fluid and has to rotate at lower speeds to prevent shear rates associated with hemolysis and platelet activation.

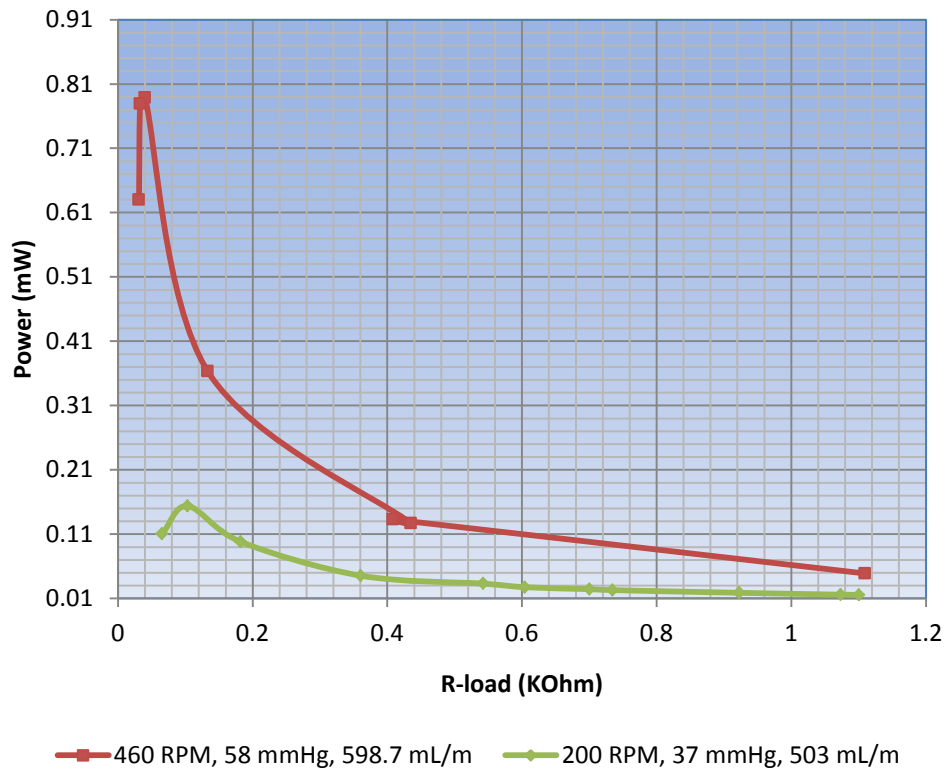
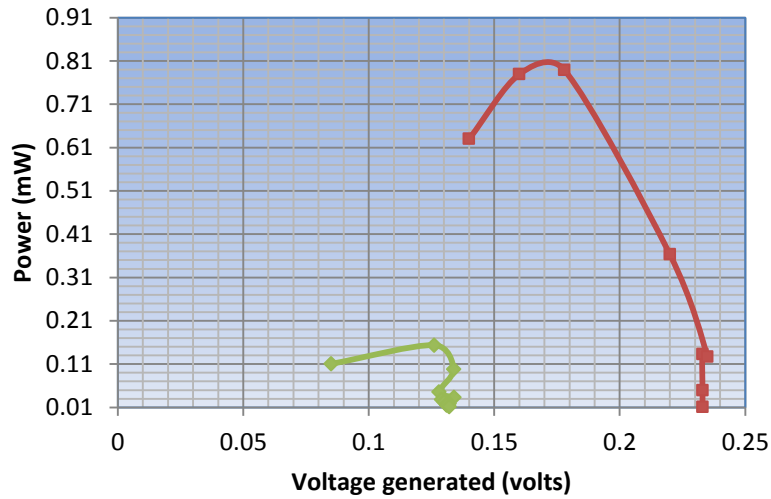
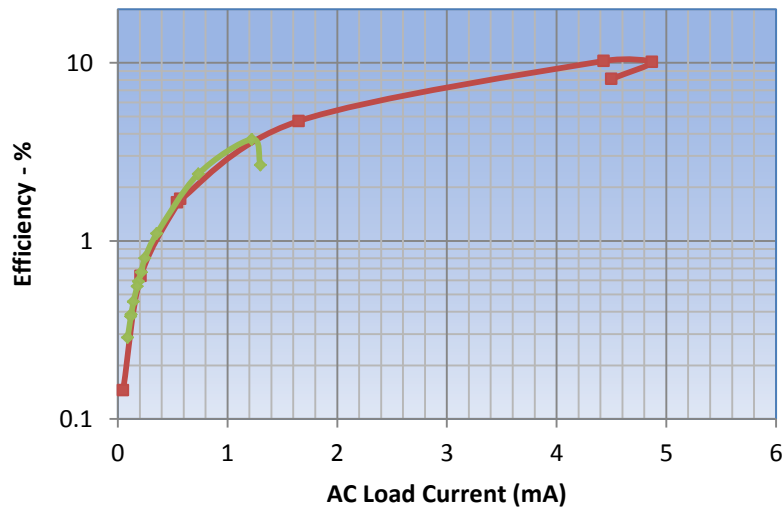


Figure 9.25 OTI-1 (SB) AC power in mW vs load resistance in  $K\Omega$  for changing RPM, pressure difference in mmHg and flow Q in mL/min



■ 460 RPM, 58 mmHg, 598.7 mL/m  
◆ 200 RPM, 37 mmHg, 503 mL/m



■ 460 RPM, 58 mmHg, 598.7 mL/m  
◆ 200 RPM, 37 mmHg, 503 mL/m

Figure 9.26 OTI-1 (SB) AC power in mW vs generated rms voltage in volts for different RPM, pressure difference in mmHg and flow  $Q$  in mL/m (top) and efficiency vs load current (bottom)

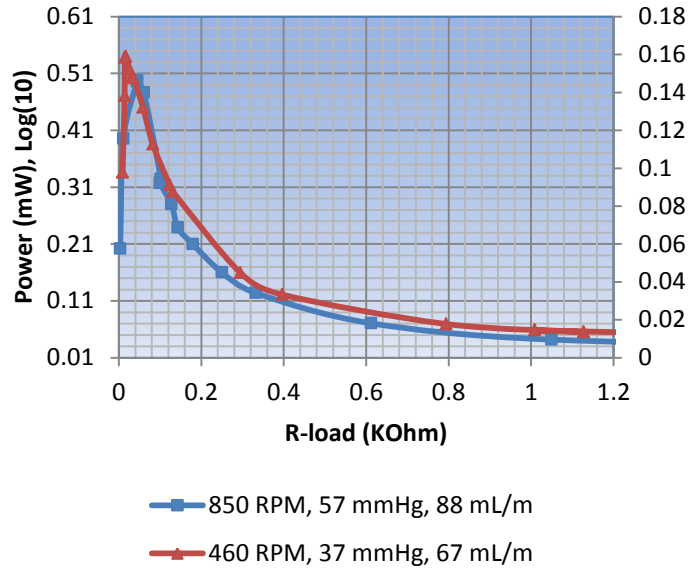


Figure 9.27 OTI-2 (SB) AC power in mW vs load resistance in KΩ for changing RPM, pressure difference in PSI and flow Q in mL/min

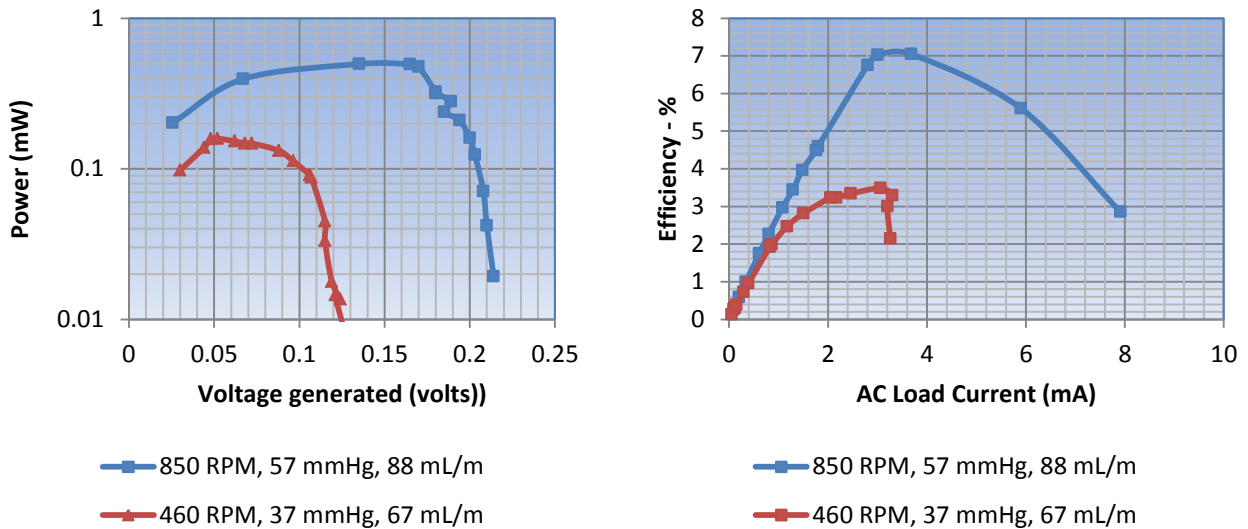


Figure 9.28 OTI-2 (SB) AC power in mW vs generated rms voltage in volts for different RPM, pressure difference in mmHg and flow Q in mL/m and efficiency vs load current in mA (right)

In Figures 9.27 and 9.28 the AC power curves for OTI-2 are displayed. This turbine is in fact smaller than OTI-1 allowing for easier implantation, but at a reduced power tradeoff. See Table 7.4 for feature size comparisons between OTI-1 and OTI-2.

The power that is seen in Figure 9.25 is sufficient to power many IMDs including a pacemaker which only requires approximately 10 to 20  $\mu\text{W}$  according to [94].

This power is considered raw power that needs to be rectified and rectification losses are very substantial. So at this juncture the author decided to investigate a way to dispense with the rectifier by using a DC to DC converter that accepts either polarity and given the fact that low RPMs produce low frequencies seen by the converter as a changing polarity at the input, the LTC 3109 converter was considered because it allows both polarities. The LTC 3109 evaluation board was not available in time so an experiment was devised with the LTC 3108 which is able to produce 2.2 volts from an input 20 mV or higher. It was hoped that the LTC 3108 would see at least 20 mV during the positive half cycle of the generator's output and still be able to produce enough power to source the most common IMDs available.

### **9.3.2 DC Power**

Two LTC 3108 DC to DC converters were used to proceed with the turbine evaluations and it was found that in fact the converter could be connected directly to the generator without using a rectifier in between. This is possible because the cold start unit of the DC to DC converter has a reverse voltage protection diode that attenuates any negative spikes that may surge in the input voltage [95] as is the case of the BQ25504. In the case of the LTC family, the Zener diode seen at input pin C1 on the LTC3108 will also ground a negative peak [96]. Therefore the generator output's sinusoidal negative half cycle is grounded, while the low frequency positive half cycle is passed and seen as a variable fluctuating positive level which is accepted by the converter according to the datasheet. This allowed the avoidance of the losses associated with the rectifier and it was possible to run the turbines at lower RPMs to reduce the pressure drop across the turbine to the lowest possible level.



Although this is not the recommended use of these converters, connecting the output of the generator directly to the converter facilitated the completion of this work, showing the proof of concept presented by the thesis in section 1.1, that it is possible to use the SIPS to harvest enough energy from the flow of the blood in the circulatory system for powering an IMD.

### **9.3.2.1 OTI-1 DC Power**

The resulting power, voltage, current, RPM and  $V_{in-rms}$  graphs are seen in Figure 9.29 for the LTC 3108 supercap DC to DC converter (left) and for the LTC 3105 femto converter (right). Both converters manage to maintain over two volts at the load, but the LTC 3108 Supercap was only able to produce between 50 and 60  $\mu W$  due to the fact that it demands a lot of current to charge its capacitors, while the femto passes all the power to the load.

### **9.3.2.2 OTI-2 DC Power**

The BQ25504 was then tested with the OTI-2, which produced some meaningful results presented below. Figure 9.30 displays the results using the BQ25504 with no rectifier. Figure 9.31 shows the findings using the LTC 3108 supercap and LTC 3108 femto also without rectification. It is quite remarkable that the OTI-2 being a smaller turbine is able to achieve a higher voltage over 3 volts when connected directly to the LTC 3108 femto, and that is so because there is close match in impedance between the two.

The original 18.8 mm diameter generator has an input impedance of approximately 7.3  $\Omega$  per coil, but when two contiguous phases are taken together they add up to 14.6  $\Omega$ , which is very close to the input impedance of the LTC 3108 femto board's of 12.6  $\Omega$ . This matching is only possible at very low frequencies, where the real part of the complex impedance dominates and the imaginary part approaches zero.

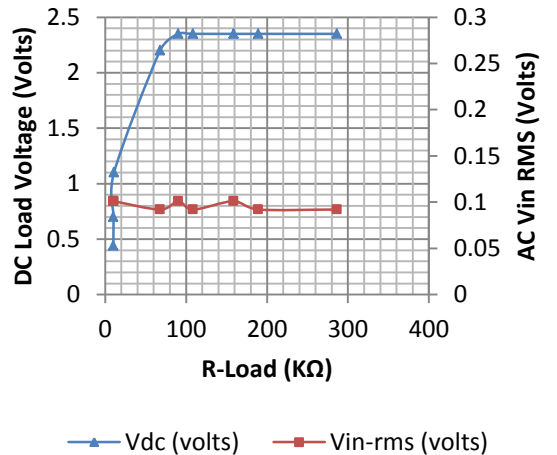
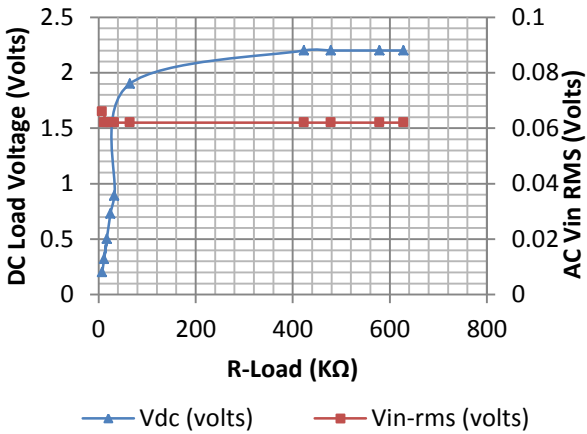
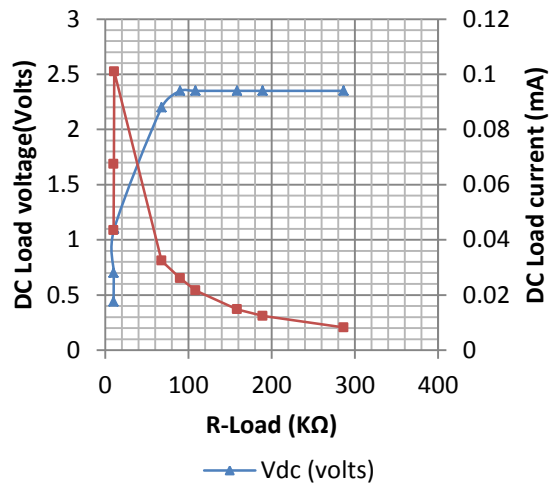
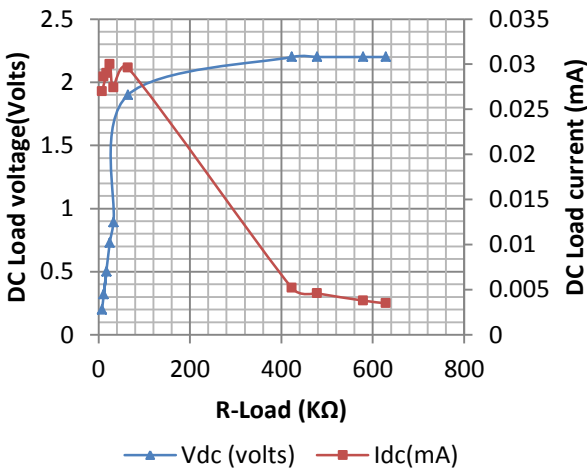
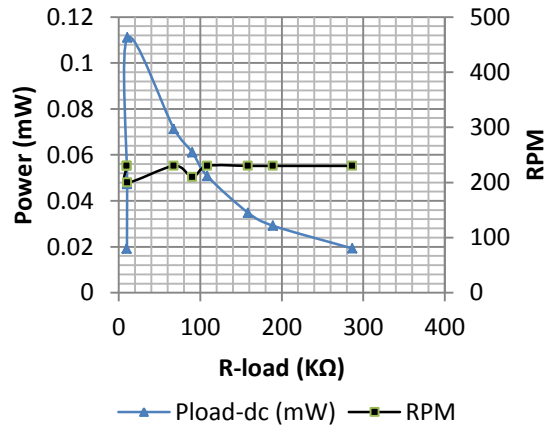
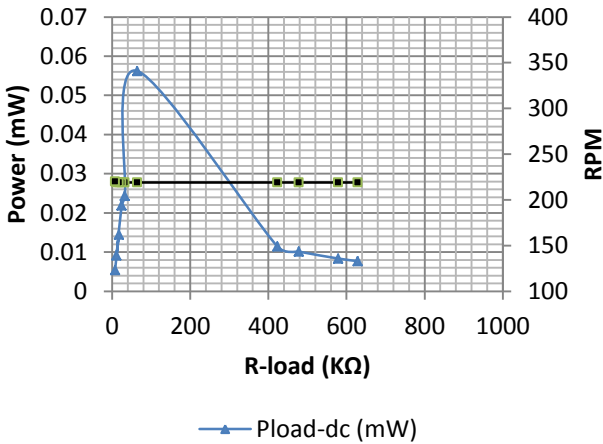


Figure 9.29 OTI-1 (SB) DC power, DC load voltage, DC load current, RPM and rms generator voltage against load resistance, using LTC 3108 Supercap (left) and LTC 3108 femto (right)

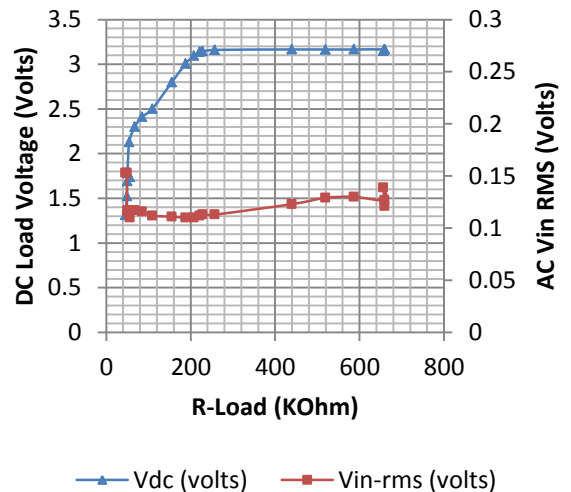
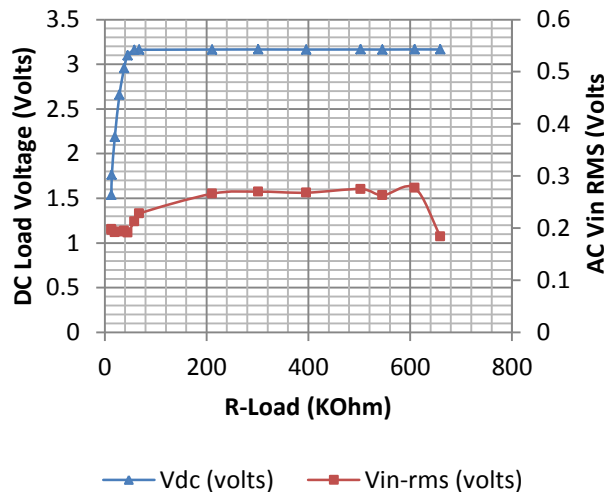
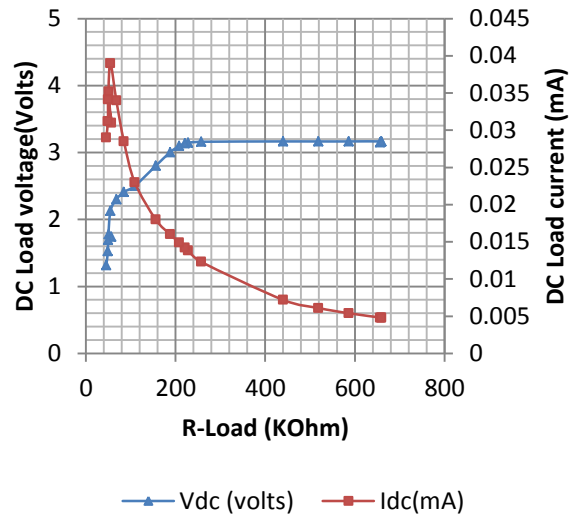
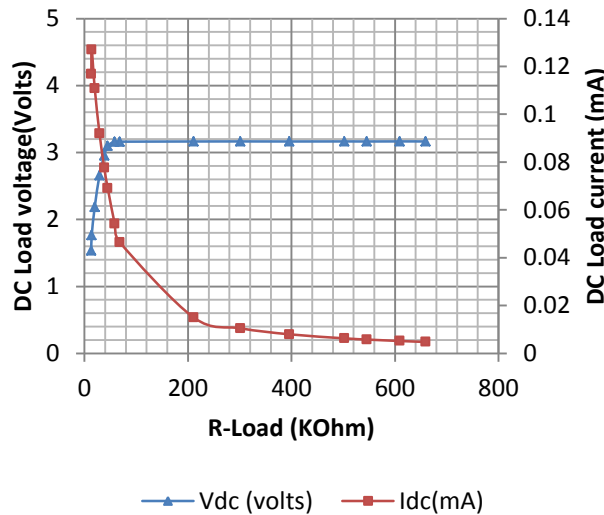
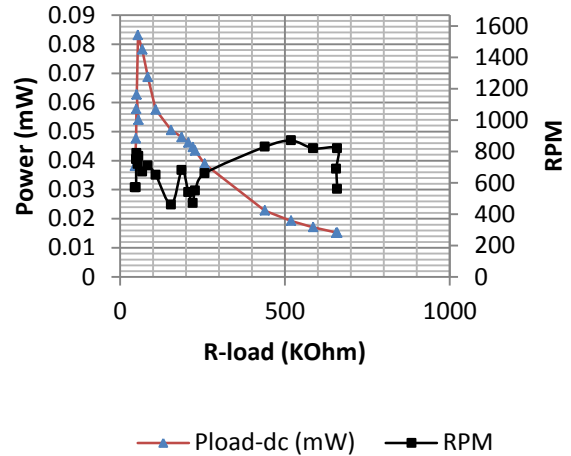
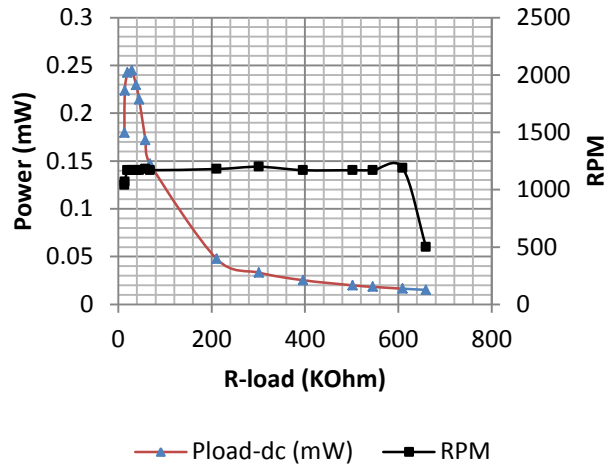


Figure 9.30 OTI-2 (SB) DC power, DC load voltage, DC load current, RPM and rms generator voltage vs load resistance, using BQ 25504 above 1000 RPM (left) and below 1000 RPM (right)

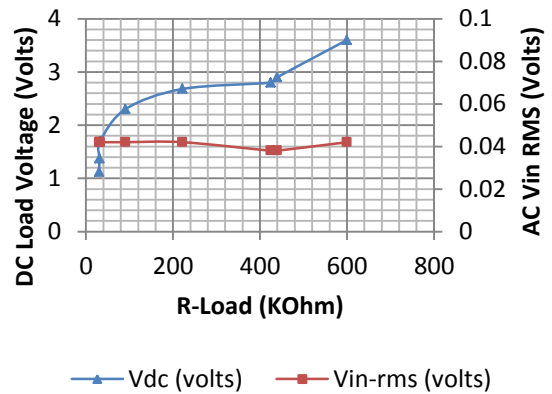
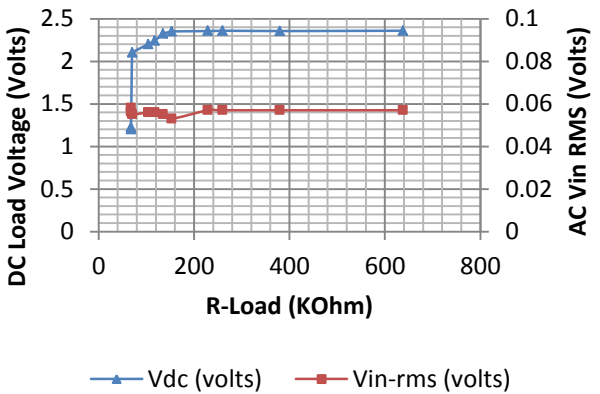
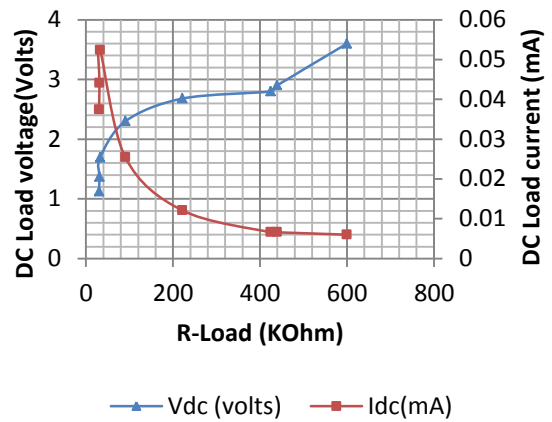
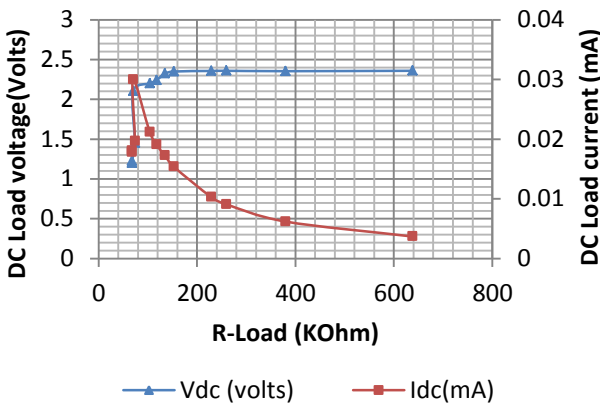
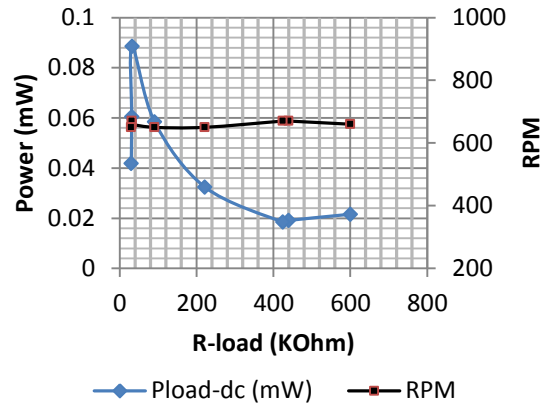
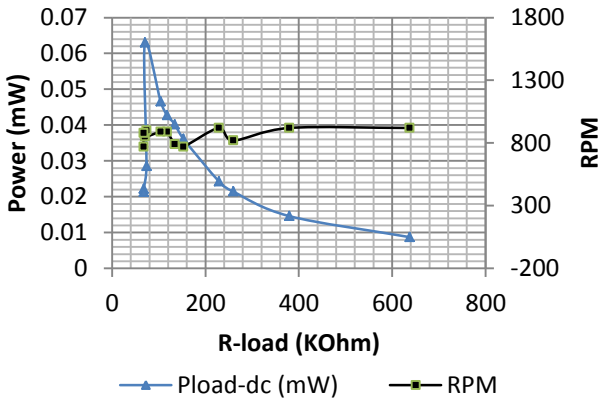


Figure 9.31 OTI-2 (SB) DC power, DC load voltage, DC load current, RPM and rms generator voltage against load resistance, using LTC 3108 supercap (left) and LTC 3108 femto (right)

This work is concluded in the next chapter, where conclusions are drawn based on the findings in the previous chapters. Recommendations for future works are also presented in an attempt to push the present effort forward.

## CHAPTER 10: CONCLUSIONS AND FUTURE WORKS

### 10.1 Introduction

In this work four notched-blade turbines were designed, the LST, MST, OTI-1 and OTI-2 using a CAD program. The MST's flow characteristics were simulated, which led to the design and fabrication of the LST and to the optimization of the OTI-1 and OTI-2. The CAD design was used to fabricate the turbines by 3D printing in ABS. They were then integrated into an energy harvesting and delivery system (EHDS) by coupling each one to a generator whose output voltage was rectified and boosted by a DC to DC converter.

The resulting EHDS was extensively tested by use of three test beds designed to specifically evaluate the system's ability to harvest energy from three separate and distinct fluid flows: Nitrogen, water and simulated blood, the results of which can be found in chapter 9 of this work.

It is important to alert the reader to the circumstances that impinged on the flow and quality of our results as a lessons learned and improvements checklist for those who are interested in continuing furthering this research effort. Many lessons were learned, but in particular four are worthy of consideration at this time:

1. The surface quality, specifically of the inside of the casings of 3D printed models may increase the resistance to the fluid flow when compared to a molded or machined parts with a very smooth finish.
2. The generators used provided high currents at various RPMs, but very little voltage, which decreased their performance at the low RPMs needed for implantation. A

- more appropriate generator can be designed and manufactured for around U.S. \$10,000 or less, greatly improving the performance of the system and decreasing the size of the turbines even more. A well-tuned generator that produces a high voltage and moderate currents at low RPMs would take advantage of high viscosity fluids that provide higher torque at lower speeds.
3. Impedance matching between the generator and the rectifier and DC to DC conversion system needs to be studied more closely to ensure that the turbine is operating at its optimum potential.
  4. Experimentation of blade designs that decrease the resistance between the back of the blade and the fluid even more. New simulations and fabrication are recommended that take into consideration the blade's ability to cut through the fluid as it turns. This will help improve performance even in high viscosity fluids such as water and blood when compared to gases.

## **10.2 LST Conclusions**

The LST was integrated and now is considered the large scale turbine energy harvesting system, LST-EHDS. It demonstrated great potential for applications in harvesting energy from any gas at moderate flow rates of tens of liters per minute. Industrial processes that use gasses such as nitrogen, oxygen, argon, etc. for many fabrication and manufacturing processes can benefit from installing this turbine in their process lines and harvest the flow energy to power internet of things (IoT) devices that can continuously monitor and report wirelessly normal and/or abnormal findings in their environment.

The findings can then be communicated directly to computers that control conveyor belts that carry parts in an assembly line, for example.

The addition of an LST EHDS to any industrial process would increase safety for the workers and provides a mechanism to prevent damage to the machines by stopping the process if a critical finding warrants it.

### **10.3 MST Conclusions**

The MST, just like the LST now becomes the MST-EHDS. This system was tested both with nitrogen gas and water to examine its ability to harvest and deliver power to a circuit. It produced up to 23.4 mW of raw power using nitrogen flow and up to 3 mW using water flow as an energy source. This system can be used to replace many batteries found in a home, office or industrial setting. It has a very small operating volume of 1 mL, requiring small flows and low pressure requirements down 0.2 PSI. It is small enough to be non-obstructing even when supplying power to small systems with limited real estate. It demonstrated a very robust behavior given to the wide blade design with increased flow contact area when compared to the OTI-1 and OTI-2.

### **10.4 OTI-1 Conclusions**

This system once integrated is considered a symbiotic intra-corporeal power source which is a specialized EHDS and is the topic of this dissertation. In this work it was found to provide enough power to source three out five IMDs listed on table 2.2: Most pacemakers and defibrillators which require between 30 and 100  $\mu$ W and some neurological stimulators at 30  $\mu$ W to 2 mW. Of course the high end of these ranges is outside the peak DC power of 71  $\mu$ W found for the OTI-1 at a very low 225 RPM and 468 mL/m flow (see Table 10.1). With some impedance matching this SIPS can go beyond this range now that a rectifier is not being used.

An LTC 3109 DC to DC converter may accept the unrectified input of both the positive and negative half cycles produced by the generator when operating at the low RPMs required for implantation.

Table 10.1 Characterization data of the OTI-1 SIPS using simulated blood flow as a harvesting source

Optimized Turbine for Implantation 1 (OTI-1)								
DC Measurements (2.3 volts) LTC 3108 femto				Simulated blood				
Vdc (volts)	Idc(mA)	Vin-rms (volts)	Freq(Hz)	RPM	R (KΩs)	Pload-dc (mW)	Pd (mmHg)	Q (mL/m)
2.35	0.004	0.092	23	230	587.5	0.0094	36	468
2.35	0.0047	0.092	23	230	500	0.011045	36	468
2.35	0.0049	0.092	23	230	479.5918	0.011515	36	468
2.35	0.0068	0.101	23	230	345.5882	0.01598	36	468
2.35	0.0082	0.092	21	210	286.5854	0.01927	36	468
2.35	0.0124	0.092	23	230	189.5161	0.02914	36	468
2.35	0.0148	0.101	20	200	158.7838	0.03478	36	468
2.35	0.0216	0.092	23	230	108.7963	0.05076	36	468
2.35	0.026	0.101	23	230	90.38462	0.0611	36	468
2.2	0.0324	0.092	23	230	67.90123	<b>0.07128</b>	36	473
1.1	0.101	0.101	19	190	10.89109	0.1111	35	473
0.7	0.0675	0.101	19	190	10.37037	0.04725	35	478
0.44	0.0435	0.101	19	190	10.11494	0.01914	35	483
				<b>225</b>			<b>36</b>	<b>468.5</b>

### 10.5 OTI-2 Conclusions

Due to better impedance matching between the generator and the LTC 3108 DC to DC converters, especially the femto, the OTI-2 SIPS outperformed (88  $\mu$ W) the OTI-1 (71  $\mu$ W) even though it is smaller and has a smaller generator. But it required approximately 650 RPM with a flow of 600 mL/m to operate and caused a drop of 62 mmHg.(see Table 10.2). Ideally, no more than 10% of the blood pressure should be harvested from the circulatory system in order to reduce the potential for hypoperfusion and ischemia distal to the implantation site, that is if the SIPS is connected in series configuration (see chapter 5).



An alternative is to connect the SIPS in a parallel configuration that takes advantage of the great potential pressure difference between an artery and a vein, which can be as much as 120 mmHg during systole (time when the left and right ventricles contract and pump the blood into the aorta and the main pulmonary artery respectively) and 80 mmHg during diastole (time when the ventricles are at rest, receiving blood from the atria).

Table 10.2 Characterization data of the OTI-2 SIPS using simulated blood flow as a harvesting source

OTI-2 13x 3mm notched-turbine rotor								
DC Measurements (3.6 volts) LTC 3108-femto				Simulated Blood				
Vdc (volts)	Idc (mA)	Vin-rms (volts)	Freq (Hz)	RPM	R (KΩs)	Pload-dc (mW)	Pd (mmHg)	Q (mL/m)
3.6	0.006	0.042	66	660	600	0.0216	65	663
2.9	0.007	0.038	67	670	439.3939	0.01914	65	663
2.8	0.007	0.038	67	670	424.2424	0.01848	65	663
2.68	0.012	0.042	65	650	221.4876	0.032428	65	663
2.3	0.025	0.042	65	650	90.55118	0.05842	65	648
1.69	0.052	0.042	66	660	32.25191	<b>0.088556</b>	66	633
1.37	0.044	0.042	67	670	31.06576	0.060417	65	663
1.12	0.037	0.042	65	650	29.94652	0.041888	65	663
				<b>660</b>			<b>65.125</b>	<b>657.375</b>

## 10.6 Materials Conclusions

The ultimate use of a SIPS in an actual commercial application is strictly dependent on the use of materials and procedures that are hemo-compatible.

At this juncture, the implementation of hemo-compatible materials in the current work is limited to making the argument or recommendation for use of a certain process. There are many options for making an IMD hemo-compatible, but three of them are most readily available to the author and have potential for collaboration between research groups at USF and are presented here for consideration:

1. SiC deposition for coating our turbine blade assembly and the inside of the casing by using PECVD in association with the SiC group at USF. This process could trigger a new area of investigation and collaboration for the AMBIR group and can open the doors to many researchers interested in continuing the present effort.
2. The second option is to use the traditional machining process of metals with high quality and high durability mentioned in chapter 5. This process is costly, as we don't have the machinery and expertise to complete that process at USF, so the designs would have to be submitted to a third party for fabrication. The Heartmate II® left ventricular assist device (HM2 VAD), flagged as a system with low thromboembolic risk by [97] uses Ti as a bulk material and then runs it through a process that renders the blood-contacting surface smooth and textured (with Ti microspheres) in different sections of the device to improve its hemo-compatibility.
3. The third option is to make the parts out of a less expensive metal and then coat their surface to comply with the specifications outlined by ISO 14708-1:2014 as they apply to IMDs. This process is highly beneficial to our research group as a means to study the deposition of hemo-compatible coatings such as the diamond like coating (DLC) using ion beam sputtering (IBS) which has demonstrated improved compatibility over TiN[98]. This last option has a lot of merit as a research avenue, but requires the acquisition of new equipment that can provide years of investigation potential for the AMBIR lab.

Only those materials and procedures that are strictly necessary for proof of concept were utilized in this work, such as PMMA and ABS. Although they are biocompatible, they are minimally hemo-compatible and thus not sufficient to conclude that our system is ready for in-

vivo investigations. The research objectives presented in chapter 1 are revisited in the next section to clarify their interpretations in light of the findings in chapter 9.

## 10.7 Research Objectives Conclusions

In section 1.2 it was stated that the objective of this research was to miniaturize the NTEG originally developed by [28] at USF's AMBIR group, down to an implantable size that could power most common low power IMDs such as a pacemakers or defibrillators without the need for a battery. This established a maximum power need of 10 mW as the high end of our goal (Table 2.1). But this goal was set assuming that a dual generator system with 6 phases operating simultaneously could be implemented and furthermore, that the results of a single phase could be multiplied by 6. This is still possible if each phase is connected to a transformer as found in chapter 2, but a system like that would be too large to implement as an implantable medical device unless smaller, high voltage generators were used. It is possible though to use such a device as an extracorporeal energy harvesting system using the current generators capable of producing 10mW of power for IoT applications.

The goal of creating a SIPS is still possible by implementing two phases in series. This approach produced very good results comparable to the battery of many IMDs implanted up to now.

One of the most commonly implanted IMDs is the pacemaker, with average size of 48x43x7 cubic mm or 14.57 cc [99], compared to size of the generators in this work, 1.49 cc (MST), 7.83 cc (OTI-1) and 3.25 cc (OTI-2), with an average of 4.2 cc, which is well below half the size of a typical pacemaker. And since half of the real estate of a pacemaker is taken by its battery, these generators have a higher power density than the typical pacemaker's lithium ion battery.

The claims of section 1.2 and Table 2.1 (10 mW) therefore were achieved when looking at the performance of the MST in water, since the claim was based on the performance measurements in water obtained by [28].

The fourth row of Table 3.1 appears bolded to indicate the goal that was set to achieve, powering most IMDs by staying around 2,000 RPM. It can be seen that at 2000 RPM the power produced by 2 coils taken in series is 5.44 mW, while the power of a single coil is 2.728 (half as much). Figure 9.15 shows this achievement, 3 mW, or 1.6 mW per phase with a slight increase in RPM for a total of 10 mW when a dual coil system with 6 phases is used. This is of course a calculation, and only empirical data from an experiment can prove these hypotheses as the discussion moves to the future works section of this work. It was important to the author that every avenue of possibilities be explored as it pertains to the potential application of these turbine systems, so the research did not conclude with the miniaturization that produced the MST, rather it continued to the development of the OTI-1 and OTI-2 which produced very good results not only for implantation, but for extra-corporeal applications as well.

It is hereby concluded that the stated goals were achieved and a baseline for comparison was established for future research. See Table 10.3 below for a summary of power density in mW/cc of the four turbines evaluated in chapter 8.

In this section various ideas are presented to show how the SIPS can be used and improved upon to meet the power needs of an ever increasing number of IMDs with increased capabilities. The use of the SIPS in areas not demonstrated in this work are vast and very diverse, but need to be explored so that those interested in bio-energy harvesting systems can continue this research and make it an increasingly exciting field of investigation.

Table 10.3 Peak power density for LTS, MST, OTI-1 and OTI-2 turbines in mW/cc

Turbines		Nitrogen		Water		Simulated Blood	
Model	Volume (cc)	Peak Power (mW)	Power Density (mW/cc)	Peak Power (mW)	Power Density (mW/cc)	Peak Power (mW)	Power Density (mW/cc)
LST	49.00	80.00	1.63				
MST	1.49	23.40	<b>15.70</b>	3.00	0.13		
OTI-1	7.83	<b>120.00</b>	15.33	<b>5.25</b>	0.67	<b>1.06</b>	0.13
OTI-2	3.25	15.76	4.85	2.84	0.87	0.50	0.15

## 10.8 Future Works

The future looks bright for energy harvesting both inside and outside of the human body. The time has come to stop envisioning what is to come and start implementing what we know is needed to make it a reality.

The energy harvesting systems presented in this work have shown to be quite adaptable and versatile in extracting energy from flow in any environment and taking them to the next level will necessitate a conscious effort to use all of the coils at the same time by implementing a dual generator system in which both generators are driven by a single turbine.

This system has the potential of driving 6 devices at the same time, where the output of from each coil is connected to a different circuit.

Another option is to use a six diode configuration discussed in chapter 2, where 3 phases per generator are rectified and stored in a capacitor. This approach would apply mainly to IoT networks, with the single generator approach being reserved for intra-corporeal use to replace the battery of an IMD. Two considerations that take advantage of this approach are considered below.

### **10.8.1 Emergency Notification System**

The use of the SIPS as a power source allows for the use of multiple modules, one of which can be dedicated to monitoring the event of a heart attack.

Although implantable defibrillators use this technology, other system can also use it to ensure prompt notification and treatment. In the event of a heart attack, the SIPS would stop generating power and the IMD would not function as intended.

The SIPS can be modified to maintain sufficient charge in a supercapacitor (as seen with the LTC 3108 supercap) to transmit a distress signal understood by any nearby cellphone, which would automatically dial 911 and transmit the patient's identification, condition and GPS coordinates to the emergency response system. An implantable rectenna may be used to communicate with its environment immediately outside of the body. This system can be achieved by tuning and enhancing the RF energy harvesting system presented by Pérez and Ababneh in [66].

### **10.8.2 Thrombus Detection System**

The development of a thrombus (blood clot) is a dangerous event that could potentially occur with any post-operative patients due to reduced activity or patients with poor circulation or even with high potassium which contributes to the thickening of the blood. Often a clot is formed in the deep veins of the legs and is called deep vein thrombosis (DVT). If the clot dislodges from the walls of the veins (usually near a valve) it is called an embolus, which is more threatening to the patient because it is now able to travel in the circulatory system and obstruct the flow of blood to distant tissues and organs which will starve for nutrients and oxygen as a consequence.

It is then imperative that a quick diagnosis be made concerning a patient with a thrombus so that clot-busting drugs can be administered promptly before the thrombus becomes an embolus. The development of a blood clot is an event that produces an increase in D-dimer, a blood marker of endogenous fibrinolysis detectable in patients with DVT[62].

If the proposed generator is made of a biocompatible non-thrombogenic material that is coated with a blood repellent[5], a patient with a SIPS has the advantage that the SIPS can power a D-dimer LOC (lab on a chip) that will quickly detect whether the patient has developed a thrombus. This information can be sent wirelessly to the patient's cell phone which would dial 911 and report the D-dimer test results and the person's location, giving the doctor enough time to save the patient's life by administering the necessary drugs. This capability can be investigated and implemented as one of many future works areas that stem from the current research effort.

## REFERENCES

- [1] E. A. Finkelstein, J. G. Trogon, J. W. Cohen, and W. Dietz, “Annual Medical Spending Attributable To Obesity: Payer-And Service-Specific Estimates,” *Health Aff. (Millwood)*, vol. 28, no. 5, pp. w822–w831, Sep. 2009.
- [2] C. L. Ogden, M. D. Carroll, B. K. Kit, and K. M. Flegal, “Prevalence of Childhood and Adult Obesity in the United States, 2011-2012,” *JAMA*, vol. 311, no. 8, p. 806, Feb. 2014.
- [3] S. Gollakota, H. Hassanieh, B. Ransford, D. Katabi, and K. Fu, “They Can Hear Your Heartbeats: Non-invasive Security for Implantable Medical Devices,” in *Proceedings of the ACM SIGCOMM 2011 Conference*, New York, NY, USA, 2011, pp. 2–13.
- [4] J. W. Smith, C. Thorne, W. C. Grabb, and R. W. Beasley, *Grabb and Smith’s plastic surgery*. Lippincott Williams & Wilkins, 2007.
- [5] D. C. Leslie, A. Waterhouse, J. B. Berthet, T. M. Valentin, A. L. Watters, A. Jain, P. Kim, B. D. Hatton, A. Nedder, K. Donovan, E. H. Super, C. Howell, C. P. Johnson, T. L. Vu, D. E. Bolgen, S. Rifai, A. R. Hansen, M. Aizenberg, M. Super, J. Aizenberg, and D. E. Ingber, “A bioinspired omniphobic surface coating on medical devices prevents thrombosis and biofouling,” *Nat. Biotechnol.*, vol. 32, no. 11, pp. 1134–1140, Nov. 2014.
- [6] H. Cabra, S. Thomas, and S. Pérez, “‘Design, Mathematical Model, and Simulation of a Novel Mini Notched Impulse Turbine’ - Submitted,” *IEEE Trans. Power Syst.*
- [7] M. Jonsson, A. Zurbuchen, A. Haeberlin, A. Pfenniger, and R. Vogel, “Vascular Turbine Powering a Cardiac Pacemaker: an In-vivo Case Study,” 2014.
- [8] Y. Yang, X.-J. Wei, and J. Liu, “Suitability of a thermoelectric power generator for implantable medical electronic devices,” *J. Phys. Appl. Phys.*, vol. 40, no. 18, p. 5790, 2007.
- [9] G. Wang, W. Liu, M. Sivaprakasam, and G. A. Kendir, “Design and analysis of an adaptive transcutaneous power telemetry for biomedical implants,” *IEEE Trans. Circuits Syst. Regul. Pap.*, vol. 52, no. 10, pp. 2109–2117, Oct. 2005.
- [10] S. Priya and D. J. Inman, *Energy harvesting technologies*, vol. 21. Springer, 2009.



- [11] J. A. Paradiso and T. Starner, "Energy scavenging for mobile and wireless electronics," *Pervasive Comput. IEEE*, vol. 4, no. 1, pp. 18–27, 2005.
- [12] E. V. Potapov, M. Loebe, B. A. Nasser, H. Sinawski, A. Koster, H. Kuppe, G. P. Noon, M. E. DeBakey, and R. Hetzer, "Pulsatile Flow in Patients With a Novel Nonpulsatile Implantable Ventricular Assist Device," *Circulation*, vol. 102, no. suppl 3, pp. Iii–183–Iii–187, Nov. 2000.
- [13] S. Klotz, B. Meyns, A. Simon, T. Wittwer, P. Rahmanian, C. Schlensak, T. T. Tjan, H. H. Scheld, and D. Burkhoff, "Partial mechanical long-term support with the CircuLite Synergy pump as bridge-to-transplant in congestive heart failure," *Thorac Cardiovasc Surg*, vol. 58, no. Suppl 2, pp. S173–S178, 2010.
- [14] S. Agarwal and K. M. High, "Newer-generation ventricular assist devices," *Best Pract. Res. Clin. Anaesthesiol.*, vol. 26, no. 2, pp. 117–130, Jun. 2012.
- [15] <http://www.mdtmag.com/article/2014/10/energy-harvesting-ics-power-electric-body> [MDT, "Energy Harvesting ICs Power the Electric Body", October 7,-2015].
- [16] Tuttle, Todd M., et al. "Increasing use of contralateral prophylactic mastectomy for breast cancer patients: a trend toward more aggressive surgical treatment." *Journal of Clinical Oncology* 25.33 (2007): 5203-5209.
- [17] "Blood Marker Tests," *Breastcancer.org*. [Online]. Available: [http://www.breastcancer.org/symptoms/testing/types/blood\\_marker](http://www.breastcancer.org/symptoms/testing/types/blood_marker). [Accessed: 11-Jan-2015].
- [18] <http://www.medicalnewstoday.com/articles/257898.php>, [*Medical News Today* "Tiny Lab' Implanted Under Skin Transmits Blood Marker Levels", January 23, 2015].
- [19] "Energy Harvesting ICs Power the Electric Body," *Medical Design Technology*. [Online]. Available: <http://www.mdtmag.com/articles/2014/10/energy-harvesting-ics-power-electric-body>. [Accessed: 01-Jan-2015].
- [20] M. J. Ramsay and W. W. Clark, "Piezoelectric energy harvesting for bio-MEMS applications," 2001, vol. 4332, pp. 429–438.
- [21] A. Harb, "Energy harvesting: State-of-the-art," *Renew. Energy*, vol. 36, no. 10, pp. 2641–2654, Oct. 2011.
- [22] D. C. Bock, A. C. Marschilok, K. J. Takeuchi, and E. S. Takeuchi, "Batteries used to power implantable biomedical devices," *Electrochimica Acta*, vol. 84, pp. 155–164, Dec. 2012.

- [23] "ICD Manufacturers Must Increase Battery Life to Cut Costs, Improve Care," *DI Cardiology*. [Online]. Available: <http://www.dicardiology.com/article/icd-manufacturers-must-increase-battery-life-cut-costs-improve-care>. [Accessed: 9-Jul-14].
- [24] U.S. Environmental Protection Agency, "Proceedings Of Public Hearings: Plutonium And The Other Transuranium Elements Volume III Additional Materials Received (3-73)", 1975
- [25] D. A. McIntyre, "The Eleven Most Implanted Medical Devices In America," *247wallst.com*, 19-Jul-2011. [Online]. Available: <http://247wallst.com/healthcare-economy/2011/07/18/the-eleven-most-implanted-medical-devices-in-america/>. [Jul7, '14].
- [26] "ICD Manufacturers Must Increase Battery Life to Cut Costs, Improve Care," *DI Cardiology*. [Online]. Available: <http://www.dicardiology.com/article/icd-manufacturers-must-increase-battery-life-cut-costs-improve-care>. [Accessed: 9-Jul-14].
- [27] J. Kymissis, C. Kendall, J. Paradiso, and N. Gershenfeld, "Parasitic power harvesting in shoes," in *Second International Symposium on Wearable Computers, 1998. Digest of Papers*, 1998, pp. 132–139.
- [28] H. Cabra, "Design, Simulation, Prototype, and Testing of a Notched Blade Energy Generation System," *Grad. Theses Diss.*, May 2014.
- [29] S. R. Platt, S. Farritor, K. Garvin, and H. Haider, "The use of piezoelectric ceramics for electric power generation within orthopedic implants," *IEEEASME Trans. Mechatron.*, vol. 10, no. 4, pp. 455–461, Aug. 2005.
- [30] P. Miao, P.D. Mitcheson, A.S. Holmes, E.M. Yeatman, T.C. Green, and B.H. Stark, "Mems inertial power generators for biomedical applications," *Microsyst Technol*, vol. 12, pp. 1079–1083, 2006.
- [31] R. Amirtharajah and A. P. Chandrakasan, "Self-powered signal processing using vibration-based power generation," *Solid-State Circuits IEEE J. Of*, vol. 33, no. 5, pp. 687–695,
- [32] H. Goto, D. T. Sugiura, Y. Harada, and T. Kazui, "Feasibility of using the automatic generating system for quartz watches as a leadless pacemaker power source," *Med. Biol. Eng. Comput.*, vol. 37, no. 3, pp. 377–380, May 1999.
- [33] Savoie, Richard, and Gary Searle. "Medical device having capacitive coupling communication and energy harvesting." U.S. Patent No. 8,939,928. 27 Jan. 2015.
- [34] K. Goto, T. Nakagawa, O. Nakamura, and S. Kawata, "An implantable power supply with an optically rechargeable lithium battery," *Biomed. Eng. IEEE Trans. On*, vol. 48, no. 7, pp. 830–833, 2001.

- [35] Y. Zhu, S. O. R. Moheimani, and M. R. Yuce, "Ultrasonic Energy Transmission and Conversion Using a 2-D MEMS Resonator," *IEEE Electron Device Lett.*, vol. 31, no. 4, pp. 374–376, Apr. 2010.
- [36] Bert Lenaerts and Robert Puers, "An inductive power link for a wireless endoscope," *Biosens. Electron.*, no. 22, pp. 1390–1395, 2007.
- [37] J.A. Paradiso, T. Starner, "Energy scavenging for mobile and wireless electronics," *IEEE Pervasive Computing*, Vol.4, Issue 1, pp.18-27, 2005
- [38] S. Am and H. Nh, "Human red blood cell hemolysis in a turbulent shear flow: contribution of Reynolds shear stresses.," *Biorheology*, vol. 21, no. 6, pp. 783–797, Dec. 1983.
- [39] X. Wei and J. Liu, "Power sources and electrical recharging strategies for implantable medical devices," *Front. Energy Power Eng. China*, vol. 2, no. 1, pp. 1–13, 2008.
- [40] "8-pole magnetic ring, 12 slot stator," *Daido Electronics*. [Online]. Available: [http://www.daido-electronics.co.jp/english/analysis/magnetic\\_field/images/image01.png](http://www.daido-electronics.co.jp/english/analysis/magnetic_field/images/image01.png).
- [41] W. R. Douglas, "Of pigs and men and research," *Space Life Sci.*, vol. 3, no. 3, pp. 226–234, Jun. 1972.
- [42] Wilson, N., et al. "Normal intracardiac and great artery blood velocity measurements by pulsed Doppler echocardiography." *Heart* 53.4 (1985): 451-458.
- [43] A. S. Manolis and T. A. Manolis, "Totally Implantable Artificial Heart: Still a Major Challenge," *Hosp. Chron.*, vol. 9, no. 1 Sup, pp. 60–62, May 2014.
- [44] "Tesla polyphase induction motors : Ac Motors - Electronics Textbook," *All About Circuits*. [Online]. Available: [http://www.allaboutcircuits.com/vol\\_2/chpt\\_13/7.html](http://www.allaboutcircuits.com/vol_2/chpt_13/7.html). [Accessed: 19-Jan-2015].
- [45] T. R. Kuphaldt, *Lessons In Electric Circuits, Volume II – AC*, 6th ed., vol. 2, 6 vols.
- [46] "INDUCTION MOTORS: ROTATING FIELD, SLIP and TORQUE (part 2)," *Industrial Electronics Information for Manufacturing Applications*. [Online]. Available: [http://www.industrial-electronics.com/Electric-Motors-Drives\\_5b.html#sthash.FeQ7gM3T.dpuf](http://www.industrial-electronics.com/Electric-Motors-Drives_5b.html#sthash.FeQ7gM3T.dpuf).
- [47] W. Storr, "Full Wave Rectifier and Bridge Rectifier Theory," *Basic Electronics Tutorials*. [Online]. Available: [http://www.electronics-tutorials.ws/diode/diode\\_6.html](http://www.electronics-tutorials.ws/diode/diode_6.html). [Accessed: 19-Jan-2015].

- [48] “Rectifier circuits : Diodes And Rectifiers - Electronics Textbook,” *All About Circuits*. [Online]. Available: [http://www.allaboutcircuits.com/vol\\_3/chpt\\_3/4.html](http://www.allaboutcircuits.com/vol_3/chpt_3/4.html). [Accessed: 19-Jan-2015].
- [49] Y. Yang, G. Dong Xu, and J. Liu, “A Prototype of an Implantable Thermoelectric Generator for Permanent Power Supply to Body Inside a Medical Device,” *J. Med. Devices*, vol. 8, no. 1, pp. 014507–014507, Dec. 2013.
- [50] C. Peters, J. Handwerker, D. Maurath, and Y. Manoli, “An ultra-low-voltage active rectifier for energy harvesting applications,” in *Circuits and Systems (ISCAS), Proceedings of 2010 IEEE International Symposium on*, 2010, pp. 889–892.
- [51] W. Nichols, M. O’Rourke, and C. Vlachopoulos, *McDonald’s blood flow in arteries: theoretical, experimental and clinical principles*. CRC Press, 2011.
- [52] “Bernoulli Equation.” [Online]. Available: <http://hydrogen.physik.uni-wuppertal.de/hyperphysics/hyperphysics/hbase/pber.html>.
- [53] Richard E. Klabunde, *Cardiovascular Physiology Concepts*, Second. Lippincott Williams & Wilkins, 2011.
- [54] W. B. Lo and H. Ellis, “The Circle Before Willis: A Historical Account of the Intracranial Anastomosis,” *Neurosurgery*, vol. 66, no. 1, pp. 7–18, Jan. 2010.
- [55] Study Blue, “Arteries and Veins”, [Online]. Available: <https://s3.amazonaws.com/classconnection/84/flashcards/7928084/jpg/veins-arteries-14CC9D6E1881216A64A-thumb400.jpg>
- [56] “Implantable Pulse Generators ‘Stimulate’ Medical Device Industry,” *Medical Design Technology*. [Online]. Available: <http://www.mdtmag.com/articles/2012/01/implantable-pulse-generators-%E2%80%98stimulate%E2%80%99-medical-device-industry>. [Accessed: 07-Jul-14].
- [57] M. J. Brescia, J. E. Cimino, K. Appel, and B. J. Hurwicz, “Chronic Hemodialysis Using Venipuncture and a Surgically Created Arteriovenous Fistula,” *N. Engl. J. Med.*, vol. 275, no. 20, pp. 1089–1092, Nov. 1966
- [58] “Coronary anastomosis,” *TheFreeDictionary.com*. [Online]. Available: <http://medical-dictionary.thefreedictionary.com/Coronary+anastomosis>. [Accessed: 19-Jan-15].
- [59] Mayo Clinic, “Riverside.” [Online]. Available: [http://www.riversideonline.com/health\\_reference/Bladder-Kidney/DA00078.cfm?RenderForPrint=1](http://www.riversideonline.com/health_reference/Bladder-Kidney/DA00078.cfm?RenderForPrint=1). [Accessed: 19-Jan-2015].

- [60] H. B. Bittner, J. Garbade, S. Lehmann, M. J. Barten, and F. W. Mohr, "Extra-Corporeal Membrane Oxygenation Support in Cardiac Transplantation," *J. Heart Lung Transplant.*, vol. 32, no. 4, pp. S257–S257, 2013.
- [61] R. G. Carroll, "CARDIOVASCULAR PRESSURE-FLOW RELATIONSHIPS: WHAT SHOULD BE TAUGHT?," *Adv. Physiol. Educ.*, vol. 25, no. 2, pp. 8–14, Jun. 2001.
- [62] P. S. Wells, D. R. Anderson, M. Rodger, M. Forgie, C. Kearon, J. Dreyer, G. Kovacs, M. Mitchell, B. Lewandowski, and M. J. Kovacs, "Evaluation of D-Dimer in the Diagnosis of Suspected Deep-Vein Thrombosis," *N. Engl. J. Med.*, vol. 349, no. 13, pp. 1227–1235, Sep. 2003.
- [63] Henry Cabra and S. Thomas, "Design, Simulation and Prototyping Model of a Miniaturized Bio Energy Generation System," *Technical Proceeding of the 22nd IASTED International Symposia on Modeling and Simulation*, MS, 2011.
- [64] H. Cabra and S. W. Thomas, "Fabrication of cross flow bio microturbine", [http://cap.ee.imperial.ac.uk/~pdm97/powermems/2010/posterpdfs/183\\_Cabra\\_158.pdf](http://cap.ee.imperial.ac.uk/~pdm97/powermems/2010/posterpdfs/183_Cabra_158.pdf)
- [65] Majdi M. Ababneh, Samuel Pérez, Henry Cabra, and Sylvia Thomas," Design of A Novel Mini Notched Turbine With Optimized Power Management Circuit," *The 8th international Renewable Energy Congress*, March 2017
- [66] Majdi M. Ababneh, Samuel Pérez, and Sylvia Thomas, "Optimized Power Management Circuit for Implantable Rectenna for In-Body Medical Devices," *The 12th IEEE international conference on Power Electronics and Drive Systems*, December 2017
- [67] Song, Kwangsun, et al. "Subdermal flexible solar cell arrays for powering medical electronic implants." *Advanced healthcare materials* 5.13 (2016): 1572-1580.
- [68] "Life is Easy with IoT", IoThought. [Online]. Available: <http://iothought.com/wearables-of-internet-of-medical-things> [ Accessed: March 4, 2015]
- [69] "WHAT IS CNC MACHINING? AN OVERVIEW OF THE CNC MACHINING PROCESS.", Astro Machine. [Online] Available: <http://astromachineworks.com/what-is-cnc-machining/> [Accessed: March 4, 2015]
- [70] "What is 3D Printing? The definitive guide to additive manufacturing", [Online]. Available: <https://www.3dhubs.com/what-is-3d-printing#materials> [Accessed: 19-Jan-2015]
- [71] "Material properties and fabrication parameters in selective laser sintering process", [Ian Gibson, Dongping Shi, , *Rapid Prototyping Journal*, Vol. 3 Issue: 4, pp.129-136, 1997] [Online]. Available: <http://www.emeraldinsight.com/doi/full/10.1108/13552549710191836> [Accessed: Match 5, 2018]

- [72] “CNC MACHINING VS SLA AND SLS”, Steve, WayKen [Online]. Available: <https://www.waykenrm.com/cnc-machining-vs-sla-and-sls.html> [Accessed: Nov 8, 2017]
- [73] “Vacuum Casting”, AFS and The Institute [Online]. Available: <http://www.afsinc.org/content.cfm?ItemNumber=6911> [Accessed: March, 17, 2018]
- [74] “Mass Production of Medical Devices by Metal Injection Molding”, MD+DI, John L. Johnson. [Online]. Available: <http://www.mdonline.com/mass=production-medical-devices-metal-injection-molding> [Accessed: March 21, 2018]
- [75] “Lessons In Electric Circuits”, Tony R. Kuphaldt, under the terms and conditions of the Design Science License, copyright (C) 2000-2010, Nov. 2015 [Online]. Available: [http://www.malayalam.net/howto/LessonsInElectricCircuits/AC/AC\\_13.html](http://www.malayalam.net/howto/LessonsInElectricCircuits/AC/AC_13.html) [Accessed: 20 Jan 2015]
- [76] “Bernoulli Equation”, Hyperphysics. [Online]. Available: <http://hydrogen.physik.uni-wuppertal.de/hyperphysics/hyperphysics/hbase/pber.html> [Accessed: Nov 2, 2017]
- [77] Elaine N. Marieb, Benjamin Cummings Human Anatomy and Physiology, Sixth Ed., Pearson, 2004. (Power Point Slides)
- [78] Jonathan Daniels, “A V Fistula graft” [Online]. Available: [https://www.youtube.com/watch?v=6I\\_gzfPFW1U](https://www.youtube.com/watch?v=6I_gzfPFW1U) [Accessed: 22 Dec 2017]
- [79] “Red blood cells (erythrocytes)”, Encyclopedia Britannica. [Online]. Available: <https://www.britannica.com/science/red-blood-cell> [Accessed: June 4, 2017]
- [80] “High shear stress can initiate both platelet aggregation and shedding of procoagulant containing microparticles”, Y. Miyazaki, S. Nomura, T. Miyake, H. Kagawa, C. Kitada, H. Taniguchi, Y. Komiyama, Y. Fujimura, Y. Ikeda, S. Fukuhara, , Vol. 88, No. 9, pp. 3456–3464, 1996. [Online]. Available: <https://www.ncbi.nlm.nih.gov/pubmed/8896411> [Accessed: May 9, 2016]
- [81] [81]“Platelet Activation: The Mechanisms and Potential Biomarkers”, Seong-Hoon Yun, Eun-Hye Sim, Ri-Young Goh, Joo-In Park, and Jin-Yeong Han, , [Online]. Available: <https://www.hindawi.com/journals/bmri/2016/9060143/> [Accessed: March 2016]
- [82] “High shear stress can initiate both platelet aggregation and shedding of procoagulant containing microparticles”, Y. Miyazaki, S. Nomura, T. Miyake, H. Kagawa, C. Kitada, H. Taniguchi, Y. Komiyama, Y. Fujimura, Y. Ikeda, S. Fukuhara, , Vol. 88, No. 9, pp. 3456–3464, 1996. [Online]. Available: <https://www.ncbi.nlm.nih.gov/pubmed/8896411> [Accessed: 5-Jan-16]

- [83] Mihov, D., and B. Katerska. "Some biocompatible materials used in medical practice." *Trakia Journal of Sciences* 8.2 (2010): 119-125.
- [84] Rajagopalan, T., et al. "Low temperature deposition of nanocrystalline silicon carbide films by plasma enhanced chemical vapor deposition and their structural and optical characterization." *Journal of Applied Physics* 94.8 (2003): 5252-5260.
- [85] Register, Joseph J., *SiC for advanced biological applications*. University of South Florida, 2014.
- [86] Caglar, Veli, et al. "Study of volume, weight and size of normal pancreas, spleen and kidney in adults autopsies." *Forensic Medicine and Anatomy Research* 2.03 (2014): 63.
- [87] "Zortrax 3D Printed Artificial Heart", All3DP. [Online]. Available: <https://all3dp.com/zortrax-3d-printed-artificial-heart/> [Accessed: 10 February, 2017]
- [88] Dodziuk, Helena. 2016. "Applications of 3D printing in healthcare". *Kardiochirurgia i Torakochirurgia Polska/Polish Journal of Thoracic and Cardiovascular Surgery* 13 (3): 283-293. doi:10.5114/kitp.2016.62625
- [89] "A quarterly letter of the Instrumentation Testing Association", ITA News. [Online]. Available: [http://www.instrument.org/enews/2010/Spring2010/ITAEnewsSpring2010\\_files/Page435.htm](http://www.instrument.org/enews/2010/Spring2010/ITAEnewsSpring2010_files/Page435.htm) [Accessed: March 13, 2018]
- [90] Makid Y. Yousif, "Deriving a Blood-Mimicking Fluid for Particle Image Velocimetry in Sylgard-184 Vascular Models", 31<sup>st</sup> Annual International Conference of the IEE EMBS Minneapolis, Minnesota, USA, September 2-5-6, 2009.
- [91] N. Antonova, E. Zvetkova, I. Ivanov and Y. Savov, "Hemorheological changes and characteristic parameters derived from whole blood viscometry in chronic heroin addicts", *Clinical Hemorheology and Microcirculation* , vol 39, pp. 53-61, 2008.
- [92] Mao, Song Shou, et al. "Normal thoracic aorta diameter on cardiac computed tomography in healthy asymptomatic adults: impact of age and gender." *Academic radiology* 15.7 (2008): 827-834.
- [93] Mohiaddin, RAAD H., DAVID N. Firmin, and DONALD B. Longmore. "Age-related changes of human aortic flow wave velocity measured noninvasively by magnetic resonance imaging." *Journal of Applied Physiology* 74.1 (1993): 492-497.
- [94] Haeberlin, Andreas, et al. "The first batteryless, solar-powered cardiac pacemaker." *Heart rhythm* 12.6 (2015): 1317-1323.

- [95] Instruments, Texas. "bq25504-Ultra Low Power Boost Converter with Battery Management for Energy Harvester Applications Datasheet." *Rev A* (2012).
- [96] "LTC 3108 –Data sheet", Technologies, Linear. [Online]. Available: <http://cds.linear.com/docs/en/datasheet/3108fc.pdf> [Accessed: Mar 25, 2018]
- [97] John, Ranjit, et al. "Low thromboembolic risk for patients with the Heartmate II left ventricular assist device." *The Journal of thoracic and cardiovascular surgery* 136.5 (2008): 1318-1323.
- [98] Sin, Dong-Choon, Ho-Lun Kei, and Xigeng Miao. ", Surface coatings for ventricular assist devices.", *Coatings for Biomedical Applications*. 2012. 264-283.
- [99] Mallela, Venkateswara Sarma, V. Ilankumaran, and N. Srinivasa Rao. "Trends in cardiac pacemaker batteries." *Indian pacing and electrophysiology journal* 4.4 (2004): 201.10.8
- [100] Hannan, Mahammad A., et al. "Energy harvesting for the implantable biomedical devices: issues and challenges." *Biomedical engineering online* 13.1 (2014): 79.
- [101] Wang, Bob, Aiguo Patrick Hu, and David Budgett. "Maintaining middle zero voltage switching operation of parallel–parallel tuned wireless power transfer system under bifurcation." *IET Power Electronics* 7.1 (2014): 78-84.
- [102] Bocan, Kara N., and Ervin Sejdić. "Adaptive transcutaneous power transfer to implantable devices: A state of the art review." *Sensors* 16.3 (2016): 393
- [103] [102] Grabowski, Sandra Reynolds, and Gerard J. Tortora. *Principles of anatomy and physiology*. Wiley, 2000.
- [104] "Dual Surface Mount Schottky Barrier Diode SDM40E20L/s/c/a datasheet", Diodes Incorporated [Online] Available: <https://www.diodes.com/assets/Datasheets/ds30298.pdf>, [Accessed: Feb 27, 2018]
- [105] Yousif, Majid Y., David W. Holdsworth, and Tamie L. Poepping. "Deriving a blood-mimicking fluid for particle image velocimetry in sylgard-184 vascular models." *Engineering in Medicine and Biology Society, 2009. EMBC 2009. Annual International Conference of the IEEE*. IEEE, 2009.






## APPENDICES


## Appendix A: Copyright Notices

The following notice is for the material in Chapter 7, 8 and 9.

Rightslink® by Copyright Clearance Center - Google Chrome

Secure | <https://s100.copyright.com/AppDispatchServlet#formTop>

 **Copyright Clearance Center**  [Home](#) [Account Info](#) [Help](#) 

 **IEEE**  
Requesting permission to reuse content from an IEEE publication

**Title:** Design of a novel mini notched turbine with optimized power management circuit

**Conference Proceedings:** Renewable Energy Congress (IREC), 2017 8th International

**Author:** Majdi M. Ababneh

**Publisher:** IEEE

**Date:** March 2017

Copyright © 2017, IEEE

Logged in as:  
Samuel Perez  
University of South Florida

[LOGOUT](#)

### Thesis / Dissertation Reuse

**The IEEE does not require individuals working on a thesis to obtain a formal reuse license, however, you may print out this statement to be used as a permission grant:**

*Requirements to be followed when using any portion (e.g., figure, graph, table, or textual material) of an IEEE copyrighted paper in a thesis:*

- 1) In the case of textual material (e.g., using short quotes or referring to the work within these papers) users must give full credit to the original source (author, paper, publication) followed by the IEEE copyright line © 2011 IEEE.
- 2) In the case of illustrations or tabular material, we require that the copyright line © [Year of original publication] IEEE appear prominently with each reprinted figure and/or table.
- 3) If a substantial portion of the original paper is to be used, and if you are not the senior author, also obtain the senior author's approval.

*Requirements to be followed when using an entire IEEE copyrighted paper in a thesis:*

- 1) The following IEEE copyright/ credit notice should be placed prominently in the references: © [year of original publication] IEEE. Reprinted, with permission, from [author names, paper title, IEEE publication title, and month/year of publication]
- 2) Only the accepted version of an IEEE copyrighted paper can be used when posting the paper or your thesis on-line.
- 3) In placing the thesis on the author's university website, please display the following message in a prominent place on the website: In reference to IEEE copyrighted material which is used with permission in this thesis, the IEEE does not endorse any of [university/educational entity's name goes here]'s products or services. Internal or personal use of this material is permitted. If interested in reprinting/republishing IEEE copyrighted material for advertising or promotional purposes or for creating new collective works for resale or redistribution, please go to [http://www.ieee.org/publications\\_standards/publications/rights/rights\\_link.html](http://www.ieee.org/publications_standards/publications/rights/rights_link.html) to learn how to obtain a License from RightsLink.

If applicable, University Microfilms and/or ProQuest Library, or the Archives of Canada may supply single copies of the dissertation.

[BACK](#)

[CLOSE WINDOW](#)

## Appendix B: Glossary of Terms

SIPS	Symbiotic Intra-corporeal Power Source
NTEG	Notched Turbine Energy Generator
PSAC	Power Source and Conditioning
IMD	Implantable Medical Device
VAD	Ventricular Assist Device
MPPT	Maximum Power Point Tracking
$v_{\text{-noz}}$	Nozzle velocity
$P_{\text{flow}}$	Power from flow of gas or fluid
$W$	Work
$m'$	Mass Flow Rate
$v'$	Volumetric Flow Rate
$\rho$	Fluid Density in $\text{kg/m}^3$
$P_R$	Mechanical Rotor Power
$I_D$	Diode Current
PE	Peak Efficiency
CCE	Center of Curve Efficiency
$Q$	Flow in $\text{m}^3/\text{s}$
SiC	Silicon Carbide
$P_d$	Pressure Difference
$P_{\text{in}}$	Pressure at the inlet
$P_{\text{out}}$	Pressure at the Outlet
$f$	Operating Frequency,

RPM	Revolutions per Minute
$R_L$	Load Resistance
MEMS	Microelectromechanical Systems
IoT	Internet of Things
PCPTM	Personalized Continuous Preventive Telemedicine
MST	Miniaturized Scale Turbine
LST	Large Scale Turbine
OTI-1	Optimized Turbine for Implantation 1
OTI-2	Optimized Turbine for Implantation 2
UHMWPE	Ultra-high Molecular Weight Polyethylene
PMMA	Polymethylmethacrylate
ABS	Acrylonitrile Butadiene Styrene
PLA	Polylactic Acid

## ABOUT THE AUTHOR

Samuel Pérez Minaya is a retired U.S. Air Force (USAF) MSgt who immigrated to the United States from the Dominican Republic in January 1988. He joined the USAF the same year and completed his undergraduate studies in Computer Engineering at the University of Nebraska at Omaha, in 2003. He later earned a M.Sc. in Electrical Engineering from The University of South Florida (USF) in 2010. That same year, he retired from the USAF after 21 years of service and was accepted into the doctoral program at USF where he later joined the advanced materials bio & integration research laboratory (AMBIR).

As a research assistant under the direction of Dr. Sylvia Thomas, he has participated in numerous educational and research endeavors that span integrated circuit processing, nanofiber synthesis by electrospinning, and material analysis and characterization by scanning electron microscopy (SEM) and Atomic Force Microscopy (AFM). Some of his interests include nanomaterials and nanotechnology, nano electromechanical systems (NEMS), micro electromechanical systems (MEMS), internet of things (IoT) applications, sensor technology and design, energy harvesting and sustainable systems. His educational philosophy focuses on capturing the students' interest and attention through applications and realistic simulations that bring any subject to life, allowing students to immerse themselves in the subject and to take control of the learning process, using the teacher as a resource and not a sage. His final work at the AMBIR lab includes the integration of miniaturized turbines as energy harvesting systems for intracorporeal and extracorporeal applications, which is the topic of his most recent work.